学 位 論 文

Microspectroscopic investigations and correlations of photoluminescence in microcrystals, nanocrystals and assemblies of lead halide perovskites

(ハロゲン化鉛ペロブスカイトのマイクロ結晶、ナノ結晶および集合体の発光挙動に関する顕微分光学的相関研究)

Graduate School of Environmental Science

Hokkaido University

Ghimire Sushant

March 2020

Dedicated to my father late *Narayan Ghimire*

Acknowledgement

First, I would like to express my sincere gratitude to my supervisor, Prof. Vasudevanpillai Biju, for his immense support, motivation, and supervision during my Ph.D. research. This dissertation work would not have been what it is now without his constructive suggestions and discussions which he had made during the planning of my work, analyzing the data, and preparing the manuscript. I would also like to thank Assoc. Prof. Yuta Takano and Assist. Prof. Ken-ichi Yuyama for their kind support and help during my research. I am very much thankful to Ms. Atsuko Fujii and all other members of Biju's group for their friendly and cooperative gesture during my stay in the lab.

Furthermore, I am indebted to Prof. Akihiro Furube and Assist. Prof. Tetsuro Kitayama, Tokushima University for their help with transient absorption measurements. I am also very much thankful to the Hokkaido University Nanotechnology PLATFORM for helping me with the TEM imaging. I thank a Japanese Government (Monbukagakusho: MEXT) Scholarship for my Ph.D research in Japan. Thanks to the Environmental Science Alumni Association, Graduate School of Environmental Science, Hokkaido University for providing me with a travel grant through the Excellent Graduate Student Overseas Visits Program 2018 to participate in the 10th Asian Photochemistry Conference, Taipei, Taiwan.

I am also grateful to Prof. Suresh K. Ghimire, Prof. Rameshwar Adhikari, and Assist. Prof. Subesh Ghimire for their continuous support and encouragement during my research stay in Japan. Last but not the least, I owe my profound gratitude to my wife Preeti, my mother Sabitra, all my family members including Subash, Suman, Sudhanshu, Subodh, Suprabha, Susmita, Lalita, Susmita, Sabitri, Tulsi, Suparth, Sukshita, Supradipta, Siddharth, Subigya, Sukrit, Rudra; and my friends especially Lata, Shahjahan, Elizabeth, Kumod, Roshan, Pramod, Prakash, and Binod for their warm support and faith in me.

Abstract

Lead halide perovskites are greatly attracted to energy-harvesting and light-emitting applications, which is owing to their long-range carrier diffusion, large absorption coefficient, high defect tolerance, wide and tunable photoluminescence color, and high photoluminescence quantum yield. In this thesis, I present the study of the charge carrier dynamics in lead halide perovskite nanocrystals, microcrystals and their close-packed assemblies. While I assign energy transfer and carrier migration to be two important factors which influence charge carrier dynamics in perovskites, I focus my research on electron harvesting and amplified emission in nanocrystals, microcrystals and films of perovskites excited with low- and high-intensity pulsed laser beams. The thesis consists of five chapters. In Chapter 1, general introduction to lead halide perovskites with special reference to their preparation, optical and charge carrier properties, and applications are reviewed. This chapter begins with brief introduction to the crystal structure and characterization of lead halide perovskites. Different wet-chemical and mechanochemical routes, such as ligand-assisted reprecipitation, hot-injection, antisolvent vapor-assisted crystallization, one-step or sequential deposition, hand grinding and ball-milling techniques for the synthesis of perovskite nanocrystals, microcrystals and thin films are discussed. Next, the optical properties of perovskites are discussed by referring to the influences of composition, temperature and pressure on the electronic band structure of perovskites. The charge carrier dynamics in perovskites are reviewed in terms of monomolecular, bimolecular and trap-assisted recombination, which is followed by an overview of the solar cell and lasing applications of these materials. Finally, the motivation and the main objectives of my research are stated. Chapter 2 is the experimental section which includes various materials and methods used in this thesis. In the study, I synthesize the close-packed pellets, microcrystals, nanocrystals, clusters and thin films of perovskites by solid state and wet-chemical methods. I introduce piezochemical method as the new solid state method for the synthesis of pure methylammonium lead or mixed bromide-iodide perovskites. I prepare nanocrystals of methylammonium, formamidinium, or cesium lead bromide perovskites by ligand-assisted reprecipitation and hot-injection methods.

Successively, these nanocrystals are self-assembled into clusters and thin films. On the other hand, the microcrystals of methylammonium lead bromide perovskites are obtained by antisolvent vapor-assisted crystallization. I characterize these perovskite samples by X-ray diffraction, UV-visible and steady-state photoluminescence spectroscopic techniques, single-particle microspectroscopy, transmission electron microscopy, and fluorescence microscopy. The charge carrier dynamics are studied by time-resolved photoluminescence and transient absorption spectroscopic techniques. In Chapter 3, I study photon recycling and energy transfer in piezochemically-synthesized closely-packed perovskite crystallites. In such closely-packed perovskite structures, a nonradiative energy transfer among different crystalline domains through the distributed energy states is obvious. I construct a distinct band gap heterojunction of a mixed bromide-iodide perovskite to confirm the nonradiative energy transfer from bromide- to iodide-rich domains and its role on photon recycling. The fast relaxation of photoexcited donor (bromide-rich domain), which is associated with the depopulation of its excited state by the acceptor (iodide-rich domain) confirms nonradiative energy transfer across the heterojunction. However, I do not rule out the carrier migration among closely-packed crystallites through the distributed band gaps in these samples. To study the carrier migration in closely-packed perovskite structures, in Chapter 4, I arrange the perovskite nanocrystals in self-assembled clusters and films. The low-intensity excitation of closely-packed perovskite nanocrystals renders delayed photoluminescence (>1 microsecond) which is attributed to the long-range diffusion of photogenerated charge carriers. On the other hand, a multitude of charge carriers are photogenerated in the closely-packed perovskite nanocrystals at high-intensity excitation. The high-density charges are spatially confined, resulting in the high rate of radiative recombination and amplified photoluminescence. Besides carrier migration, photon recycling by reabsorption-emission in such closely-packed perovskite self-assembly may complicate the carrier dynamics. Chapter 5 presents the study on the harvesting of photogenerated electrons from perovskite nanocrystal films and amplified spontaneous emission from perovskite microcrystals. To confirm the diffusion of photogenerated charge carriers in the self-assembled structures of perovskite nanocrystals, I efficiently extract photogenerated electrons from photoactivated perovskite nanocrystal films by doping with Buckminster fullerene. The electron

transfer from perovskite nanocrystals to fullerene is obvious from the enormous decrease of photoluminescence intensity and increase in the rate of carrier relaxation in fullerene-doped nanocrystal film when compared to the pristine film. These results also demonstrate the harvesting of charge carriers from a photoexcited perovskite self-assembly, which will have important implications to the development of high-efficiency solar cells. While the delayed recombination of charge carriers is promising for their efficient harvesting in solar cells, the generation and radiative recombination of multiple charges at high-intensity excitation suggest the potential application of perovskite nanocrystal assemblies in amplified spontaneous emission and lasing. However, in this study, the ensemble averaging of photoluminescence from the self-assembled perovskite nanocrystals does not allow for the observation of any spectral narrowing. Therefore, in Chapter 5, I also discuss the importance of well-defined optical cavity for amplified spontaneous emission and lasing by demonstrating amplified spontaneous emission from the isolated microcrystals of methylammonium lead bromide perovskites. I estimate the threshold of amplified spontaneous emission at 68 μJcm^{-2}. In short, the thesis develops close-packed lead halide perovskite structures that allow for the nonradiative energy transfer, and multiplication and long-range migration of charge carriers. While nonradiative energy transfer among closely-packed heterojunctions play an important role on photon recycling, the long-range carrier diffusion at the low-intensity and the multiplication of charge carriers at high-intensity excitation are important for carrier harvesting in solar cells and amplified emission in lasers.

List of Abbreviations

ASE	Amplified spontaneous emission
AVC	Antisolvent vapor crystallization
BCP	Bathocuproine
C_{60}	Buckminster fullerene
ca.	Circa
CBM	Conduction band minimum
D	Dimensional
DCM	Dichloromethane
DMF	*N*,*N*-dimethylformamide
DMSO	Dimethyl sulfoxide
EDX	Energy dispersive X-ray
E_g	Band-gap energy
EMCCD	Electron multiplying charge-coupled device
ETL	Electron transport layer
FA	Formamidinium
FTO	Fluorine-doped tin oxide
FWHM	Full width at half maximum
GPa	Gigapascal
h	Hour
HTL	Hole transport layer
ITC	Inverse temperature crystallization
ITO	Indium-doped tin oxide
k_{et}	Rate of energy transfer
k_{ET}	Rate of electron transfer
k_{nr}	Rate of non-radiative relaxation
k_r	Rate of radiative relaxation
LARP	Ligand-assisted reprecipitation
LED	Light emitting diode
LUMO	Lowest unoccupied molecular orbital
MA	Methylammonium

min	Minute
NA	Numerical aperture
NIR	Near infrared
OPA	Optical parametric amplifier
PCBM	[6,6]-phenyl-C_{61}-butyric acid methyl ester
PCE	Power conversion efficiency
PEDOT:PSS	Poly(3,4 ethylenedioxythiophene)-polystyrene sulfonate
PeLED	Perovskite-based light emitting diode
PIP	Polyimide precursor
PL	Photoluminescence
PLQY	Photoluminescence quantum yield
PMMA	Poly(methyl methacrylate)
PNC	Perovskite nanocrystal
PTAA	Poly(triaryl amine)
PVK: PBD	Poly(9-vinylcarbazole): 2-(4-biphenylyl)-5-phenyl-1,3,4-oxadiazole
RegA	Regenerative amplifier
SEM	Scanning electron microscope
SHG	Second harmonic generator
SOC	Spin-orbital coupling
Spiro-OMTAD	2,2$^{'}$,7,7-tetrakis(*N,N-dimethoxyphenylamine*)-9,9$^{'}$-spirobifluorene
TEM	Transmission electron microscope
UV	Ultraviolet
v/v	Volume-by-volume
VBM	Valence band maximum
Vis	Visible
WGM	Whispering-gallery mode
X	Cl or Br or I
XPS	X-ray photoelectron spectroscopy
XRD	X-ray diffraction
τ or τ_{av}	Photoluminescence lifetime or average photoluminescence lifetime

Contents

Chapter 1

Introduction

Abstract

The intriguing optoelectronic properties and potential applications of lead halide perovskites in the field of photovoltaic and lighting emitting devices have attracted an immense interest of the entire semiconductor community to explore this material further. In this chapter, I introduce the general concept of lead halide perovskites concerning their structure, synthesis, characterization, optical properties, electronic structure, and charge carrier properties. I also discuss the motivation and objective of my thesis work. The first section of the chapter is general introduction, where I present an overview on the structure of lead halide perovskites, their optoelectronic properties, and applications. In the second section of the chapter, I discuss the synthesis and characterization of lead halide perovskites. A more detail discussion is presented on the ligand-assisted reprecipitation, hot-injection, and antisolvent vapor-assisted crystallization methods for the synthesis of perovskite nanocrystals and microcrystals. Similarly, I also introduce different techniques for the structural and optical characterization of lead halide perovskites. In the third section, I review about the optical properties of lead halide perovskites in relation to their electronic structure. In this regard, the modification of electronic structure of perovskites, mainly by the variation of chemical composition (halogen and A-site cation) is analyzed. The fourth section is about the carrier dynamics in lead halide perovskites, where I discuss the exciton and free carrier properties in these materials. In the fifth section, I survey about the applications of lead halide perovskites as light-harvesting and light-emitting materials. Finally, I conclude the chapter by stating my motivation for this research work and the specific objective to attain the expected research goals.

1.1 General Introduction

Within a short span of time, lead halide perovskites have emerged into a class of cost-effective light-harvesting and light-emitting materials, which is in virtue of their excellent optical and electronic properties. High carrier mobility, long carrier diffusion length, large absorption coefficient, and narrow-tunable photoluminescence (PL) with nearly 100% photoluminescence quantum yield (PLQY) make these materials highly promising for solar cells, light-emitting diodes (LEDs), lasers, and photodetectors.[1-8] Synthesis of large single crystals, thin films, and nanocrystals of lead halide perovskites using inexpensive precursors are convenient which make them viable for their wide applications.

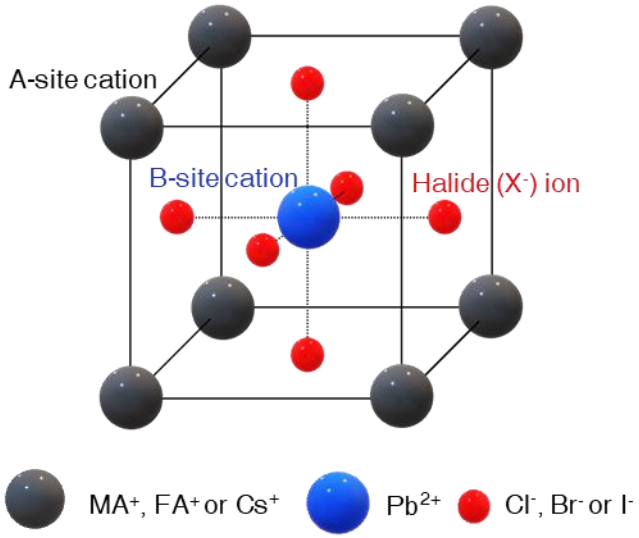

Figure 1.1 The structure of lead halide perovskites.

Lead halide perovskites have the general formula $APbX_3$, where the A-site cation such as Cs^+, methylammonium ($CH_3NH_3^+$, MA^+) or formamidinium ($CH(NH_2)_2^+$, FA^+) occupies the octahedral cavities formed by the corner-sharing lead halide octahedra (PbX_6, X=Cl, Br, I). The structure of lead halide perovskites is shown in Figure 1.1. The formation and stability of $APbX_3$ perovskite structure is determined by the Goldschmidt tolerance factor,

$$t=(r_a+r_x)/[\sqrt{2}\,(r_b+r_x)] \quad (1.1),$$

and the octahedral factor,

$\mu = r_b/r_x$ (1.2),

where r_a, r_b and r_x respectively, are the radii of A-site cation, Pb^{2+} cation and halogen. The tolerance factor in the range of 0.80 to 1.00 and the octahedral factor in 0.44 to 0.9 range render a stable perovskite structure.[9] Size of the cations and anions determine the tolerance and octahedral factors that are favorable for the formation of stable perovskite structures. Based on these stability factors, MA-, FA-, and Cs-based different isomorphs of lead halide perovskites are obtained by replacing Pb^{2+} with Sn^{2+}, Ge^{2+}, Bi^{3+}, In^{3+}, or Sb^{3+} cations and by varying halogen as X=Cl, Br, and I.[9,10]

Lead halide perovskites show wide-range of PL, which spans in the entire ultraviolet-visible-near infrared (UV-Vis-NIR) range. This wide emission color gamut in lead halide perovskites is achieved by varying the halogen composition in single and mixed halide perovskites irrespective of their size and shape.[3,5,6,11-14] Variation in halogen composition tunes the optical band-gap of these materials by modulating the valence band minimum (VBM). Such variation in PL and excellent PLQY make lead halide perovskites highly promising for the applications in multi-color display devices, LEDs, lasers, and photodetectors. In this regard, the synthesis of high-quality lead halide perovskites using different methods, characterization and study of their photophysical properties become important.

1.2 Synthesis and Characterization of Lead Halide Perovskites

Lead halide perovskites are easy to synthesize using inexpensive precursors. Different lead halide salts ($PbCl_2$, $PbBr_2$ or PbI_2) and metal halides (CsCl, CsBr or CsI), metal salts (Cs acetate or Cs-oleate), or organic ammonium halides (MAX, FAX) are used as precursors for the synthesis of perovskites. Even simple mixing of these precursors in their solution in a stoichiometric ratio followed by coating on a substrate and drying forms perovskites. Different synthesis techniques are employed for the synthesis of high-quality lead halide perovskites with their size in nano, micro or millimeter scale, which are summarized in Figure 1.2.

The techniques for the synthesis of lead halide perovskites are broadly categorized into wet-chemical and mechanochemical methods. In wet-chemical methods, a solvent plays an essential role in the growth and stabilization of the perovskite structure. As shown in Figure 1.2, different wet-chemical methods used for the synthesis of

perovskite nanocrystals (PNCs) are ligand-assisted reprecipitation (LARP)[3] and hot-injection methods.[15] Similarly, for microcrystals, antisolvent vapor-assisted crystallization (AVC)[16,17] and inverse temperature crystallization (ITC)[18,19] methods are used, whereas single-step and sequential coating methods are applied for the preparation of perovskite films.[20,21] Typically, lead halide perovskite crystals and films

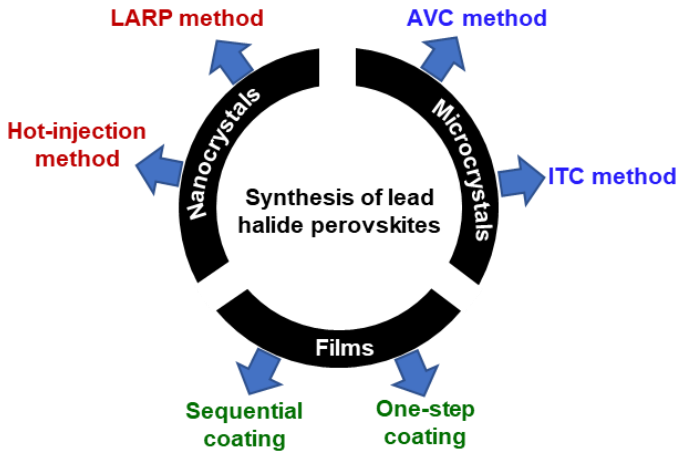

Figure 1.2 A scheme of different methods for the synthesis of lead halide perovskites.

are prepared from the stoichiometric mixture of their precursor salts dissolved in the solvents such as *N*,*N*-Dimethylformamide (DMF), dimethyl sulfoxide (DMSO) or γ-butyrolactone. On the other hand, mechanochemical synthesis involves the hand-grinding[22] or ball milling[23] of perovskite precursor mixtures. Different methods for the synthesis of nanocrystals, microcrystals and films of lead halide perovskites are discussed below in detail.

1.2.1 Synthesis of Nanocrystals

PNCs show high PLQY when compared to their bulk film counterparts.[3,15] Further, their optical properties can be tuned by controlling their size and shape.[3,4,6,12,15] Hence, different wet-chemical approaches are widely studied for the synthesis of high-quality PNCs. Wet-chemical synthesis of colloidal PNCs was first reported by Pérez-Prieto and coworkers,[24] where they used solvent-induced reprecipitation technique to obtain luminescent $MAPbBr_3$ nanoparticles. In this synthesis, *n*-octylammonium bromide and *n*-octadecylammonium bromide were used as capping ligands and acetone was used as precipitating solvent. Following the first synthesis of colloidal PNCs by Pérez-Prieto and coworkers, LARP and hot-injection methods were introduced to synthesize

luminescent PNCs with different dimensions, narrow size distribution and high PLQY.[3-8,12-15,25-27] Synthesis of zero-dimensional (0D) perovskite quantum dots, one-dimensional (1D) nanorods (or nanowires), two-dimensional (2D) nanoplatelets (or nanosheets), and three-dimensional (3D) nanocubes by the LARP and hot-injection methods are illustrated in Figure 1.3. In these methods, a combination of long chain

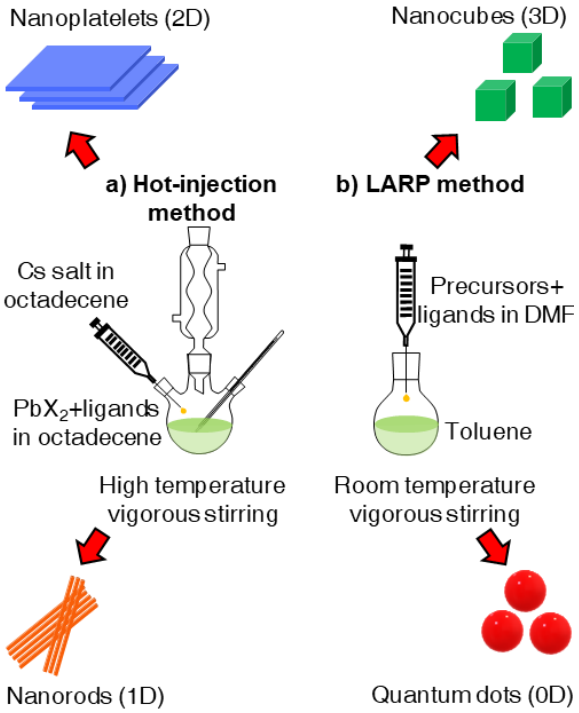

Figure 1.3 Scheme for the synthesis of 0D, 1D, 2D, and 3D PNCs by (a) hot-injection and (b) LARP methods.

organic amines (for example, oleylamine, *n*-octylamine) and organic acids (for example, oleic acid) are used as ligands to control the size and shape of the nanocrystals. The LARP method was first developed by Zhang *et al.*[3] to synthesize colloidal $MAPbX_3$ PNCs with a high PLQY at room temperature. They used *n*-octylamine and oleic acid as organic ligands to control the size of the nanocrystals. In LARP method, addition of perovskite solution prepared by dissolving the precursors in a good solvent such as DMF into a vigorously stirring poor solvent such as toluene, supplemented with long chain organic ligands, results in the precipitation of PNCs. The LARP method is also used to synthesize the highly luminescent and uniform size $FAPbX_3$ PNCs.[25]

Hot-injection method is employed for the synthesis of all-inorganic PNCs such as $CsPbX_3$.[5,6,12,13,15,26,27] In this method, a hot solution of metal salt (Cs-oleate or Cs-

acetate) dissolved in an organic solvent such as octadecene is injected into a hot solution of PbX_2 in octadecene, which is supplemented with organic amine and organic acid ligands. The crystallization of PNCs is arrested by quenching the reaction in an ice bath immediately after the hot injection of precursor solution. Kovalenko and coworkers[15] first demonstrated the synthesis of $CsPbX_3$ PNCs by hot-injection method, where monodisperse nanocubes with edge lengths of 4-15 nm were synthesized. In these methods of PNC synthesis (LARP or hot-injection), the size, shape, and dimensionality of the nanocrystals are controlled by varying the chain-lengths of organic acid and organic amines, reaction temperature, and reaction time. Further, PNCs with different single and mixed halide compositions are also easily synthesized by these methods, which is by using different PbX_2 (X=Cl, Br, I) salts, by varying the ratio of mixture of different PbX_2 ($PbCl_2$/$PbBr_2$ or $PbBr_2$/PbI_2) during synthesis, or by post-synthesis halide exchange reactions on PNCs.[3-8,12-15,25,26]

1.2.2 Synthesis of Microcrystals and Films

High quality lead halide perovskite single crystals with size ranging from micro-to millimeter scale are attaining considerable interests due to the long carrier diffusion length, long carrier lifetime, and low defect density in them, which are highly promising for solar cells.[1,16-19,28,29] These crystals are generally prepared by using AVC[16,17] and ITC[18,19] methods. As shown in Figure 1.4a, in AVC method, single crystals of perovskites are grown by exposing the precursor solution of perovskite to the vapors of another solvent in which the perovskite crystal is poorly soluble (thus called antisolvent). During the process, the vapors of antisolvent slowly diffuse into the perovskite precursor solution, and the reduced solubility of perovskites in the antisolvent facilitates the nucleation and growth of the crystals. However, the quality and size of perovskite single crystals depend on the type of antisolvent, the volume ratio between solvent and antisolvent, the antisolvent vapor diffusion time, and the diffusion rate. Kirmayer and coworkers[16] were first to employ the AVC method to prepare the microcrystals of $MAPbBr_3$ and $MAPbI_3$ using DMF as solvent and isopropyl alcohol as antisolvent. Later, Shi *et al.*[17] modified the method by using dichloromethane (DCM) as antisolvent for preparing the high-quality millimeter size $MAPbBr_3$ and $MAPbI_3$ single crystals. Unlike isopropyl alcohol, DCM is a poor solvent for MAX and PbX_2 salts and therefore facilitates the growth of large single crystals upon slow diffusion

into the precursor solution. On the other hand, ITC method is assisted by the retrograde solubility of perovskite crystals under elevated temperature. Lead halide perovskites show decrease in solubility in some solvents such as DMF or γ-butyrolactone under increasing temperature, which is known as inverse temperature or retrograde solubility.

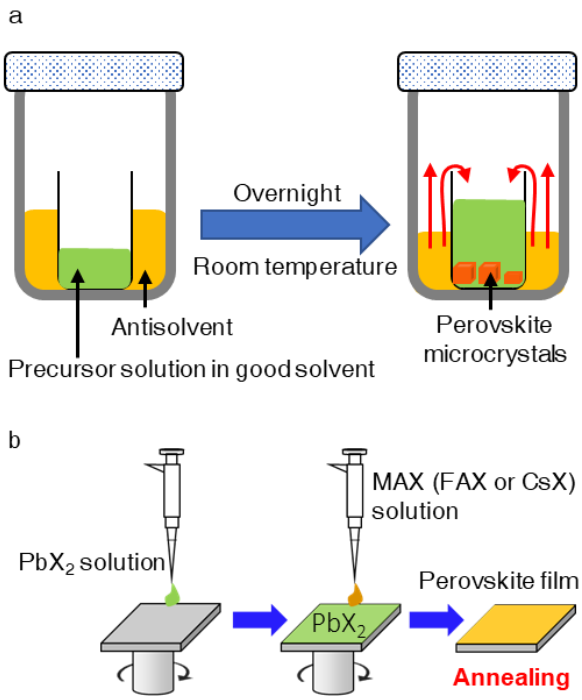

Figure 1.4 Synthesis of microcrystals and thin films of lead halide perovskites. (a) AVC method for the synthesis of perovskite microcrystals and (b) sequential deposition method for the preparation of perovskite thin films.

Saidaminov *et al.*[18,19] used ITC method to grow high-quality single crystals of $MAPbBr_3$ and $MAPbI_3$ perovskites. Unlike AVC method, the rate of crystal growth is much faster in ITC method, and this method can be used to prepare the size- and shape-controlled perovskite single crystals. Nonetheless, in both the methods, the selection of suitable solvents for the crystallization and growth of high-quality perovskite crystals is important.

Lead halide perovskite films are employed as light absorbing and light emitting layers in solar cells and LEDs, respectively. Films of lead halide perovskite are prepared by the single-step or sequential deposition of precursor solutions on a substrate by using different techniques, such as spin-coating,[2,20] hot-casting,[30] spray-coating,[31] doctor-blade coating,[32] etc. In single-step deposition, the two precursors [AX (A=MA, FA or

Cs) and PbX_2] in their stoichiometric ratio are dissolved together in a solvent (DMF, DMSO or γ-butyrolactone) and coated on the substrate, which is followed by subsequent drying and annealing.[2] This renders with perovskite films in which the uniformity and grain size of perovskite crystallites can be controlled by compositional engineering, controlling the rate of solvent evaporation, and tuning the annealing temperature.[2,21] On the other hand, in sequential deposition,[20] one of the perovskite precursors, typically PbX_2, dissolved in an appropriate solvent is coated on a substrate which is followed by the deposition of another precursor (AX) solution, drying and annealing. Figure 1.4b schematically shows the sequential deposition method for a lead halide perovskite film.

1.2.3 Mechanochemical Synthesis

Large-sized or nanocrystalline lead halide perovskites are also prepared by the mechanochemical synthesis,[22,23,33-39] where chemical reaction between the precursors is induced by the mechanical forces. Both the bottom-up[22,23,33-38] and top-down[39] approaches can be employed in the mechanochemical synthesis of lead halide perovskites. In bottom-up approach, the stoichiometric mixture of precursor salts (AX and PbX_2) in their solid state are subjected to hand-grinding, which is by using a mortar and pestle, or ball-milling in absence of solvent, resulting in the formation of polycrystalline and phase pure powders of lead halide perovskites. This solventless solid-state approach is considered as the green method of material synthesis, where the use of organic solvents is avoided during the synthesis. Stoumpos *et al.*[22] first demonstrated the mechanochemical synthesis of perovskites using a hand-grinding process which rendered with the desired $MASnI_3$ product and large amounts of unreacted precursors. Such hand-grinding process of mechanochemical synthesis takes quite a long time for the conversion of precursors into perovskite structure. Later, Prochowicz *et al.*[23] successfully demonstrated the phase pure and high yield synthesis of $MAPbI_3$ perovskites using electric ball-milling as the efficient mechanochemical route. Apart from the synthesis of pure $APbX_3$ type perovskites, those involving mixed cation,[33] mixed halogen[34] and other types such as 0D (Cs_4PbBr_6, Cs_4PbCl_6),[35] 1D ($GuaPbI_3$),[36] and 2D ($CsPb_2Br_5$, $CsPb_2Cl_5$, Gua_2PbI_4)[35,36] perovskites are also easily synthesized by the mechanochemical method.

In the top-down approach, lead halide PNCs are obtained by applying the mechanical force to the corresponding bulk crystals in presence of solvents and ligands. For example, Kovalenko and coworkers[39] have used wet ball-milling of bulk perovskite crystals mixed with a solvent and a capping ligand, *n*-oleylammonium bromide, to obtain highly luminescent green emitting nanocrystals of Cs- or FA-based 3D lead halide perovskites. The method is also extended to mechanically induce halide exchange reaction to produce bromide-iodide mixed halide PNCs. Such facile and diverse approaches for synthesizing PNCs of different compositions, sizes, and shapes make them an easy recipe in many laboratories for further studies and applications. Nevertheless, such diversity in synthesis also employs many challenges to characterize these materials.

1.2.4 Characterization

Different spectroscopic and microscopic techniques are employed for the optical, electronic, structural and morphological characterization of lead halide perovskites (Figure 1.5). Since the crystals and films of lead halide perovskites are luminescent under UV light, UV-Vis absorption and steady-state PL spectroscopic techniques are used for the easy and first-hand optical characterization of these materials. The band-gap of lead halide perovskites absorbs light in the range of UV-Vis to NIR. Therefore, the absorption and PL spectra of lead halide perovskites involving pure halide, mixed halide and mixed cation compositions span the entire UV-Vis-NIR region with sharp bands.[3-8,11-15,24-26] For instance, as shown in Figure 1.5a, $MAPbCl_3$, $MAPbBr_3$, and $MAPbI_3$ perovskites show slightly Stokes-shifted band-edge absorption and emission maxima in the blue, green and red (or NIR) region of electromagnetic spectrum, respectively.[11] Furthermore, the absorption and PL spectroscopic techniques help to monitor the halide exchange reaction in perovskites, where the band-edge absorption and emission peaks shift from blue to cyan and cyan to green when Cl is exchanged with Br, and from green to orange and orange to red when Br is exchanged with I.[13,14] Moreover, these spectroscopic techniques are also helpful in analyzing the colloidal solution of perovskites with different nanocrystal size, shape and dimensionality.[12,25,26]

The structural characterization of lead halide perovskites is carried out by using X-ray diffraction (XRD) techniques (Figure 1.5b). Both the single crystal and powder XRD techniques are used to analyze the crystal structure of perovskites. Luminescent

lead halide perovskites crystallize into orthorhombic (low-temperature), tetragonal (room-temperature) and cubic (high-temperature) phases.[41-43] On the other hand, during the synthesis or storage, some non-perovskite phases, known as yellow phase, may form which are non-luminescent. These crystalline phases of lead halide perovskites are well

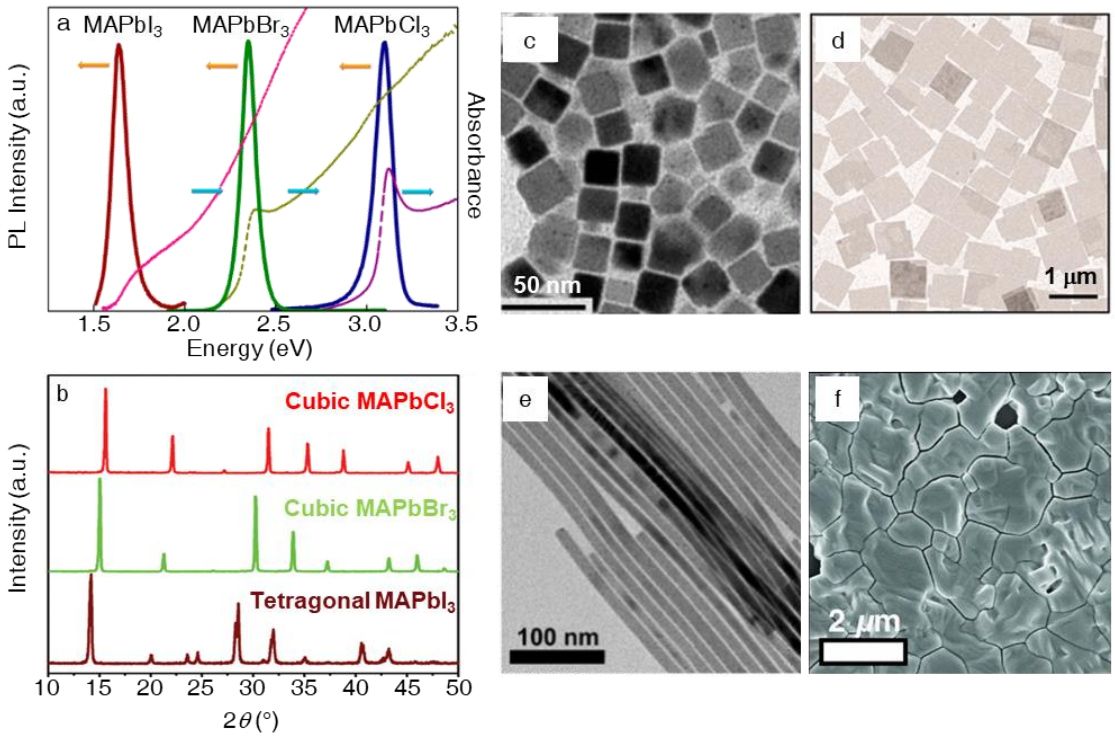

Figure 1.5 Characterization of lead halide perovskites. (a) Absorption and PL spectra of $MAPbX_3$ (X=Cl, Br, I) PNCs. (b) XRD patterns of $MAPbX_3$ perovskite single crystals. (c-e) Transmission electron microscopic images of (c) $MAPbBr_3$ perovskite nanocubes, (d) $CsPbBr_3$ nanosheets, and (e) $CsPbBr_3$ nanowires. (f) Scanning electron microscopic image of a mixed halide $MAPbI_3(Cl)$ perovskite film. Reproduced from (a,c) Shamsi *et al.*,[11] (b) Liu *et al.*,[29] (d) Shamsi *et al.*,[27] (e) Zhou *et al.*,[40] and (f) deQuilettes *et al.*[2]

characterized by XRD techniques. Besides, halogen composition and the size of A-site cation can also influence the lattice parameters and crystal structure of perovskites.[13,14,29,41,44] For example, structural deformation occurs through octahedral tilting in perovskite lattice when a large FA^+ cation is replaced by smaller MA^+, which in turn becomes more prominent when the replacement occurs by much smaller Cs^+.[41,44]

The octahedral tilt is reflected in the XRD pattern of lead halide perovskites by shifting of the Bragg's diffraction peak to a smaller 2θ angle.[41] Similarly, as shown in Figure 1.5b, while moving down the halogen group, the lattice contraction increases, and the diffraction peaks shift to the smaller 2θ.[13,14,29] Such lattice distortion in perovskites can also occur as the function of temperature,[42,45] pressure,[46,47] and moisture,[48] which sometimes becomes so large that the perovskite undergoes phase transition, or the structure becomes unstable. Therefore, it is very important to characterize the crystal structure of synthesized perovskite crystals and films, and XRD is one of the efficient techniques.

Electron microscopic techniques such as transmission electron microscopy (TEM) and scanning electron microscopy (SEM) are used for the morphological characterization of nanocrystals, microcrystals and thin films of lead halide perovskite, which are shown in Figure 1.5c-f. Such microscopic techniques are useful for studying the shape, size, and stability of perovskite crystallites. The nanocrystals of lead halide perovskites are revealed with 3D cubic (Figure 1.5c),[11] 2D platelet or sheet (Figure 1.5d),[27] and 1D rod or wire-like (Figure 1.5e)[40] structures by using electron microscopy. Similarly, as shown in Figure 1.5f, electron microscopic studies are also helpful in understanding the distribution of grain-boundaries in polycrystalline thin films of perovskites.[2] Such grain-boundaries influence the performance of lead halide perovskite films in solar cells.

Other techniques such as X-ray photoelectron spectroscopy (XPS), electron dispersive X-ray (EDX), time-resolved PL spectroscopy, and transient absorption spectroscopy are used for the advanced characterization of lead halide perovskites. The compositional characterization of perovskites is carried out by using XPS and EDX techniques, whereas the time-resolved PL and transient absorption spectroscopic techniques are helpful for analyzing the ultrafast carrier dynamics in these materials.

1.3 Optical Properties of Lead Halide Perovskites

Lead halide perovskites are direct band-gap semiconductors whose band-edge electronic structure is mainly contributed by the atomic orbitals of $[PbX_6]^{4-}$ octahedra.[9,49-51] As shown in Figure 1.6a, the conduction band minimum (CBM) has the sigma (σ^*) and pie (π^*) antibonding orbitals, which are formed by the hybridization

of the 6*p*-orbitals of Pb and the *s*- and *p*- orbitals of halogens, respectively. On the other hand, the VBM is contributed by the *6s*- and *6p*- orbitals of Pb and the *s*- and *p*-orbitals of halogen. The band-gaps and the optical properties of lead halide perovskites are therefore mainly governed by the $[PbX_6]^{4-}$ octahedra. The change in composition of halogen from Cl to Br and Br to I increases the contribution of halogen *p*-orbitals in VBM, energetically favoring the orbital mixing between the halide *p*-orbitals and Pb *s*-orbital to a greater extent. This lowers the optical band-gap energy (E_g) in lead halide

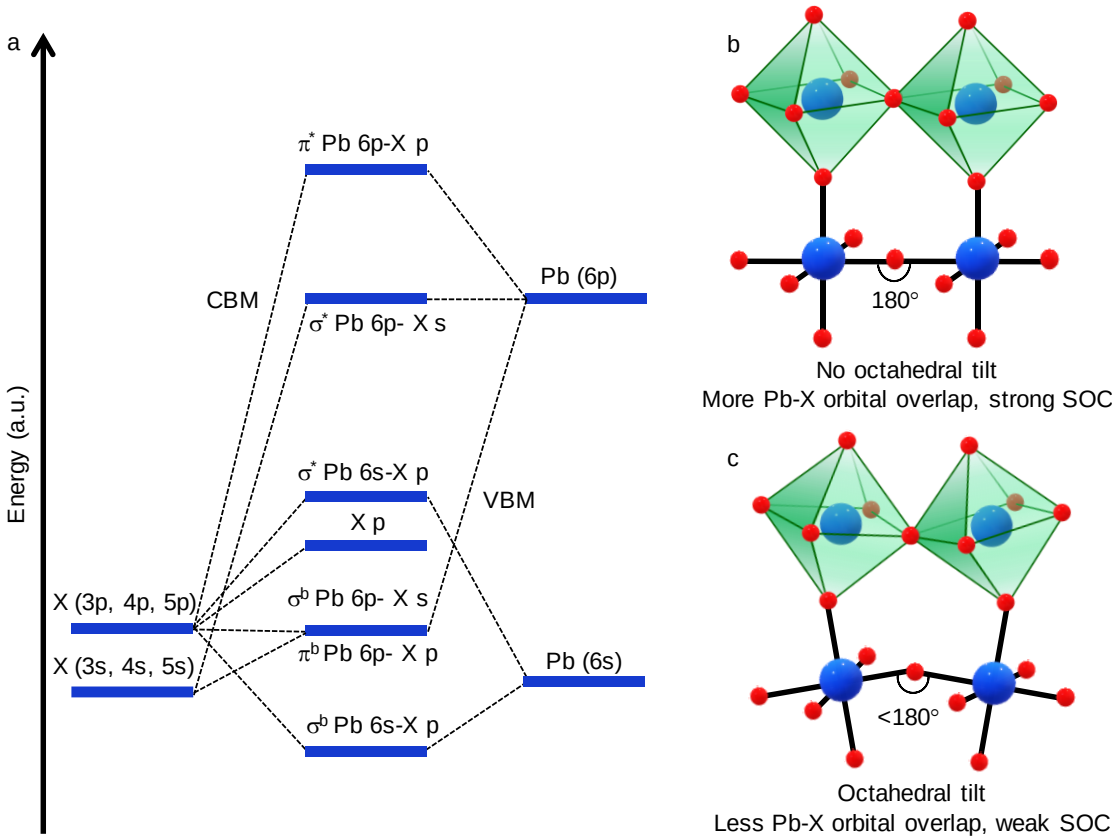

Figure 1.6 (a) Electronic structure of lead halide perovskite. (b,c) Crystal structure of lead halide perovskites (a) without and (b) with octahedral tilting.

perovskites in the order, E_g (Cl)>E_g (Br)>E_g (I).[9,14] Therefore, the PL of lead halide perovskites can be tuned in the UV-Vis-NIR region by varying the halogen composition through anion exchange, as shown in Figure 1.7a,b.[12] Spin-orbital coupling (SOC) influences the optical band-gaps in lead halide perovskites,[44,50,51] which is the consequence of mixing of orbital-angular momentum (i.e. electron motion in *p*, *d*, and *f* orbitals) and spin-angular momentum (i.e. the electron spin around its own axis in clockwise or anticlockwise direction). In lead halide perovskites, SOC splits the three-

fold degenerate CBM into the lower-energy doublet spin-orbit split-off states and higher-energy quadruplet states, causing the significant lowering of optical band-gap energies in these materials. In fact, SOC tunes the optical properties of perovskites by modulating the CBM, which is associated with the compositions of A-site and B-site cations and octahedral tilting.[41,44,52,53]

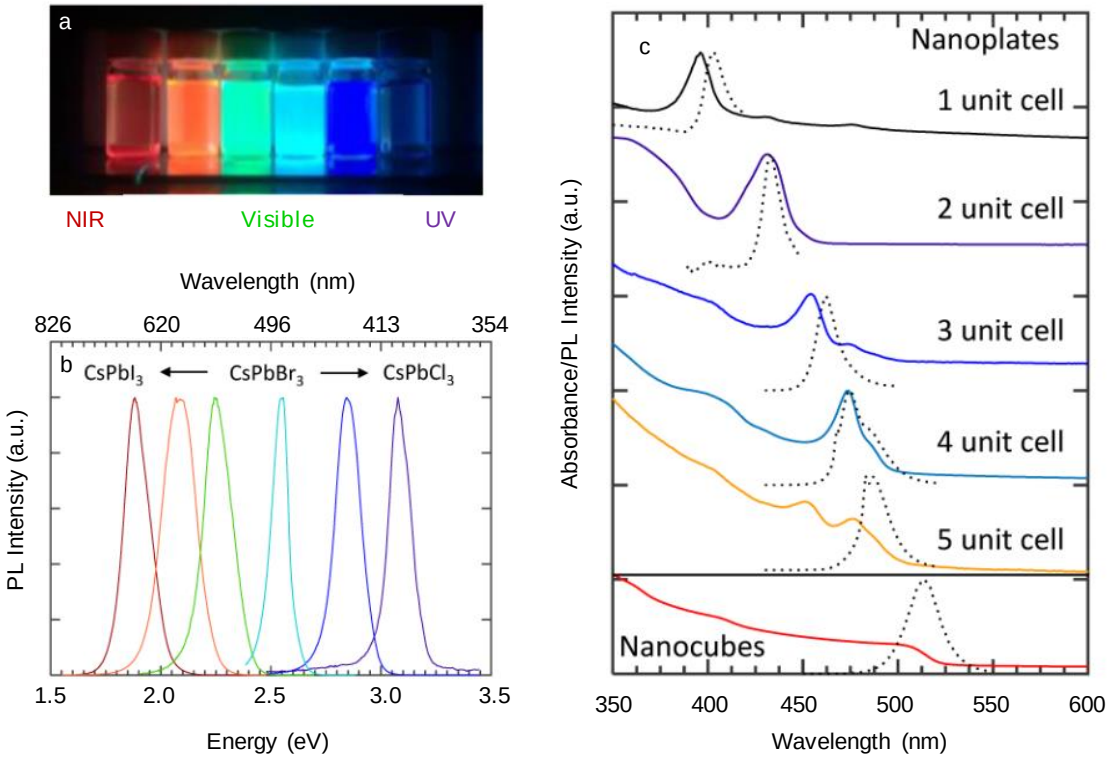

Figure 1.7 (a) Photographs of colloidal solution of halide ion exchanged $CsPbX_3$ PNCs under UV (365 nm) excitation, (b) PL spectra of halide ion exchanged $CsPbX_3$ PNCs, and (c) Absorption (solid lines) and PL (dashed lines) spectra of $CsPbBr_3$ nanoplatelets and nanocubes. Reproduced from Bekenstein *et al.*[12]

As the size of A-site cation decreases from a larger FA^+ to a smaller Cs^+, the Pb-X-Pb dihedral angle decreases from its ideal value (180°), resulting in an octahedral tilt.[9,41,44] Figure 1.6b,c shows the crystal structure of lead halide perovskites without and with octahedral tilting, respectively. Such a tilt in PbX_6 octahedra weakens SOC by lowering the orbital overlap between Pb and X and decreasing the contribution of Pb orbitals to the band-edge. These decrease in SOC increases the band-gap and shifts the absorption and PL band to blue. Interestingly, the change in crystal structure from cubic to tetragonal or other phases also leads to an octahedral tilt,[44] and more importantly, such crystal phase transition and octahedral tilt is the consequence of

temperature[42,45] and pressure[46,47] exerted on the perovskite lattice. Therefore, the band-edge electronic structure in perovskites varies with these factors, resulting in different E_g values and hence different optical properties of these materials. Apart from the chemical composition and octahedral symmetry, the optical properties of lead halide perovskites are also influenced by the quantum-size effects or quantum confinement.[12,15,25,26] When the physical size of a material is smaller than or comparable to the corresponding exciton Bohr radius, the quantum confinement comes into play, resulting in the blue-shift of absorption edge and PL band. As shown in Figure 1.7c, a blue-shift in the absorption and PL spectra is observed with the change in dimension of $CsPbBr_3$ PNCs from a 3D nanocubes to 2D nanoplatelets; and the gradual blue-shift in the absorption and PL spectra further continues with the decrease in the platelet thickness from 5 unit cells to 1 unit cell.[12]

1.4 Charge Carrier Properties of Lead Halide Perovskites

In lead halide perovskites single crystals and films, free charge carriers dominate over the bound excitons at room temperature which is the consequence of low exciton binding energy.[54-62] In fact, the exciton dissociates into free charge carriers when the thermal energy surpasses the associated binding energy in these materials. The free charge carrier property of halide perovskites is associated with long carrier diffusion length ($L_D=\sqrt{k_B T\mu\tau/e}$, where k_B is Boltzmann constant, T is absolute temperature, μ is charge carrier mobility, τ is PL lifetime, and e is electronic charge) and delayed PL. Further, the shallow defects and low defect densities in perovskite single crystals and films also help for such a long-range migration and delayed recombination of photogenerated charge carriers. Nevertheless, the carrier lifetime varies in the range of sub-nanoseconds to microseconds in different types of halide perovskites, depending upon their size, dimensionality, and composition.[1-3,5,6,9,11,15,17,18,23,25,28,30,54,57]

Different charge carrier recombination rates in lead perovskites is explained by a differential equation 1.3,[62]

$$\frac{dn}{dt} = -k_3 n^3 - k_2 n^2 - k_1 n \quad \text{.....(1.3),}$$

where k_1, k_2, and k_3 are the monomolecular, bimolecular and Auger recombination rate constants, and n is the concentration of total charge carriers. Hence, the carrier lifetimes,

mobility and diffusion lengths in perovskites are influenced by the monomolecular, bimolecular and Auger recombination mechanisms. An excitonic (geminate) or a trap-assisted carrier recombination is involved in the monomolecular mechanism.[56,59,62] However, the contribution of excitonic recombination is less significant in the process, which is due to the small exciton binding energies in single crystals and thin films of lead halide perovskites.[54-62] Therefore, the trap-assisted processes mainly attribute to the monomolecular carrier recombination rate (in the order of ~10^6 s^{-1})[56] in perovskites. Material purity and crystal phase alter the density, activation energy and depth of the traps in perovskites, affecting the trap-assisted monomolecular recombination process. For example, when compared to the orthorhombic crystal phase, the cubic and tetragonal phases of lead halide perovskites have higher rate of trap-assisted monomolecular carrier recombination, which is due to the different trap formation activation energies in these different crystalline phases.[56,62]

Bimolecular recombination, on the other hand, involves the recombination of free charge carriers (non-geminate), and it is influenced by the halide and B-site cation compositions in perovskites. The bimolecular recombination rate in lead halide perovskites deviates from the Langevin theory, resulting in lower k_2/μ value than the predicted one. Hence, the non-Langevin bimolecular recombination in lead halide perovskites indicates high carrier mobility,[54,56,59,62] which is attributed to the occupation of different molecular orbitals formed by the overlap of energetically different *s*- and *p*-orbitals from halogen and Pb ions in a perovskite unit cell by an electron and a hole.

Trap-assisted and bimolecular recombination processes in perovskites dominate at low-intensity of excitation and intermediate charge carrier concentration, whereas Auger-assisted process is involved at higher intensity of excitation and high charge carrier concentration.[54,56,59,62] Also, the Auger-assisted recombination process is temperature and crystal phase-dependent, which decreases at low temperature and orthorhombic phase, increases at room temperature and tetragonal phase, and decreases again at high temperature and cubic phase.[42] This temperature or crystal phase-dependent variation of Auger recombination rate in perovskites is due to the different extent of SOC and hydrogen bonding in different crystalline structures, which is related to the change in band-edge electronic structure.

On contrary to the above discussed mechanism of trap-assisted and free-carrier recombination in lead halide perovskites, the isolated nanocrystals and quantum dots of these materials show weak to strong quantum confinement regime, depending upon their size, thickness or dimensionality, in which the carrier recombination is mainly governed by the geminate type bound excitonic recombination.[12,15,25,26,58] For instance, the exciton binding energy for micrometer-size bulk $MAPbBr_3$ perovskite crystal is 84 meV, which increases by more than three times to 320 meV in the case of corresponding nanoparticles with size ca. 8 nm.[58] Further, slow cooling and efficient extraction of hot carriers are reported for the PNC colloidal solutions despite the quantum confinement effects in them.[63] Although the strong quantum confinement regime in lead halide perovskites belongs to 2-7 nm range,[15,25,58,64-66] a great many studies reporting the excellent opto-electronic properties and applications of PNCs have used the nanocrystals with size which is in the weak or negligible quantum confinement regime. This suggests that PNCs show immense diversity in terms of properties and applications.

1.5 Applications of Lead Halide Perovskites

The promising applications of lead halide perovskites are found in solar cells, LEDs, and lasers, which are discussed briefly in this section.

1.5.1 Solar Cells

Recently, lead halide perovskites are emerging as the highly desirable light-absorbing materials for solar cells.[1,2,16-18,20,21,23,28,30,31-33,48,] The high absorption coefficient, high and ambipolar carrier mobility, long diffusion length of charge carriers, defect tolerant properties, and cost-effective preparation methods make lead halide perovskites compatible for harvesting solar energy. After the first demonstration of lead halide perovskite solar cell by Miyasaka and coworkers[67], many researchers were attracted to design cost-effective solar cells with improved power conversion efficiency (PCE) by using lead halide perovskites as active light-absorbing material. Indeed, to this date, the PCE of perovskite solar cells has improved up to 25.2%,[68] which has encouraged their commercialization.

In general, uniform lead halide perovskite films with low or no grain boundaries, high surface coverage, and high stability are desirable for high efficiency perovskite solar cells.[2,20,30-32] Such films are fabricated by a single-step or sequential deposition

methods which are discussed in the previous section. Figure 1.8a shows a typical perovskite solar cell architecture which consists of a perovskite layer as the light absorbing material in between the electron transport layer (ETL) and hole transport layer (HTL), and the whole architecture is sandwiched between a conducting glass substrate [fluorine-doped tin oxide (FTO) or indium-doped tin oxide (ITO)] and Au or Ag electrode. Figure 1.8b shows the energy levels of various ETLs, HTLs, lead halide

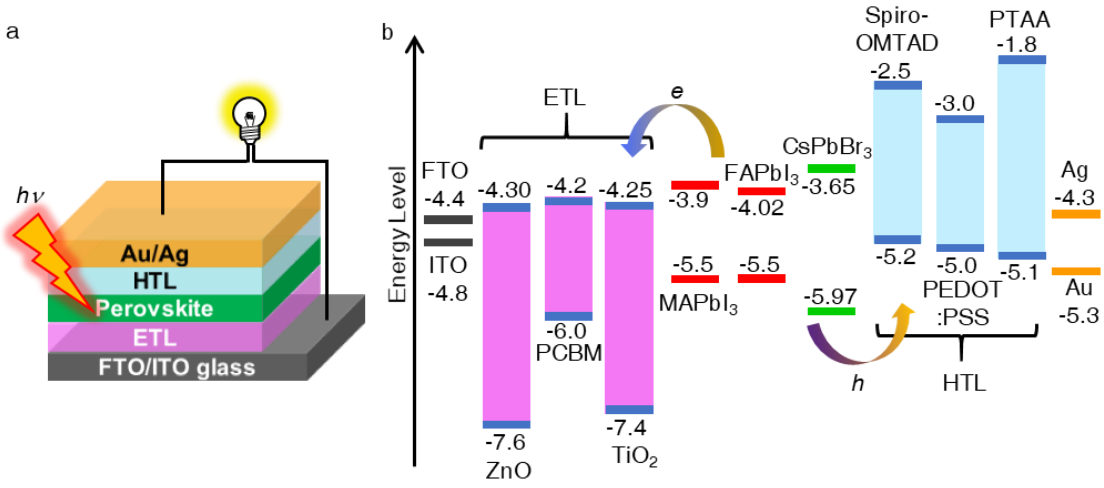

Figure 1.8 Solar cell application of perovskites. (a) Device architecture of a perovskite solar cell. (b) Energy levels of various ETLs, HTLs, perovskites, and electrode materials.

perovskites, and electrode materials that are energetically favorable to construct a perovskite solar cell, in which the efficient extraction and transport of photogenerated electrons and holes from a perovskite layer are facilitated by the chosen ETLs, HTLs and electrode materials. The common *n*-type ETLs used in perovskite solar cells are [6,6]-phenyl-C_{61}-butyric acid methyl ester (PCBM), TiO_2, ZnO, or Buckminster fullerene (C_{60}); and the common *p*-type HTLs are poly(3,4 ethylenedioxythiophene)-polystyrene sulfonate (PEDOT:PSS), 2,2',7,7-tetrakis(*N,N-dimethoxyphenylamine*)-9,9'-spirobifluorene (spiro-OMTAD), or poly(triaryl amine) [PTAA].

Apart from the energetically favorable combination of perovskites, ETLs, HTLs and electrodes, different approaches are used to improve the efficiency of lead halide perovskite solar cells. For example, compositional engineering of lead halide perovskite films by using mixed halogen and mixed A-site cation has improved the mobility and diffusion of charge carriers and reduced the defect density in the film.[69,70] Further, such

defect density can also be reduced by minimizing the pin-holes and grain boundaries in the film through the control of nucleation and growth of perovskite crystallites.[2] The quality of lead halide perovskite films is improved by the chemical treatment of films with ligands, Lewis-acid, Lewis-base or other additives which renders high PCE in solar cells.[71-73] Chemical engineering of ETL, HTL and the perovskite-HTL (ETL) interface are also employed to improve the PCE of perovskite solar cells.[74-77]

One of the limitations of lead halide perovskites for their application in solar cells is their stability against moisture and high-intensity light. The highly ionic nature of perovskite lattice results in degradation and the leakage of Pb^{2+} cation in presence of moisture.[48,74] Further, the photoionic conductivity of halides and vacancies also limits the performance of perovskite solar cells.[78,79] Nevertheless, different approaches such as hydrophobic coating of perovskite layer, modifying the composition with mixed cations and mixed halides, and treating the lead halide perovskites with additives are employed to address the stability of perovskites and improve the performance of perovskite solar cells to their optimal level.[2,69-77] For example, Bai *et al.*[74] have used water-resistant cross-linkable silane-functionalized doped C_{60} as ETL and demonstrated a moisture-stable and high efficiency (19.5%) perovskite solar cell. The hydrophobic tails of trifluoromethyl groups bonded to the cross-linked silane on the doped C_{60} surface prevented any water molecule or moisture to permeate into the perovskite film which is underneath the fullerene layer. Their perovskite solar cell could retain the original high efficiency even after exposing it to the ambient environment for 30 days.

1.5.2 Light Emitting Diodes

Perovskites are exceptional materials for next-generation LEDs, which is attributed to their narrow emission band and high color purity, PL tunability in UV-Vis-NIR region, high PLQY, low defect density, and low-cost solution processability.[3,4,12,13,14,15,25,26,27] Further, lead halide perovskites show long-range ambipolar charge transport,[1,2] facilitating the efficient injection and transport of charges at the interface and low turn-on voltage, which are essential for the LED applications. In perovskite-based LEDs (PeLEDs), the emitter layer comprises of a 3D, layered, or nanostructured perovskites which is sandwiched between ETLs (or electron-injection layer), HTLs (or hole-injection layer) and electrical contacts. A typical device architecture of $MAPbBr_3$

PeLED is shown in Figure 1.9a and the corresponding electroluminescence spectra at different applied voltage along with the photograph of a working PeLED device is shown in Figure 1.9b.[4] Here, $MAPbBr_3$ nanoplatelet film is sandwiched between a HTL (PEDOT: PSS) and an ETL (bathocuproine, BCP). Different types of ETLs and HTLs are discussed in the perovskite solar cell section and Figure 1.8b of this chapter.

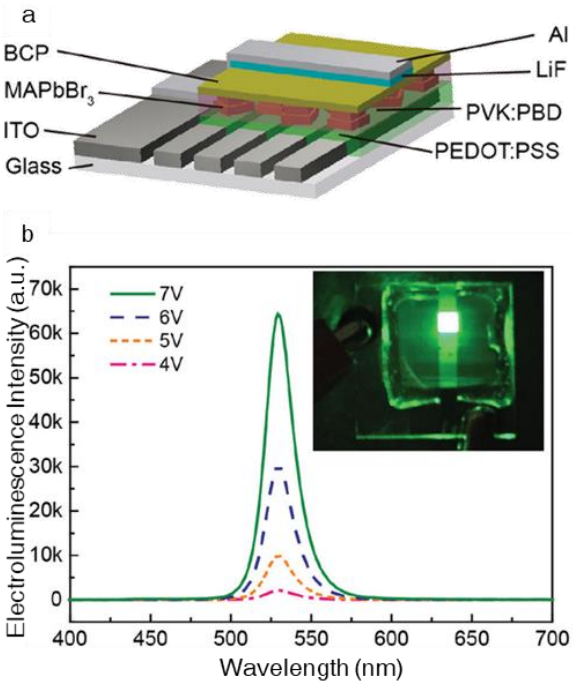

Figure 1.9 LED application of lead halide perovskites. (a) Device architecture of a PeLED. (b) Electroluminescence spectra of $MAPbBr_3$ PeLED under different applied voltage. Inset is a photograph of a working $MAPbBr_3$ PeLED at 7 V. Reproduced from Ling *et al.*[4]

The efficiency of PeLED is limited by the optical loss or current leakage induced by the presence of pin-holes due to the incomplete surface coverage and excess metallic lead present due to the incomplete formation of perovskites.[4,80,81] Therefore, for the optimal external quantum efficiency, high surface coverage with smooth and grain boundary free morphology of perovskite light-emitting layer is essential. This is obtained by using different types of polymers such as poly(methyl methacrylate) [PMMA] or polyimide precursor (PIP), poly(9-vinylcarbazole): 2-(4-biphenylyl)-5-phenyl-1,3,4-oxadiazole (PVK: PBD) blends as host materials for the perovskite emitters.[4,81] Furthermore, the problem due to the presence of excess metallic Pb can be lifted by using excess of AX salt during the film deposition which suppresses the

formation of free Pb.[80] Apart from the quality of light-emitting material, the design of PeLED should also account for the electrical losses for which the selection of interfaces is critical. As shown in Figure 1.8b, the selection of ETL and HTL is mainly determined by their band alignment with the perovskite layer and solution processability.

1.5.3 Lasers

Beside solar cells and PeLEDs, lead halide perovskites are promising materials for low-threshold lasing and ASE.[5,6,82-88] After the successful demonstration of low-threshold ASE in solution-processed $CsPbX_3$ (X = Cl, Br, and I) PNCs by Yakunin *et*

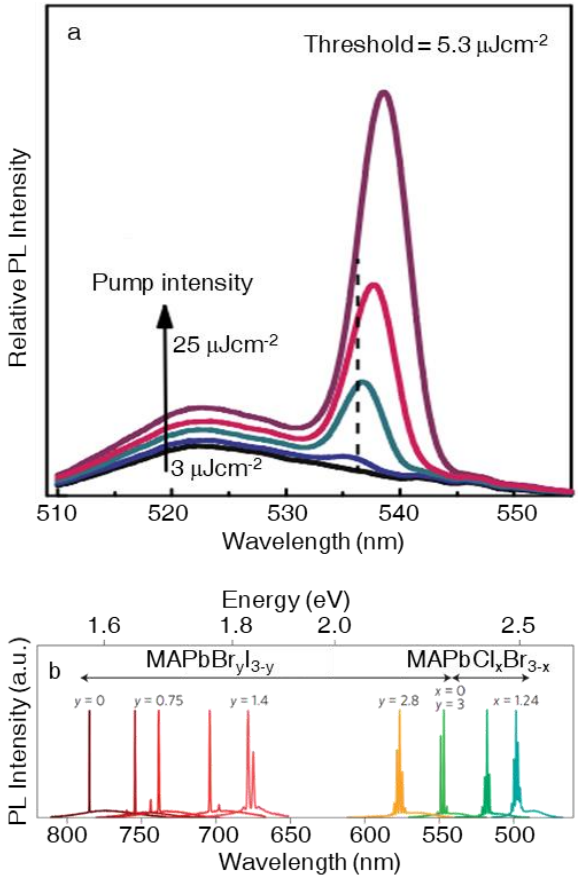

Figure 1.10 ASE and lasing in lead halide perovskites. (a) ASE in $CsPbBr_3$ PNC film. (b) Single and multimode lasing with tunable emission color in perovskites. Reproduced from (a) Yakunin *et al.*[5] and (b) Zhu *et al.*[6]

al.,[5] investigations of lasing and ASE have been extended to various MA-, FA- and Cs-based perovskites. As shown in Figure 1.10a, the ASE in lead halide perovskites is marked by the narrowing and red-shifting of PL band above a certain excitation

threshold when the sample is excited under increasing pump fluence or intensity.[5] Similarly, as shown in Figure 1.10b, single and multimode low-threshold lasing is observed in lead halide perovskites, in which the lasing wavelength is tuned in the entire UV-Vis-NIR region by modulating the halogen composition.[5,6,83]

Arrangement of all-inorganic (Cs-based), organic-inorganic (MA- or FA-based), and mixed halide perovskites in random cavity,[82,83] Fabry-Pérot cavity,[6,84] Whispering Gallery Mode (WGM) cavity [5,85,86] and vertical microcavity[87,88] results in low-threshold lasing or ASE in these materials. The micro/nanodomains present in perovskite films result in the coherent backscattering of propagating PL, which forms close-loop random cavity.[82,83] A vertical cavity is prepared by sandwiching a perovskite film in between two reflector mirrors.[87,88] Similarly, lead halide perovskites with different shapes, such as microspheres and 2D micro or nanoplates act as WGM cavity.[5,85,86] Such cavities are also formed by coating of perovskite nanocrystals on the silica microspheres.[5] Besides, lead halide perovskite cuboids, rods and wires act as optical waveguides along the axial or planar direction and create a Fabry–Pérot cavity.[6,84] The lasing threshold in these cavities vary largely, depending upon the factors, such as dimensions, end facets, crystal quality and halide composition.

1.6 Motivation and Objectives of Research

Interesting optical and charge carrier properties make lead halide perovskites highly cherished among material scientists, chemists and physicists for the further exploration and application-based studies. While generation and diffusion of charges in perovskite single crystals and bulk films are largely exploited in constructing high-performance solar cells and PeLEDs, the control and stabilization of such charge carrier dynamics in these materials for application-specific purposes are still fascinating and motivated me to study further in this direction. Therefore, the main objective of this thesis is the design and development of closely-packed lead halide perovskite structures or assemblies that allow long-range diffusion of charge carriers and delayed emission. The thesis aims to study the mechanism of diffusion of charge carriers in these structures as the function of band-gap distributions and the excitation laser intensity modulations. Further, the thesis also demonstrates the applications of such charge carrier properties of lead halide perovskites in electron-harvesting and ASE. This study will be very helpful to understand, on the one hand, the fundamentals of carrier dynamics in lead

halide perovskites when the individual (nano or micro) crystallites are closely arranged in an assembly and, on the other hand, the applications of these materials in solar cells and lasers.

References

1. Dong, Q.; Fang, Y.; Shao, Y.; Mulligan, P.; Qiu, J.; Cao, L.; Huang, J. Electron-Hole Diffusion Lengths >175 μm in Solution-Grown $CH_3NH_3PbI_3$ Single Crystals. *Science* **2015**, *347*, 967–970.
2. deQuilettes, D. W.; Vorpahl, S. M.; Stranks, S. D.; Nagaoka, H.; Eperon, G. E.; Ziffer, M. E.; Snaith, H. J.; Ginger, D. S. Impact of Microstructure on Local Carrier Lifetime in Perovskite Solar Cells. *Science* **2015**, *348*, 683–686.
3. Zhang, F.; Zhong, H.; Chen, C.; Wu, X.; Hu, X.; Huang, H.; Han, J.; Zou, B.; Dong, Y. Brightly Luminescent and Color-Tunable Colloidal $CH_3NH_3PbX_3$ (X=Br, I, Cl) Quantum Dots: Potential Alternatives for Display Technology. *ACS Nano* **2015**, *9*, 4533–4542.
4. Ling, Y.; Yuan, Z.; Tian, Y.; Wang, X.; Wang, J. C.; Xin, Y.; Hanson, K.; Ma, B.; Gao, H. Bright Light-Emitting Diodes Based on Organometal Halide Perovskite Nanoplatelets. *Adv. Mater.* **2016**, *28*, 305–311.
5. Yakunin, S.; Protesescu, L.; Krieg, F.; Bodnarchuk, M. I.; Nedelcu, G.; Humer, M.; De Luca, G.; Fiebig, M.; Heiss, W.; Kovalenko, M. V. Low-Threshold Amplified Spontaneous Emission and Lasing from Colloidal Nanocrystals of Caesium Lead Halide Perovskites. *Nat. Commun.* **2015**, *6*, 8056.
6. Zhu, H.; Fu, Y.; Meng, F.; Wu, X.; Gong, Z.; Ding, Q.; Gustafsson, M. V.; Trinh, M. T.; Jin, S.; Zhu, X-Y. Lead Halide Perovskite Nanowire Lasers with Low Lasing Thresholds and High Quality Factors. *Nat. Mater.* **2015**, *14*, 636–643.
7. Ramasamy, P.; Lim, D.-H.; Kim, B.; Lee, S.-H.; Lee, M.-S.; Lee, J.-S. All-Inorganic Cesium Lead Halide Perovskite Nanocrystals for Photodetector Applications. *Chem. Commun.* **2016**, *52*, 2067–2070.
8. Yang, T.; Zheng, Y.; Du, Z.; Liu, W.; Yang, Z.; Gao, F.; Wang, L.; Chou, K.-C.; Hou, X.; Yang, W. Superior Photodetectors Based on All-Inorganic Perovskite

$CsPbI_3$ Nanorods with Ultrafast Response and High Stability. *ACS Nano* **2018**, *12*, 1611−1617.

9. Manser, J. S.; Christians, J. A.; Kamat, P. V. Intriguing Optoelectronic Properties of Metal Halide Perovskites. *Chem. Rev.* **2016**, *116*, 12956−13008.

10. Hoefler, S. F.; Trimmel, G.; Rath, T. Progress on Lead-Free Metal Halide Perovskites for Photovoltaic Applications: A Review. *Monatshefte für Chemie-Chemical Monthly* **2017**, *148*, 795−826.

11. Shamsi, J.; Abdelhady, A. L.; Accornero, S.; Arciniegas, M.; Goldoni, L.; Kandada, A. R. S.; Petrozza, A.; Manna. L. N-Methylformamide as a Source of Methylammonium Ions in the Synthesis of Lead Halide Perovskite Nanocrystals and Bulk Crystals. *ACS Energy lett.* **2016**, *1*, 1042−1048.

12. Bekenstein, Y.; Koscher, B. A.; Eaton, S. W.; Yang, P.; Alivisatos, A. P. Highly Luminescent Colloidal Nanoplates of Perovskite Cesium Lead Halide and Their Oriented Assemblies. *J. Am. Chem. Soc.* **2015**, *137*, 16008−16011.

13. Akkerman, Q. A.; D'Innocenzo, V.; Accornero, S.; Scarpellini, A.; Petrozza, A.; Prato, M.; Manna, L. Tuning the Optical Properties of Cesium Lead Halide Perovskite Nanocrystals by Anion Exchange Reactions. *J. Am. Chem. Soc.* **2015**, *137*, 10276−10281.

14. Jang, D. M.; Park, K.; Kim, D. H.; Park, J.; Shojaei, F.; Kang, H. S.; Ahn, J. P.; Lee, J. W.; Song, J. K. Reversible Halide Exchange Reaction of Organometal Trihalide Perovskite Colloidal Nanocrystals for Full-Range Band-gap Tuning. *Nano Lett.* **2015**, *15*, 5191−5199.

15. Protesescu, L.; Yakunin, S.; Bodnarchuk, M. I.; Krieg, F.; Caputo, R.; Hendon, C. H.; Yang, R. X.; Walsh, A.; Kovalenko, M. V. Nanocrystals of Cesium Lead Halide Perovskites ($CsPbX_3$, X=Cl, Br, and I): Novel Optoelectronic Materials Showing Bright Emission with Wide Color Gamut. *Nano Lett.* **2015**, *15*, 3692−3696.

16. Tidhar, Y.; Edri, E.; Weissman, H.; Zohar, D.; Hodes, G.; Cahen, D.; Rybtchinski, B.; Kirmayer, S. Crystallization of Methyl Ammonium Lead Halide Perovskites: Implications for Photovoltaic Applications. *J. Am. Chem. Soc.* **2014**, *136*, 13249−13256.

17. Shi, D.; Adinolfi, V.; Comin, R.; Yuan, M.; Alarousu, E.; Buin, A.; Chen, Y.; Hoogland, S.; Rothenberger, A.; Katsiev, K.; Losovyj, Y.; Zhang, X.; Dowben, P. A.; Mohammed, O. F.; Sargent, E. H.; Bakr, O. M. Low Trap-State Density and Long Carrier Diffusion in Organolead Trihalide Perovskite Single Crystals. *Science* **2015**, *347*, 519−522.

18. Saidaminov, M. I.; Abdelhady, A. L.; Murali, B.; Alarousu, E.; Burlakov, V. M.; Peng, W.; Dursun, I.; Wang, L.; He, Y.; Maculan, G.; Goriely, A.; Wu, T.; Mohammed, O. F.; Bakr, O. M. High-Quality Bulk Hybrid Perovskite Single Crystals Within Minutes by Inverse Temperature Crystallization. *Nat. Commun.* **2015**, *6*, 7586.

19. Saidaminov, M. I.; Abdelhady, A. L.; Maculana, G.; Bakr, O. M. Retrograde Solubility of Formamidinium and Methylammonium Lead Halide Perovskites Enabling Rapid Single Crystal Growth. *Chem. Commun.* **2015**, *51*, 17658−17661.

20. Burschka, J.; Pellet, N.; Moon, S.-J.; Humphry-Baker, R.;Gao, P.; Nazeeruddin, M. K.; Grätzel, M. Sequential deposition as a route to high-performance perovskite-sensitized solar cells. *Nature* **2013**, *499*, 316−320.

21. Ahmadian-Yazdi, M. R.; Zabihi, F.; Habibi, M; Eslamian, M. Effects of Process Parameters on the Characteristics of Mixed-Halide Perovskite Solar Cells Fabricated by One-Step and Two-Step Sequential Coating. *Nanoscale Res. Lett.* **2016**, *11*, 408.

22. Stoumpos, C. C.; Malliakas, C. D.; Kanatzidis, M. G. Semiconducting Tin and Lead Iodide Perovskites with Organic Cations: Phase Transitions, High Mobilities, and Near-Infrared Photoluminescent Properties. *Inorg. Chem.* **2013**, *52*, 9019−9038.

23. Prochowicz, D.; Franckevičius, M.; Cieślak, A. M.; Zakeeruddin, S. M.; Grätzel, M.; Lewiński, J. Mechanosynthesis of the Hybrid Perovskite $CH_3NH_3PbI_3$: Characterization and the Corresponding Solar Cell Efficiency. *J. Mater. Chem. A* **2015**, *3*, 20772–20777.

24. Schmidt, L. C.; Pertegá, A.; González-Carrero, S.; Malinkiewicz, O.; Agouram, S.; Espallargas, G. M.; Bolink, H. J.; Galian, R. E.; Pérez-Prieto, J. Non-template Synthesis of $CH_3NH_3PbBr_3$ Perovskite Nanoparticles. *J. Am. Chem. Soc.* **2014**, *136*, 850–853.

25. Levchuk, I.; Osvet, A.; Tang, X.; Brandl, M.; Perea, J. D.; Hoegl, F.; Matt, G. J.; Hock, R.; Batentschuk, M.; Brabec, C. J. Brightly Luminescent and Color-Tunable Formamidinium Lead Halide Perovskite $FAPbX_3$ (X=Cl, Br, I) Colloidal Nanocrystals. *Nano Lett.* **2017**, *17*, 2765–2770.

26. Pan, A.; He, B, Fan, X.; Liu, Z.; Urban, J. J.; Alivisatos, A. P.; He, L.; Liu, Y. Insight into the Ligand-Mediated Synthesis of Colloidal $CsPbBr_3$ Perovskite Nanocrystals: The Role of Organic Acid, Base, and Cesium Precursors. *ACS Nano* **2016**, *10*, 7943–7954.

27. Shamsi, J.; Dang, Z.; Bianchini, P.; Canale, C.; Di Stasio, F.; Brescia, R.; Prato, M.; Manna, L. Colloidal Synthesis of Quantum Confined Single Crystal $CsPbBr_3$ Nanosheets with Lateral Size Control up to the Micrometer Range. *J. Am. Chem. Soc.* **2016**, *138*, 7240–7243.

28. Zhumekenov, A. A.; Saidaminov, M. I.; Haque, M. A.; Alarousu, E.; Sarmah, S. P.; Murali, B.; Dursun, I.; Miao, X. H.; Abdelhady, A. L.; Wu, T.; Mohammed, O. F.; Bakr, O. M. Formamidinium Lead Halide Perovskite Crystals with Unprecedented Long Carrier Dynamics and Diffusion Length. *ACS Energy Lett.* **2016**, *1*, 32–37.

29. Liu, Y.; Yang, Z.; Cui, D.; Ren, X.; Sun, J.; Liu, X.; Zhang, J.; Wei, Q.; Fan, H.; Yu, F.; Zhang, X., Zhao, C.; Liu, S. Two-Inch-Sized Perovskite $CH_3NH_3PbX_3$ (X=Cl, Br, I) Crystals: Growth and Characterization. *Adv. Mater.* **2015**, *27*, 5176–5183.

30. Nie, W.; Tsai, H.; Asadpour, R.; Blancon, J.-C.; Neukirch, A. J.; Gupta, G.; Crochet, J. J.; Chhowalla, M.; Tretiak, S.; Alam, M. A.; Wang, H.-L.; Mohite, A. D. High-Efficiency Solution-Processed Perovskite Solar Cells with Millimeter-Scale Grains. *Science* **2015**, *347*, 522–525

31. Barrows, A. T.; Pearson, A. J.; Kwak, C. K.; Dunbar, A. D. F.; Buckley, A. R.; Lidzey, D. G. Efficient Planar Heterojunction Mixed-Halide Perovskite Solar Cells Deposited via Spray-Deposition. *Energy Environ. Sci.* **2014**, *7*, 2944–2950.

32. Deng, Y.; Zheng, X.; Bai, Y.; Wang, Q.; Zhao, J.; Huang, J. Surfactant-Controlled Ink Drying Enables High-Speed Deposition of Perovskite Films for Efficient Photovoltaic Modules. *Nat. Energy* **2018**, *3*, 560–566.

33. Prochowicz, D.; Yadav, P.; Saliba, M.; Saski, M.; Zakeeruddin, S. M.; Lewiński, J.; Grätzel, M. Mechanosynthesis of Pure Phase Mixed-Cation $MA_xFA_{1-x}PbI_3$ Hybrid Perovskites: Photovoltaic Performance and Electrochemical Properties. *Sustainable Energy Fuels* **2017**, *1*, 689–693.

34. Karmakar, A.; Askar, A. M.; Bernard, G. M.; Terskikh, V. V.; Ha, M.; Patel, S.; Shankar, K.; Michaelis, V. K. Mechanochemical Synthesis of Methylammonium Lead Mixed-Halide Perovskites: Unraveling the Solid-Solution Behavior Using Solid-State NMR. *Chem. Mater.* **2018**, *30*, 2309–2321.

35. Pal, P.; Saha, S.; Banik, A.; Sarkar, A.; Biswas, K. All-Solid-State Mechanochemical Synthesis and Post-Synthetic Transformation of Inorganic Perovskite-Type Halides. *Chem. Eur. J.* **2018**, *24*, 1811–1815.

36. Jodlowski, A. D.; Yépez, A.; Luque, R.; Camocho, L.; de Miguel, G. Benign-by-Design Solventless Mechanochemical Synthesis of Three-, Two-, and One-Dimensional Hybrid Perovskites. *Angew. Chem. Int. Ed.* **2016**, *55*, 14972–14977.

37. Jana, A.; Mittal, M.; Singla, A.; Sapra, S. Solvent-Free, Mechanochemical Syntheses of Bulk Trihalide Perovskites and Their Nanoparticles. *Chem. Comm.* **2017**, *53*, 3046–3049.

38. Askar, A. M.; Karmakar, A.; Bernard, G. M.; Ha, M.; Terskikh, V. V.; Wiltshire, B. D.; Patel, S.; Fleet, J.; Shankar, K.; Michaelis, V. K. Composition-Tunable Formamidinium Lead Mixed Halide Perovskites via Solvent-Free Mechanochemical Synthesis: Decoding the Pb Environments Using Solid-State NMR Spectroscopy. *J. Phys. Chem. Lett.* **2018**, *9*, 2671−2677.

39. Protesescu, L.; Yakunin, S.; Nazarenko, O.; Dirin, D. N.; Kovalenko, M. V. Low-Cost Synthesis of Highly Luminescent Colloidal Lead Halide Perovskite Nanocrystals by Wet Ball Milling. *ACS Appl. Nano Mater.* **2018**, *1*, 1300−1308.

40. Zhou, N.; Bekenstein, Y.; Eisler, C. N.; Zhang, D.; Schwartzberg, A. M.; Yang, P.; Alivisatos, A. P.; Lewis, J. A. Perovskite Nanowire-Block Copolymer Composites with Digitally Programmable Polarization Anisotropy. *Sci. Adv.* **2019**, *5*, eaav8141.

41. Stoumpos, C. C; Kanatzidis, M. G. The Renaissance of Halide Perovskites and Their Evolution as Emerging Semiconductors. *Acc. Chem. Res.* **2015**, *48*, 2791−2802.

42. Milot, R. L.; Eperon, G. E.; Snaith, H. J.; Johnston, M. B.; Herz, L. M. Temperature-Dependent Charge-Carrier Dynamics in $CH_3NH_3PbI_3$ Perovskite Thin Films. *Adv. Funct. Mater.* **2015**, *25*, 6218−6227.

43. Steele, J. A.; Jin, H.; Dovgaliuk, I.; Berger, R. F.; Braeckevelt, T.; Yuan, H.; Martin, C.; Solano, E.; Lejaeghere, K.; Rogge, S. M. J.; *et al.* Thermal Unequilibrium of Strained Black $CsPbI_3$ Thin Films. *Science* **2019**, *365*, 679−684.

44. Amat, A.; Mosconi, E.; Ronca, E.; Quarti, C.; Umari, P.; Nazeeruddin, Md. K.; Grätzel, M.; Angelis, F. D. Cation-Induced Band-gap Tuning in Organohalide Perovskites: Interplay of Spin–Orbit Coupling and Octahedra Tilting. *Nano Lett.* **2014**, *14*, 3608−3616.

45. Whitfield, P. S.; Herron, N.; Guise, W. E.; Page, K.; Cheng, Y.Q.; Milas, I.; Crawford, M. K. Structures, Phase Transitions and Tricritical Behavior of the Hybrid Perovskite Methyl Ammonium Lead Iodide. *Sci. Rep.* **2016**, *6*, 35685.

46. Wang, Y.; Lü, X.; Yang, W.; Wen, T.; Yang, L.; Ren, X.; Wang, L.; Lin, Z.; Zhao, Y. Pressure-Induced Phase Transformation, Reversible Amorphization, and Anomalous Visible Light Response in Organolead Bromide Perovskite. *J. Am. Chem. Soc.* **2015**, *137*, 11144−11149.

47. Jaffe, A.; Lin, Y.; Beavers, C. M.; Voss, J.; Mao, W. L.; Karunadasa, H. I. High-Pressure Single-Crystal Structures of 3D Lead-Halide Hybrid Perovskites and Pressure Effects on their Electronic and Optical Properties. *ACS Cent. Sci.* **2016**, *2*, 201−209.

48. Lin, J.; Lai, M.; Dou, L.; Kley, C. S.; Chen, H.; Peng, F.; Sun, J.; Lu, D.; Hawks, S. A.; Xie, C.; Cui, F.; Alivisatos, P.; Limmer, D. t.; Yang, P. Thermochromic Halide Perovskite Solar Cells. *Nat. Mater.* **2018**, *17*, 261−267.

49. Umebayashi, T.; Asai, K.; Kondo, T.; Nakao, A. Electronic Structures of Lead Iodide Based Low-Dimensional Crystals. *Phys. Rev. B: Condens. Matter Mater. Phys.* **2003**, *67*, 155405.

50. Even, J.; Pedesseau, L.; Jancu, J.-M.; Katan, C. Importance of Spin-Orbit Coupling in Hybrid Organic/Inorganic Perovskites for Photovoltaic Applications. *J. Phys. Chem. Lett.* **2013**, *4*, 2999−3005.

51. Even, J.; Pedesseau, L.; Katan, C. Analysis of Multivalley and Multibandgap Absorption and Enhancement of Free Carriers Related to Exciton Screening in Hybrid Perovskites. *J. Phys. Chem. C* **2014**, *118*, 11566−11572.

52. Im, J.; Stoumpos, C. C.; Jin, H.; Freeman, A. J.; Kanatzidis, M. G. Antagonism between Spin−Orbit Coupling and Steric Effects Causes Anomalous Band-gap Evolution in the Perovskite Photovoltaic Materials $CH_3NH_3Sn_{1-x}Pb_xI_3$. *J. Phys. Chem. Lett.* **2015**, *6*, 3503−3509.

53. Even, J.; Pedesseau, L.; Jancu, J. M.; Katan, C. DFT and $k \cdot p$ Modelling of the Phase Transitions of Lead and Tin Halide Perovskites for Photovoltaic Cells. *Phys. Status Solidi RRL* **2014**, *8*, 31−35.

54. Saba, M.; Cadelano, M.; Marongiu, D.; Chen, F.; Sarritzu, V.; Sestu, N.; Figus, C.; Aresti, M.; Piras, R.; Lehmann, A. G.; Cannas, C.; Musinu, A.; Quochi, F.; Mura, A.; Bongiovanni, G. Correlated Electron–Hole Plasma in Organometal Perovskites. *Nat. Commun.* **2014**, *5*, 5049.

55. Tilchin, J.; Dirin, D. N.; Maikov, G. I.; Sashchiuk, A.; Kovalenko, M. V.; Lifshitz, E. Hydrogen-like Wannier-Mott Excitons in Single Crystal of Methylammonium Lead Bromide Perovskite. *ACS Nano* **2016**, *10*, 6363−6371.

56. Johnston, M. B.; Herz, L. M. Hybrid Perovskites for Photovoltaics: Charge-Carrier Recombination, Diffusion, and Radiative Efficiencies. *Acc. Chem. Res.* **2016**, *49*, 146−154.

57. Wehrenfennig, C.; Eperon, G. E.; Johnston, M. B.; Snaith, H, J.; Herz, L. M. High Charge Carrier Mobilities and Lifetimes in Organolead Trihalide Perovskites. *Adv. Mater.* **2014**, *26*, 1584–1589.

58. Zheng, K.; Zhu, Q.; Abdellah, M.; Messing, M. E.; Zhang, W.; Generalov, A.; Niu, Y.; Ribaud, L.; Canton, S. E.; Pullerits, T. Exciton Binding Energy and the Nature of Emissive States in Organometal Halide Perovskites. *J. Phys. Chem. Lett.* **2015**, *6*, 2969–2975.

59. Saba, M.; Quochi, F.; Mura, A.; Bongiovanni, G. Excited State Properties of Hybrid Perovskites. *Acc. Chem. Res.* **2016**, *49*, 166−173.

60. Yang, Y.; Yang, M.; Li, Z.; Crisp, R.; Zhu, K.; Beard, M. C. Comparison of Recombination Dynamics in $CH_3NH_3PbBr_3$ and $CH_3NH_3PbI_3$ Perovskite Films: Influence of Exciton Binding Energy. *J. Phys. Chem. Lett.* **2015**, *6*, 4688−4692.

61. Miyata, A.; Mitioglu, A.; Plochocka, P.; Portugall, O.; Wang, J. T.-W.; Stranks, S. D; Snaith, H. J.; Nicholas, R. J. Direct Measurement of the Exciton Binding Energy and Effective Masses for Charge Carriers in Organic-Inorganic Tri-Halide Perovskites. *Nat. Phys.* **2015**, *11*, 582–588.

62. Herz, L. M. Charge-Carrier Dynamics in Organic-Inorganic Metal Halide Perovskites. *Annu. Rev. Phys. Chem.* **2016**, *67*, 65–69.

63. Li, M.; Bhaumik, S.; Goh, T. W.; Kumar, M. S.; Yantara, N.; Grätzel, M.; Mhaisalkar, S.; Mathews, N.; Sum, T. C. Slow Cooling and Highly Efficient Extraction of Hot Carriers in Colloidal Perovskite Nanocrystals. *Nat. Commun.* **2017**, *8*, 14350.

64. Butkus, J. Vashishtha, P.; Chen, K.; Gallaher, J. K.; Prasad, S. K. K.; Metin, D. Z.; Laufersky, G.; Gaston, N.; Halpert, J. E.; Hodgkiss, J. M. The Evolution of Quantum Confinement in $CsPbBr_3$ Perovskite Nanocrystals. *Chem. Mater.* **2017**, *29*, 3644−3652.

65. Li, M.; Begum, R.; Fu, J.; Xu, Q.; Koh, T. M.; Veldhuis, S. A.; Grätzel, M.; Mathews, N.; Mhaisalkar, S.; Sum, T. C. Low Threshold and Efficient Multiple Exciton Generation in Halide Perovskite Nanocrystals. Nat. Commun. **2018**, *9*, 4197.

66. Tanaka, K. Takahashi, T.; Ban, T.; Kondo, T.; Uchida, K.; Miura, N. Comparative Study on the Excitons in Lead-Halide-Based Perovskite-Type Crystals $CH_3NH_3PbBr_3$ $CH_3NH_3PbI_3$. *Solid State Commun.* **2003**, *127*, 619−623.

67. Kojima, A.; Teshima, K.; Shirai, Y.; Miyasaka, T. Organometal Halide Perovskites as Visible-Light Sensitizers for Photovoltaic Cells. *J. Am. Chem. Soc.* **2009**, *131*, 6050−6051.

68. https://www.nrel.gov/pv/assets/pdfs/best-research-cell-efficiencies.20191106.pdf

69. Jacobsson, T. J.; Correa-Baena, J.-P.; Pazoki, M.; Saliba, M.; Schenk, K.; Grätzel, M.; Hagfeldt, A. Exploration of the Compositional Space for Mixed Lead Halogen Perovskites for High Efficiency Solar Cells. *Energy Environ. Sci.* **2016**, *9*, 1706−1724.

70. Bi, D.; Tress, W.; Dar, M. I.; Gao, P.; Luo, J.; Renevier, C.; Schenk, K.; Abate, A.; Giordano, F.; Correa Baena, J.-P.; *et al.* Efficient Luminescent Solar Cells Based on Tailored Mixed-Cation Perovskites. *Sci. Adv.* **2016**, *2*, e1501170.

71. Zhang, H.; Ren, X.; Chen, X.; Mao, J.; Cheng, J.; Zhao, Y.; Liu, Y.; Milic, J.; Yin, W.-J.; Grätzel, M.; Choy, W. C. H. Improving the Stability and Performance of

Perovskite Solar Cells via Off-the-Shelf Post-Device Ligand Treatment. *Energy Environ. Sci.* **2018**, *11*, 2253–2262.

72. Lee, J.-W.; Kim, H.-S.; Park, N.-G. Lewis Acid-Base Adduct Approach for High Efficiency Perovskite Solar Cells. *Acc. Chem. Res.* **2016**, *49*, 311–319.

73. Zuoa, C.; Ding, L. An 80.11% FF Record Achieved for Perovskite Solar Cells by Using the NH_4Cl Additive. *Nanoscale* **2014**, *6*, 9935–9938.

74. Bai, Y.; Dong, Q.; Shao, Y.; Deng, Y.; Wang, Q.; Shen, L.; Wang, D.; Wei, W.; Huang, J. Enhancing Stability and Efficiency of Perovskite Solar Cells with Crosslinkable Silane-Functionalized and Doped Fullerene. *Nat. Commun.* **2016**, *7*, 12806.

75. Hermes, I. M.; Hou, Y.; Bergmann, V. W.; Brabec, C. J.; Weber, S. A. L. The Interplay of Contact Layers: How the Electron Transport Layer Influences Interfacial Recombination and Hole Extraction in Perovskite Solar Cells. *J. Phys. Chem. Lett.* **2018**, *9*, 6249−6256.

76. Ye, Q.-Q.; Wang, Z.-K.; Li, M.; Zhang, C.-C.; Hu, K.-H.; Liao, L.-S. N-Type Doping of Fullerenes for Planar Perovskite Solar Cells. *ACS Energy Lett.* **2018**, *3*, 875−882.

77. Cho, K. T.; Paek, S.; Grancini, G.; Roldán-Carmona, C.; Gao, P.; Lee, Y.; Nazeeruddin, M. K. Highly Efficient Perovskite Solar Cells with a Compositionally Engineered Perovskite/Hole Transporting Material Interface. *Energy Environ. Sci.* **2017**, *10*, 621−627.

78. Yuan, Y.; Huang, J.; Ion Migration in Organometal Trihalide Perovskite and Its Impact on Photovoltaic Efficiency and Stability. *Acc. Chem. Res.* **2016**, *49*, 286−293.

79. Zhang, H.; Fu, X.; Tang, Y.; Wang, H.; Zhang, C.; Yu, W. W.; Wang, X.; Zhang, Y.; Xiao, M. Phase Segregation due to Ion Migration in All-Inorganic Mixed-Halide Perovskite Nanocrystals. *Nat. Commun.* **2019**, *10*, 1088.

80. Cho, H.; Jeong, S.-H.; Park, M.-H.; Kim, Y.-H.; Wolf, C.; Lee, C. L.; Heo, J. H.; Sadhanala, A.; Myoung, N. Yoo, S.; *et al.* Overcoming the Electroluminescence

Efficiency Limitations of Perovskite Light-Emitting Diodes. *Science* **2015**, *350*,1222−1225.

81. Li, G.; Tan, Z.-K.; Di, D.; Lai, M. L.; Jiang, L.; Lim, J. H.-W.; Friend, R. H.; Greenham, N. C. Efficient Light-Emitting Diodes Based on Nanocrystalline Perovskite in a Dielectric Polymer Matrix. *Nano Lett.* **2015**, *15*, 2640−2644.

82. Shi, Z.-F.; Sun, X.-G.; Wu, D.; Xu, T.-T.; Tian, Y.-T.; Zhang, Y.-T.; Li, X.-J.; Du, G.-T. Near-Infrared Random Lasing Realized in a Perovskite $CH_3NH_3PbI_3$ Thin Film. *J. Mater. Chem. C* **2016**, *4*, 8373−8379.

83. Xing, G.; Mathews, N.; Lim, S. S.; Yantara, N.; Liu, X.; Sabba, D.; Grätzel, M.; Mhaisalkar, S.; Sum, T. C. Low-Temperature Solution-Processed Wavelength-Tunable Perovskites for Lasing. *Nat. Mater.* **2014**, *13*, 476−480.

84. Liu, Z.; Yang, J.; Du, J.; Hu, Z.; Shi, T.; Zhang, Z.; Liu, Y.; Tang, X.; Leng, Y.; Li, R. Robust Subwavelength Single-Mode Perovskite Nanocuboid Laser. *ACS Nano* **2018**, *12*, 5923−5931.

85. Zhang, Q.; Su, R.; Liu, X.; Xing, J.; Sum, T. C.; Xiong, Q. High-Quality Whispering-Gallery-Mode Lasing from Cesium Lead Halide Perovskite Nanoplatelets. *Adv. Funct. Mater.* **2016**, *26*, 6238–6245.

86. Wang, K.; Sun, W.; Li, J.; Gu, Z.; Xiao, S.; Song, Q. Unidirectional Lasing Emissions from $CH_3NH_3PbBr_3$ Perovskite Microdisks. *ACS Photonics* **2016**, *3*, 1125−1130.

87. Wang, Y.; Li, X.; Nalla, V.; Zeng, H.; Sun, H. Solution-Processed Low Threshold Vertical Cavity Surface Emitting Lasers from All-Inorganic Perovskite Nanocrystals. *Adv. Funct. Mater.* **2017**, *27*, 1605088.

88. Huang, C.-Y.; Zou, C.; Mao, C.; Corp, K. L.; Yao, Y.-C.; Lee, Y.-J.; Schlenker, C. W.; Jen, A. K. Y.; Lin, L. Y. $CsPbBr_3$ Perovskite Quantum Dot Vertical Cavity Lasers with Low Threshold and High Stability. *ACS Photonics* **2017**, *4*, 2281−2289.

Chapter 2

Experiments

Abstract

This chapter discusses different experimental methods and instrumentation techniques used in this study. A brief overview on the significance of synthesis and characterization of perovskites is followed by the Materials section. Different experimental methods used to synthesize or prepare perovskite samples are discussed in the Methods section. Here, I discuss the preparation of perovskite pellets, nanocrystals, microcrystals, and thin films. Pellets of methylammonium lead halide and bromide-iodide heterojunction perovskites are prepared by using piezochemical synthesis. Similarly, nanocrystals of methylammonium, formamidinium, and cesium lead bromide perovskites are prepared by using the ligand-assisted reprecipitation and hot-injection methods. On the other hand, methylammonium lead halide microcrystals are obtained from the antisolvent vapor assisted crystallization. The thin films of perovskite nanocrystals are prepared by drop-casting the dilute solution of the samples on a glass substrate. The prepared perovskite samples are characterized and studied by using various spectroscopic and microscopic techniques, which are discussed in the Instrumentation section of this chapter. The excitonic bands and the optical band-gaps of perovskite nanocrystals and pellets are characterized by using UV-Vis absorption and diffuse reflectance spectroscopy, respectively. The photoluminescence properties and charge carrier dynamics of perovskite samples are studied by using steady-state and time-resolved photoluminescence spectroscopy, transient absorption spectroscopy, and single-particle microspectroscopy. Also, the crystal structure and morphology of perovskite samples are elucidated by using X-ray diffraction and transmission electron microscopy.

The intriguing optoelectronic properties of lead halide perovskites and their promising applications in light-harvesting and light-emitting systems have lured scientists to synthesize them in different dimensions and sizes by following different methods and characterize them using various spectroscopic and microscopic techniques.[1-3] Different dimensional nanoscopic, microscopic and large size organic-inorganic hybrid ($MAPbX_3$ and $FAPbX_3$) and all-inorganic ($CsPbX_3$) lead halide perovskites are prepared from their precursor salts, MAX, FAX, CH_3COOCs or CsX and PbX_2, which are commercially inexpensive and easy to handle. Besides, the synthesis methods are facile and versatile. For instance, both nano and microcrystals of lead halide perovskites can be prepared from the same precursor solution when two different synthesis methods, LARP[4] and AVC,[5] respectively are used. Therefore, owing to the easily available precursors and simple synthesis methods, the study of different types of lead halide perovskites concerning their fundamental properties and applications has become straightforward.

The optoelectronic properties of lead halide perovskites vary with respect to their size, dimension, chemical and stoichiometric composition, and crystal structure. For instance, a 3D PNC shows different optical and charge carrier properties when compared to its 2D counterpart, which is due to the strong quantum confinement effect in the later.[6] Also, the optical band-gaps of lead halide perovskites are dependent upon the halogen composition, since the VBM is governed by the electronic structure of $[PbX_6]^{4-}$ octahedra.[2,3] The crystal structure of these materials may vary as orthorhombic, cubic, and tetragonal when the synthesis temperature and halogen composition are changed.[1-5] Therefore, the first-hand characterization of lead halide perovskites by employing different microscopic and spectroscopic techniques such as TEM, SEM, UV-Vis absorption and diffuse reflectance spectroscopy, PL spectroscopy, XRD, EDX, and XPS becomes crucial.

In this study, I prepared pellets, microcrystals, nanocrystals, and films of lead halide perovskites by using various solid state and solution-processed methods to study their PL properties and charge carrier and energy transfer dynamics.[7-9] A piezochemical synthesis method is used to prepare the pellets of pristine $MAPbX_3$ (X = Cl, Br, I) and mixed bromide-iodide ($MAPbBr_{3-x}I_x$) heterojunction perovskites.[7] Similarly, micro and nanocrystals of $MAPbX_3$ (X = Cl, Br) and $FAPbBr_3$ and $CsPbBr_3$ perovskites are

synthesized by employing the AVC, LARP, and hot-injection methods.[4,5,8-12] The PNCs are assembled into thin films by drop-cast technique. The synthesized perovskite materials are characterized by using UV-Vis absorption spectroscopy, diffuse reflectance spectroscopy, steady-state PL spectroscopy, fluorescence microscopy, TEM, and XRD. Further, the charge carrier and energy transfer dynamics in these materials and their assemblies are studied by using a time-resolved PL spectroscopy, transient absorption spectroscopy, and single-particle microspectroscopy.

2.1 Materials

Various materials involved in the study are MACl (TCI, >98.0%), MABr (TCI, >98.0%), MAI (TCI, >98.0%), FABr (TCI, >98.0%), CH_3COOCs (Sigma-Aldrich, 99.9%), $PbCl_2$ (Sigma-Aldrich, 98%), $PbBr_2$ (Sigma-Aldrich, ≥98%), PbI_2 (Sigma-Aldrich, 99%), hexadecylamine ($C_{16}H_{35}N$, TCI, >95.0%), *n*-octylamine hydrobromide ($C_8H_{17}NH_3Br$, TCI, >98.0%), oleic acid ($C_{18}H_{34}O_2$, TCI, >85.0%), dehydrated DMF (Fujifilm Wako), dehydrated toluene (Fujifilm Wako, >99.5%), acetone (Fujifilm Wako), DCM (Fujifilm Wako, >99.5%), 1-octadecene (TCI, >90.0%), 1-hexadecene (Fujifilm Wako), hexane (Fujifilm Wako, >96.0%), *n*-butanol (Fujifilm Wako, >99.0%), and cover glasses (Matsunami, 24 mm×50 mm or 18 mm×18 mm, thickness 0.13–0.17 mm). The chemicals were used as received.

2.2 Methods

2.2.1 Piezochemical Synthesis of Perovskite Pellets

Closely-packed pellets of $MAPbX_3$ perovskites were prepared by using a novel piezochemical synthesis method,[7] where pressure was applied to the solid mixture of precursor salts to obtain perovskites (Figure 2.1). The study of piezochemically

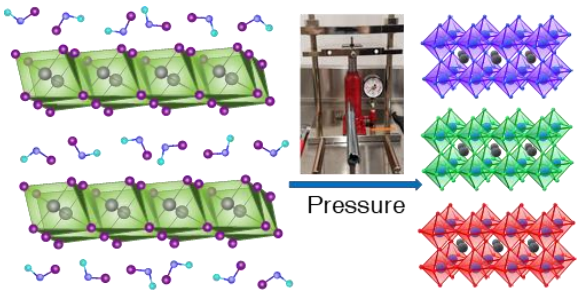

Figure 2.1 A scheme of piezochemical synthesis of $MAPbX_3$ perovskites.

synthesized perovskite samples is presented in Chapter 3. In a typical synthesis, PbX_2 (1.35 mmol) and MAX (1.25 mmol) were crushed separately into a fine powder using a hand mortar and thoroughly mixed in a glass vial to obtain a precursor solid mixture. The solid mixture was filled inside a silicon chamber (20 mm in diameter) placed on a metal plate, which was followed by applying a pressure of 2.4 GPa using a hydraulic jack. After 30 min, the pressure was released to obtain disk-shaped perovskite pellets. Here, I also studied the effect of pressure by synthesizing perovskites pellets at 1.2, 3.6, 4.8, and 6 GPa.

The piezochemical synthesis method was extended to obtain $MAPbBr_{3-x}I_x$ perovskites with the mixed halide composition. In the typical synthesis, I prepared a precursor solid mixture from $PbBr_2$ (0.75 mmol), MABr (0.75 mmol) and PbI_2 (0.25 mmol). To this precursor solid mixture, a pressure of 2.4 GPa was applied for 30 min to obtain a $MAPbBr_{3-x}I_x$ perovskite pellet. Amounts of precursors used during the reactions are tabulated in Table 2.1.

Table 2.1 Amounts of precursors used for the piezochemical synthesis of $MAPbX_3$ and $MAPbBr_{3-x}I_x$ perovskite pellets.

S.N.	Samples	Precursors	mmol (mg)
1.	$MAPbCl_3$	$PbCl_2$	1.35 (375)
		MACl	1.25 (85)
2.	$MAPbBr_3$	$PbBr_2$	1.35 (500)
		MABr	1.25 (140)
3.	$MAPbI_3$	PbI_2	1.35 (622)
		MAI	1.25 (199)
4.	$MAPbBr_xI_{3-x}$	$PbBr_2$	0.75 (275)
		MABr	0.75 (84)
		PbI_2	0.25 (115)

2.2.2 Synthesis of Perovskite Microcrystals

$MAPbBr_3$ perovskite microcrystals were prepared by the AVC method (Figure 2.2)**.**[8,12] The study of $MAPbBr_3$ microcrystals is presented in Chapters 3 and 5. During the synthesis, the precursor salts, MABr (211 mg, 1.88 mmol) and $PbBr_2$ (690 mg, 1.88 mmol), were dissolved separately in 5 mL dehydrated DMF. Equal volumes (1 mL each) of these solutions were mixed to form a precursor solution. I drop-cast this precursor solution (50 µL) on an 18×18 mm^2 glass coverslip, which was placed on a silicon stage in a solvent chamber. The chamber contained DCM leveled below the

silicon stage, and the mouth of the chamber was covered with a lid for controlled evaporation of the precursor solution. Over 12 h, microcrystals were formed on the glass coverslip.

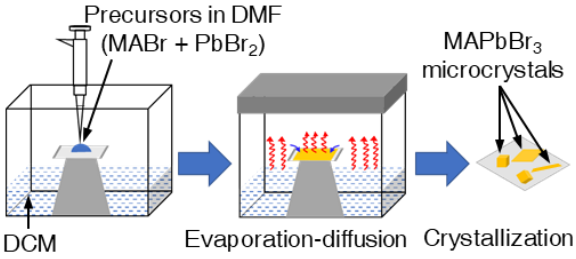

Figure 2.2 AVC method for the synthesis of $MAPbBr_3$ perovskite microcrystals.

2.2.3 Synthesis of Perovskite Nanocrystals

Synthesis of $FAPbBr_3$ PNCs

$FAPbBr_3$ PNCs were synthesized by the modified LARP method,[8-10] and the study of these samples is presented in Chapter 4. Precursor solutions were prepared by dissolving FABr (25 mg, 0.20 mmol) and $PbBr_2$ (73 mg, 0.20 mmol), separately in dehydrated DMF. Similarly, octylammonium bromide (25 mg, 0.12 mmol) and oleic acid (190 µL, 0.60 mmol) were dissolved in 1-octadecene (4 mL) with continuous stirring at 80 °C. The precursor solutions were added concomitantly to the above ligand solution, which was followed by precipitation of PNCs by the addition of either acetone or a mixture of hexane and acetone (8:1, v/v). The precipitate of $FAPbBr_3$ PNCs were collected by centrifugation at 7000 rpm for 10 min. For the thin film deposition and single-particle studies, colloidal solution of PNCs was used, whereas the dry precipitate was studied as the clusters of PNCs.

Synthesis of $MAPbBr_3$ PNCs

$MAPbBr_3$ PNCs were synthesized by the LARP method[5,8] (Figure 2.3), and the study of these samples is presented in chapter 4. In a typical synthesis, MABr (28 mg, 0.25 mmol), $PbBr_2$ (100 mg, 0.27 mmol), oleic acid (80 µL, 0.25 mmol) and hexadecyl (46 mg, 0.19 mmol) were dissolved in 1 mL DMF by alternate stirring and warming on a water bath at 60 °C, until a clear precursor solution was obtained. This solution was injected into 50 mL dehydrated toluene with vigorous stirring. The solution turned into green, and with mixing, it gradually changed into an orange-yellow turbid solution,

indicating the precipitation of PNCs. After 15 minutes of vigorous stirring, the solution was centrifuged at 10,000 rpm for 5 minutes, and the clear supernatant was discarded. The precipitate was washed with *n*-butanol to remove excess ligands. It was dispersed in toluene by sonication and centrifuged at 5000 rpm for 5 minutes to separate larger particles. $MAPbBr_3$ PNCs in the supernatant were used in the further study.

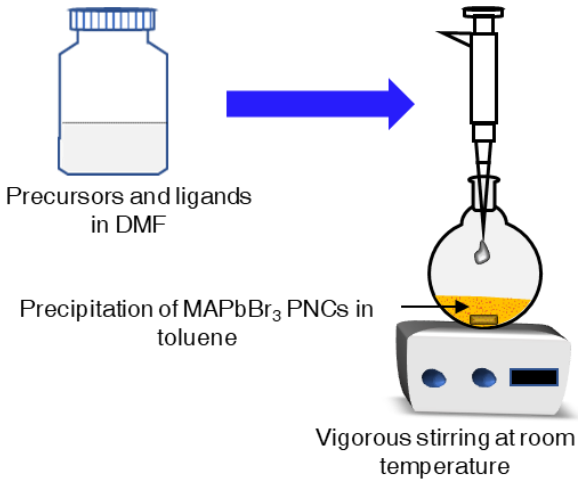

Figure 2.3 LARP method for the synthesis of $MAPbBr_3$ PNCs.

Synthesis of $CsPbBr_3$ PNCs

$CsPbBr_3$ PNCs were synthesized by the hot-injection method[8,11] (Figure 2.4**),** and the

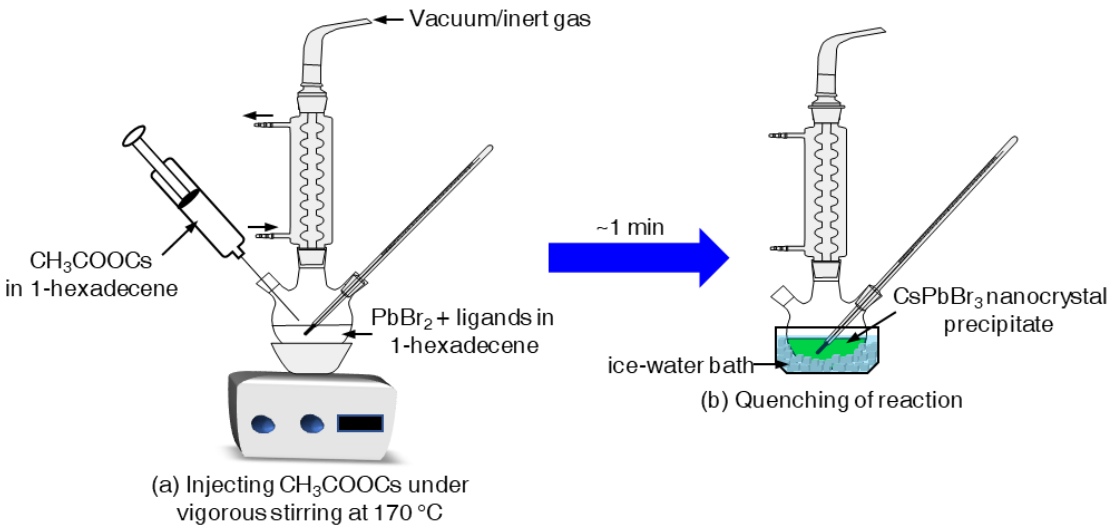

Figure 2.4 Hot-injection method for the synthesis of $CsPbBr_3$ PNCs.

study of these samples is presented in Chapter 4. In a typical synthesis, a mixture of $PbBr_2$ (690 mg, 1.88 mmol), oleic acid (4 mL, 12.6 mmol), hexadecylamine (3670 mg,

15.2 mmol), and 1-hexadecene (90 mL) was loaded in a 500 mL two-neck flask and dried under vacuum at 120 °C for 1 h with stirring. In parallel, CH_3COOCs (9 mg, 0.5 mmol) dissolved in a mixture of oleic acid (1 mL, 3.15 mmol) and 1-hexadecene (10 mL) was dried at 120 °C under vacuum with stirring. Argon was flushed alternately with the vacuum at every 20 mins while drying. After the complete dissolution of $PbBr_2$, the temperature was raised to 170 °C under Argon atmosphere. To this hot, vigorously stirring solution, dried CH_3COOCs solution was injected under Argon. Within 1 min of injection, the reaction was quenched by placing the reaction mixture in an ice-water bath. The reaction mixture was centrifuged at 6000 rpm for 25 min and a yellowish supernatant was discarded. The precipitate was collected, washed with hexane and *n*-butanol, and dispersed in toluene for further studies.

2.2.4 Thin Film Deposition of Perovskite Nanocrystals

I used drop-cast technique to deposit the thin films of PNCs in toluene. The study of PNC film samples is presented in Chapter 4. As shown in Figure 2.5, PNC solution was drop-cast in a silicon chamber fixed on a 24×50 mm^2 glass coverslip. I prepared close-

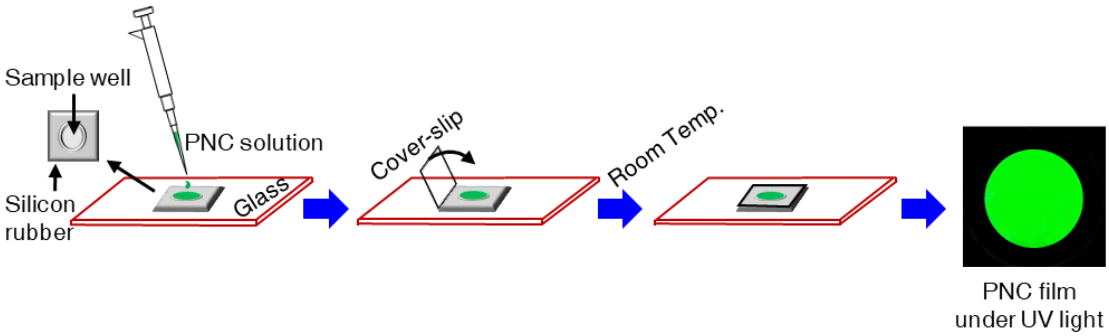

Figure 2.5 Schematic illustration of thin film deposition of PNCs.

packed or loose-packed PNC films by controlling the amounts of nanocrystals in the depositing solution. A close-packed film was prepared by depositing 50 µL sample from a stock PNC solution (1 mg mL^{-1}). Loose-packed films with different particle densities were prepared by depositing solutions with 500, 250, 125, 62 µg mL^{-1} PNCs.[8]

2.2.5 Preparation of $MAPbBr_3$/$MAPbCl_3$ Double Layer Perovskite Structure

A double layer perovskite structure was prepared by depositing $MAPbBr_3$ PNCs on a $MAPbCl_3$ microcrystal film. A $MAPbCl_3$ microcrystal film was prepared by drop-

casting a precursor solution composed of MACl (85 mg, 1.25 mmol) and $PbCl_2$ (375 mg, 1.35 mmol) dissolved in 1 mL anhydrous DMF on a 24×50 mm^2 glass coverslip.[8] The study of these samples is presented in Chapter 4.

2.2.6 Preparation of C_{60}-doped Thin Film of Perovskite Nanocrystals

To the PNC stock solution (1 mg mL^{-1} in toluene), 1.4 weight% of C_{60} (14 µg) was added, and the mixture was sonicated for 30 min. The stock solution containing C_{60} was further diluted 10 times with toluene. Thin films of C_{60}-doped PNCs were prepared by drop-casting 100 µL of the dilute solution on 24×50 mm^2 glass coverslips and drying.[9] The study of these samples is presented in Chapter 5.

2.3 Instrumentation

2.3.1 UV-Vis Absorption and Diffuse Reflectance Spectroscopy

To characterize the excitonic features and band-gaps of the lead halide perovskites, UV-Vis absorption and diffuse reflectance spectroscopy were carried out in a UV-Vis

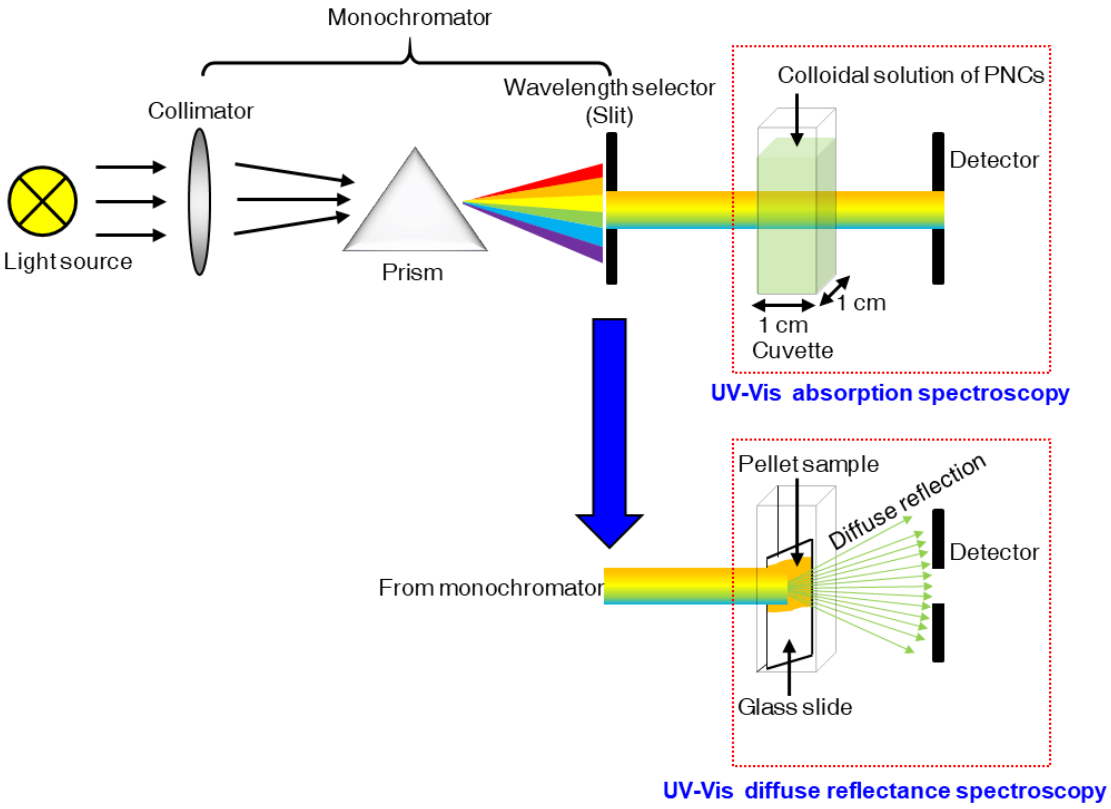

Figure 2.6 Schematic illustration of UV-Vis absorption and diffuse reflectance spectroscopy for PNC solutions and perovskite pellets, respectively.

spectrophotometer (Evolution 220, Thermo Fischer Scientific). A scheme for the UV-Vis absorption and diffuse reflectance spectroscopy used in this study is shown in Figure 2.6. UV-Vis absorption spectra were measured for the colloidal solutions of PNCs; and since the light cannot penetrate through thick perovskite pellets, diffuse reflectance spectra were estimated for such samples in a customized reflectance geometry as shown in the lower panel of Figure 2.6.

The band-gaps of PNCs and perovskite pellets were estimated from the corresponding Tauc plot of absorption spectra and the diffused reflectance spectra, respectively. The incident photon energy ($h\upsilon$) and E_g are related to the absorption coefficient (α) by the equation $[\alpha h\upsilon]^2 = a(h\upsilon\text{-}E_g)$ and the transformed Kubelka-Munk (diffuse reflectance) function by the equation $[F(R)h\upsilon]^2 = a(h\upsilon\text{-}E_g)$, where R is the percentage of reflected light, h is Plank's constant, υ is the frequency of light, and a is the proportionality constant associated with the direct allowed transition.[13]

2.3.2 Steady-state PL Spectroscopy

The steady-state PL spectroscopy was used to characterize the emission color from the PNCs by using a fluorescence spectrophotometer (F-4500, Hitachi). A scheme for the optical setup and working principle of fluorescence spectrophotometer is shown in

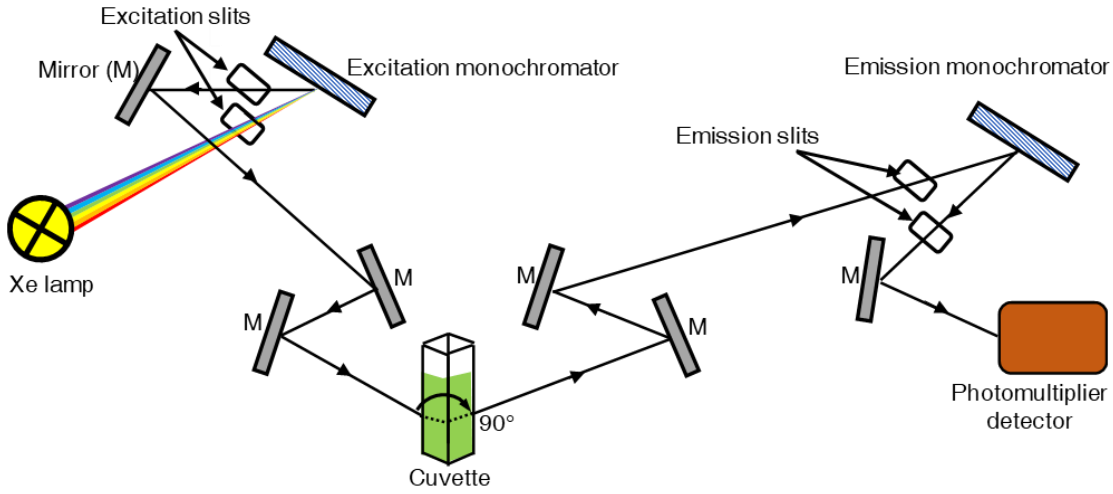

Figure 2.7 Optical setup and working principle of steady-state PL spectroscopy.

Figure 2.7. Xe lamp was used as the light source, and the PL spectra were obtained by setting the excitation wavelength to 365 nm and scanning the emission monochromator. In steady-state PL spectroscopy, the PL is collected at an angle of 90° from the

excitation light in order to avoid any transmitted light in the spectra.

2.3.3 Time-resolved PL Spectroscopy

I used time-resolved PL spectroscopy to study the PL lifetime (τ), excitation power-dependent PL and ASE of PNCs, clusters, PNC thin films, and single microcrystals. Similarly, the technique was also utilized to study the PL properties of perovskite pellets and large single crystals. A schematic illustration of the optical setup for the time-resolved PL measurement is shown in Figure 2.8.

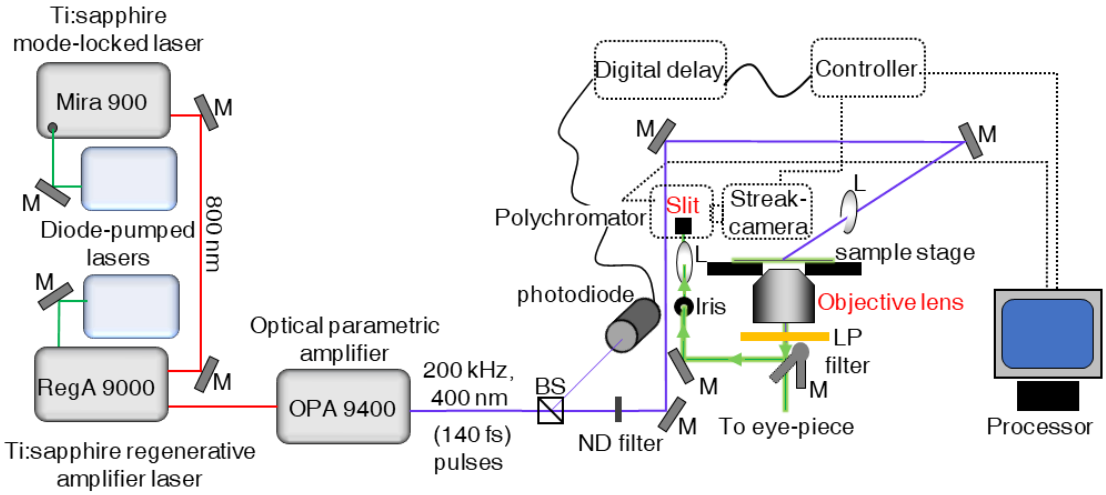

Figure 2.8 Optical setup for the time-resolved PL spectroscopy of perovskite pellets, clusters, microcrystals and PNC films.

The excitation light source used for time-resolved PL spectroscopy was a 400 nm wavelength femtosecond laser with a pulse width of 140 fs. The amplified femtosecond pulses were generated at a 200 kHz repetition rate from the second harmonic generator (SHG) crystal of an optical parametric amplifier (Coherent OPA 9400), which was pumped by an 800 nm output from a Ti:sapphire regenerative amplifier (Coherent RegA 9000). RegA was seeded by a mode-locked Ti:sapphire laser (Coherent Mira 900F). Spectral and time-resolved photocounts were recorded using an assembly of a polychromator (model 250IS, Chromex) and a photon-counting streak-camera (model C4334, Hamamatsu).

The PL signals from the perovskite samples on a glass substrate, placed over a movable stage in an inverted microscope (Olympus IX70), were passed through an

objective lens (40×, NA 0.60, Olympus), filtered through a 440 nm long-pass filter, and focused using a lens at the entrance slit of the polychromator. The signals were detected using the streak-camera (Figure 2.8). For the colloidal solution of PNCs, PL signals were collected by placing a cuvette containing the PNC solution in the excitation laser path. A lens was used to focus the laser into the colloidal solution, and a mirror was used to reflect the PL signals at a right angle from the cuvette to the entrance slit of the polychromator. For the power-dependent studies, the laser power was varied by using neutral density filters. For ASE measurements and PL studies of large single crystals, an iris was used before the entrance slit of the polychromator for collecting the emission from isolated microcrystal.

Multiexponential tail-fits of the PL decay profiles were performed and the average PL lifetime (τ_{av}) was calculated using the equation,

$$\tau_{av} = \frac{\tau_1 A_1 + \tau_2 A_2 + \tau_3 A_3}{A_1 + A_2 + A_3} \quad (2.1),$$

where A_1, A_2 and A_3 are the amplitudes, and τ_1, τ_2 and τ_3 are the PL lifetime values of 1st, 2nd and 3rd components of the exponential fit, respectively.

2.3.4 PL Masking and Unmasking System

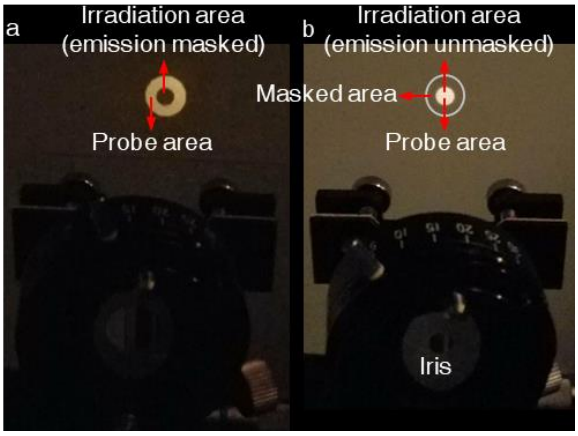

Figure 2.9 Optical masking and unmasking experiment. (a) Masking of PL from the central irradiated area by opening the iris to 150 µm diameter and collecting PL from outer non-irradiated area by placing a 50 µm diameter mask on the emission side. (b) Collecting PL from the central irradiated area by closing the iris to 50 µm diameter and removing the mask. The iris and mask were placed in between the sample and the detector.

As shown in Figure 2.9, I carried out the selected area time-resolved PL measurements of the PNC film by collecting the photons through the assembly of an iris and a circular mask. Here, the central area was always irradiated with either low- or high-intensity laser. During the collection of PL from the outer area, 50 μm diameter mask was inserted on the emission side. During the collection of PL from the irradiated area, the iris was set at the circumference of the mask and the mask was removed.

2.3.5 Single-particle Microspectroscopy

I used single-particle microspectroscopy to study the PL properties and photostability of isolated $FAPbBr_3$ PNCs on a substrate. Using this technique, I estimated and compared the time-traced total number of photons emitted by more than 500 single $FAPbBr_3$ PNCs when they were periodically excited at different pulse energies by modulating a 400 nm femtosecond laser ON and OFF. The optical setup

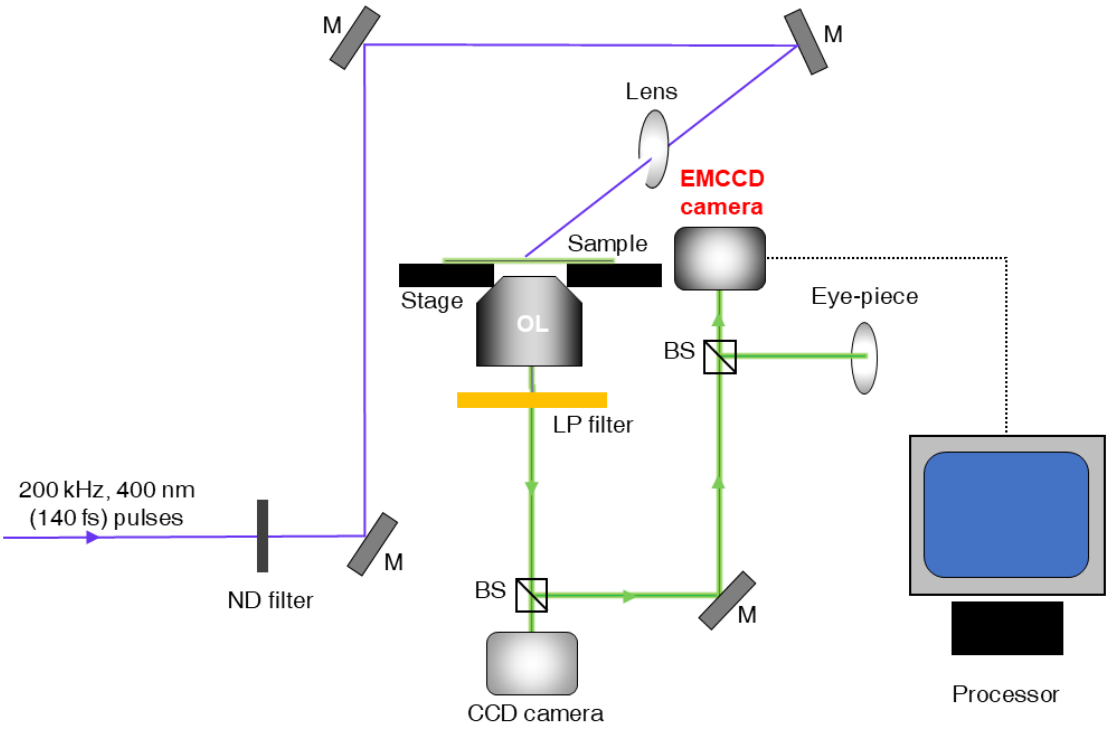

Figure 2.10 Optical setup for the single-particle micro-spectroscopy.

for the experiment is shown in Figure 2.10. Samples for the single-particle microspectroscopy were prepared by drop-casting of a dilute solution (ca. 1 ng/mL) of $FAPbBr_3$ PNCs on 18 mm×18 mm glass coverslips. Single-particle PL trajectories were

recorded at 33 ms frame rate in an inverted optical microscope (IX70, Olympus), which was equipped with an objective lens (40×, NA 0.60, Olympus), a 440 nm long-pass filter, and an EMCCD camera (iXon, Andor Technology).

2.3.6 Transient Absorption Spectroscopy

The transient absorption spectra were measured using a femtosecond pump-probe technique. The samples were excited at 400 nm with an average power of 10 μW using second harmonics from a laser (Solstice, Spectra-Physics). The pump pulse was focused to a spot with 0.7 mm diameter, and a repetition rate of 250 Hz was achieved by using an optical chopper (model 3502, New Focus). The transient absorption was probed using the supercontinuum from a CaF_2 plate. Detection was carried out using a C-MOS detector (PMA-20, Hamamatsu-Photonics). The temporal resolution was 100 fs.

2.3.7 Powder X-ray Diffraction

To characterize the crystalline phase of perovskites, I carried out powder XRD measurements of PNC samples and perovskite pellets in an X-ray diffractometer (RINT 2200, Rigaku), and I compared the obtained XRD spectra to the reference spectra from the literature to confirm the crystal structure. I prepared the samples for XRD measurements by crushing the perovskite samples into a fine powder using a hand mortar and drying it in a vacuum for 5 h. For each measurement, about 30 mg of powdered perovskite samples were used to disperse on a sample holder.

In the X-ray diffractometer, X-rays were generated in a cathode ray tube by bombarding the Cu target with accelerated electrons. Monochromatic CuKα1 radiation with wavelength 1.5406 Å was filtered, collimated and directed towards the sample, and the scanning was performed by rotating the sample and the detector in a range of 2θ angles. Here, the random orientation of the powdered sample resulted in the diffraction of X-rays in all possible directions of the lattice, which was recorded by the detector to produce a set of diffraction spectra.

The powder XRD measurement utilizes the Bragg's diffraction law $n\lambda=2d\sin\theta$, where λ is the wavelength of X-ray, θ is the diffraction angle, d is the lattice spacing in a crystalline sample and n is a positive integer. The interaction of the incident

monochromatic X-rays with the crystalline powder sample produces constructive interference when the conditions satisfy the Bragg's law. This results in diffraction peaks in the XRD spectra.

2.3.8 Electron Microscopy

I characterized the size and morphology of the PNCs by recording the TEM images in a transmission electron microscope (HD-2000, Hitachi) operated at 200 kV. Samples for TEM imaging were prepared by placing PNCs dispersed in toluene (dilute solution) on carbon-coated TEM grids (STEM Cu100P) and drying the grids inside a vacuum chamber overnight. I also estimated the size distribution of PNCs by analyzing the TEM images using ImageJ software.

In summary, I synthesized different types of lead halide perovskites, which include pellets, nanocrystals, microcrystals, and thin films, by using a solid state and different solution-processed methods. I introduced piezochemical synthesis as a new method to prepare $MAPbX_3$ and mixed halide $MAPbBr_{3-x}I_x$ perovskite pellets. This is a solvent-less solid state method for synthesizing perovskites where the pressure acts as the reaction driving force. PNCs, microcrystals, and thin films were prepared from solution-processed methods. Here, I synthesized PNCs by applying LARP and hot-injection methods. On the other hand, I prepared perovskite microcrystals from AVC technique. For the synthesis of nanocrystals, ligands such as oleic acid, hexadecyl amine, and octylammonium bromide were used to control the crystal size. I also prepared the thin films of lead halide perovskites, which was by drop-casting the colloidal solution of PNCs at the different concentration on the glass substrate.

Furthermore, I characterized and studied the perovskite samples by using UV-Vis absorption and diffuse reflectance spectroscopy, steady-state and time-resolved PL spectroscopy, transient absorption spectroscopy, single-particle microspectroscopy, powder XRD and TEM. I estimated the optical band-gaps of perovskite pellets and nanocrystals from the UV-Vis absorption and diffuse reflectance spectra. Similarly, I studied the PL and charge carrier dynamics of perovskite samples by using steady-state and time-resolved PL spectroscopy and transient absorption spectroscopy. Single-particle microspectroscopy was used to study the PL properties and photostability of perovskites at their single-particle level. The crystal structure and morphology of

perovskite samples were revealed by the powder XRD and TEM, respectively.

References

1. Dong, Q.; Fang, Y.; Shao, Y.; Mulligan, P.; Qiu, J.; Cao, L.; Huang, J. Electron-Hole Diffusion Lengths >175 μm in Solution-Grown $CH_3NH_3PbI_3$ Single Crystals. *Science* **2015**, *347*, 967–970.

2. Quan, L. N.; Rand, B. P.; Friend, R. H.; Mhaisalkar, S. G.; Lee, T.-W.; Sargent, E. H. Perovskites for Next-Generation Optical Sources. *Chem. Rev.* **2019**, *119*, 7444−7477.

3. Shamsi, J.; Urban, A. S.; Imran, M.; Trizio, L. D.; Manna, L. Metal Halide Perovskite Nanocrystals: Synthesis, Post-Synthesis Modifications, and Their Optical Properties. *Chem. Rev.* **2019**, *119*, 3296−3348.

4. Zhang, F.; Zhong, H.; Chen, C.; Wu, X.; Hu, X.; Huang, H.; Han, J.; Zou, B.; Dong, Y. Brightly Luminescent and Color-Tunable Colloidal $CH_3NH_3PbX_3$ (X = Br, I, Cl) Quantum Dots: Potential Alternatives for Display Technology. *ACS Nano* **2015**, *9*, 4533–4542.

5. Shi, D.; Adinolfi, V.; Comin, R.; Yuan, M.; Alarousu, E.; Buin, A.; Chen, Y.; Hoogland, S.; Rothenberger, A.; Katsiev, K.; *et al.* Low Trap-State Density and Long Carrier Diffusion in Organolead Trihalide Perovskite Single Crystals. *Science* **2015**, *347*, 519–522.

6. Akkerman, Q. A.; Motti, S. G.; Kandada, A. R. S.; Mosconi, E.; D'Innocenzo, V.; Bertoni, G.; Marras, S.; Kamino, B. A.; Miranda, L.; Angelis, F. D.; *et al.* Solution Synthesis Approach to Colloidal Cesium Lead Halide Perovskite Nanoplatelets with Monolayer-Level Thickness Control. *J. Am. Chem. Soc.* **2016**, *138*, 1010−1016.

7. Ghimire, S.; Takahashi, K.; Takano, Y.; Nakamura, T.; Biju, V. Photon Recycling by Energy Transfer in Piezochemically Synthesized and Close-Packed Methylammonium Lead Halide Perovskites. *J. Phys. Chem. C* **2019**, *123*, 27752−27758.

8. Ghimire, S.; Chouhan, L.; Takano, Y.; Takahashi, K.; Nakamura, T.; Yuyama, K.; Biju, V. Amplified and Multicolor Emission from Films and Interfacial Layers of Lead Halide Perovskite Nanocrystals. *ACS Energy Lett.* **2019**, *4*, 133−141.

9. Ghimire, S.; Nair, V. C.; Muthu, C.; Yuyama, K.; Vacha, M.; Biju, V. Photoinduced Photoluminescence Enhancement in Self-Assembled Clusters of Formamidinium Lead Bromide Perovskite Nanocrystals. *Nanoscale* **2019**,*11*, 9335−9340.

10. Nair, V. C.; Muthu, C.; Rogach, A. L.; Kohara, R.; Biju, V. Channeling Exciton Migration into Electron Transfer in Formamidinium Lead Bromide Perovskite Nanocrystal/Fullerene composites. *Angew. Chem. Int. Ed.* **2017**, *56*, 1214–1218.

11. Protesescu, L.; Yakunin, S.; Bodnarchuk, M. I.; Krieg, F.; Caputo, R.; Hendon, C. H.; Yang, R. X.; Walsh, A.; Kovalenko, M. V. Nanocrystals of Cesium Lead Halide Perovskites (CsPbX3, X=Cl, Br, and I): Novel Optoelectronic Materials Showing Bright Emission with Wide Color Gamut. *Nano Lett.* **2015**, *15*, 3692-3696.

12. Liao, Q.; Hu, K.; Zhang, H.; Wang, X.; Yao, J.; Fu, H. Perovskite Microdisk Microlasers SelfAssembled from Solution. *Adv. Mater.* **2015**, *27*, 3405-3410.

13. López, R.; Gómez, R. Band-gap Energy Estimation from Diffuse Reflectance Measurements on Sol–Gel and Commercial TiO_2: A Comparative Study. *J. Sol-Gel Sci. Technol.* **2012**, *61*, 1–7.

Chapter 3

Energy Transfer in Pellets and Microcrystals of Perovskites

Abstract

Photon recycling and charge carrier migration are two important phenomena which influence photoluminescence and carrier dynamics in lead halide perovskite single crystals and films. Besides, in closely-packed perovskite structures, a nonradiative energy transfer among different crystalline domains through the distributed energy states should also be considered. However, a closely-packed donor-acceptor type structure is necessary for the efficient energy transfer process. In this chapter, I discuss the role of nonradiative energy transfer among the closely-packed crystallites of lead halide perovskites in photon recycling. For this purpose, I introduce a new piezochemical method to synthesize closely-packed pristine methylammonium lead halide and mixed bromide-iodide (heterojunction) perovskites. The efficient nonradiative transfer of excitation energy is realized in a mixed bromide-iodide (heterojunction) perovskite with distinct higher (bromide) and lower (iodide) band-gap domains. The phenomenon of nonradiative energy transfer is characterized by temporally- and spectrally-resolved photoluminescence, where the fast relaxation of photoexcited bromide-rich domain is associated with the depopulation of its excited state by the iodide-rich domain. These results suggest that energy transfer plays important roles on photon recycling among the heterogenous crystallites of perovskites. Concerning these facts, I also study the PL properties of methylammonium lead halide perovskites microcrystals by using temporally- and spectrally-resolved photoluminescence. I find that the photon recycling through repeated self-absorption and re-emission of photons play dominant role on the PL properties and charge carrier dynamics of perovskite microcrystals. In addition to the energy transfer process, the pellets and microcrystals of lead halide perovskites may also involve carrier migration. However, the fast PL decays in these samples suggest that there is no long-range migration of charge carriers, and the PL is mainly influenced by the photon recycling or the nonradiative energy transfer.

3.1 Introduction

The study of PL and charge carrier properties in lead halide perovskites can be realized by processing them using different solution-based[1-5] and solid state methods.[6-10] Close packing of perovskite crystallites may result either in the nonradiative energy transfer through the distribution of their energy states or band-gaps[11,12] or in the long-range migration of charge carriers.[5,13,14] On the other hand, thick perovskite samples show photon recycling, where the photoexcitation results in multiple cycles of self-absorption and re-emission.[15-19] In this chapter, I discuss energy transfer process and it's role on photon recycling in closely-packed lead halide perovskite crystallites by modulating the distribution of their energy states or band-gaps. To support the photon recycling process in thick perovskite samples, I also study the surface and bulk charge carrier properties of lead halide perovskite microcrystals.

Multiple photon recycling events along with photonic confinement with in the perovskite sample result in low energy PL to escape far away from the point of excitation. Therefore, the long-range energy transport is not only limited to a carrier diffusion length but can occur through repeated recycling between photons and electron-hole pairs.[20] Yamada *et al.*[15] first demonstrated the photon recycling process in $MAPbI_3$ perovskite single crystals by using time-resolved PL measurements under one- and two-photon excitation. Friend and coworkers[20] have shown an increase in the excited state population of charge carriers in bulk $MAPbI_3$ perovskite film resulting in high open circuit voltages, which is attributed to the photon recycling process. Conversely, Fang *et al.*[21] have reported very small photon recycling efficiencies (<0.5%) in $MAPbI_3$ and $MAPbBr_3$ perovskite microcrystals, underscoring the intrinsically long carrier recombination lifetime instead of the photon recycling-induced photon propagation responsible for their long carrier diffusion length. However, they did not exclude the possibility of photon recycling in polycrystalline films of perovskites. Recently, a red-shifted and delayed emission was reported in 2D lead halide perovskites which was mainly attributed to photon recycling that acted as the dominant process instead of the interplane carrier migration in such multi-quantum-well perovskite structures.[22] Therefore, photon recycling and charge carrier migration are two important phenomena that affect PL and carrier dynamics in lead halide perovskites. In addition, a nonradiative energy transfer through the distributed energy

states among different crystalline domains in closely-packed perovskite structures should also be considered. Some studies have shown energy transfer among lead halide perovskite nanocrystals of different sizes or compositions which exhibit different band-gaps in their films,[11] aggregates,[12] and colloidal solution.[23] However, a more rigorous study on the role of nonradiative energy transfer on photon recycling in closely-packed perovskite structures is yet to be carried out. The efficiency of energy transfer in such structures depend upon the close packing and the composition of the crystallites. In this regard, the methods for preparing or processing closely-packed perovskites become important.

The closely-packed perovskite structures can be realized either by processing them into films, clusters or by pressing the perovskite crystallites under the pressure. In this chapter, I study the *in-situ* solid state formation and processing of perovskite crystallites into close-packed arrangements. So far, the solid state method involves direct grinding or ball-milling of precursor salt mixtures to yield perovskite lattice.[6,7,24-26] Such method foots on a mechanochemical technique with high efficiency, remarkable reproducibility, and environmental friendliness. For instance, Jadlowski *et al.*[24] have synthesized 3D $MAPbI_3$, $FAPbI_3$, and 1- and 2D $GuaPbI_3$ perovskites by grinding the precursor salts in an electrical ball mill. Michaelis and coworkers[26] have reported the mechanochemical synthesis of 0- and 3D cesium lead mixed halide perovskites by crushing the precursor salts using a hand pestle and mortar. While the mechanical force is a major driving parameter for the solid state reaction among precursors to form the perovskite in a mechanical grinding or ball-milling process, the pressure is another important thermodynamic variable that can result in the *in-situ* formation and close packing of perovskite crystallites. For instance, silicate perovskites are abundant in the lower part of the Earth's mantle where pressure plays a vital role in the formation of these materials.[27] Although studies on the effect of pressure on the electronic and optical properties and the crystal structure of perovskites are known,[8-10] piezochemical synthesis of these materials is not reported yet. Any chemical reaction resulting from the pressure which is applied on the reactants is termed as 'piezochemistry'. In this study, I introduce piezochemical synthesis to prepare closely-packed pristine $MAPbX_3$ (X=Cl, Br, I) perovskites, where hydraulic pressure is applied for the chemical reaction.[28] The method is further extended to prepare mixed bromide-iodide ($MAPbBr_{3-x}I_x$) heterojunction perovskites.

3.2 Results and Discussion

3.2.1 Characterization of $MAPbX_3$ Perovskites

This study is the first report on the piezochemical synthesis of lead halide perovskites, where the applied pressure converts the chains of edge-sharing orthorhombic PbX_2 into corner-sharing PbX_6 octahedra.[28] I hypothesize that, under the applied pressure, such transformation is assisted by the deformation of MAX, squeezing out the halide ion to become a part of the octahedra. In parallel, MA^+ is pushed into the cavity between the octahedra to form a stable perovskite structure. Piezochemical method resulted in the formation of thick (ca. 1 mm) disc-shaped (diameter ca. 20 mm) perovskite pellets, which are shown in Figure 3.1a. This hypothesis of pressure-assisted transformation of

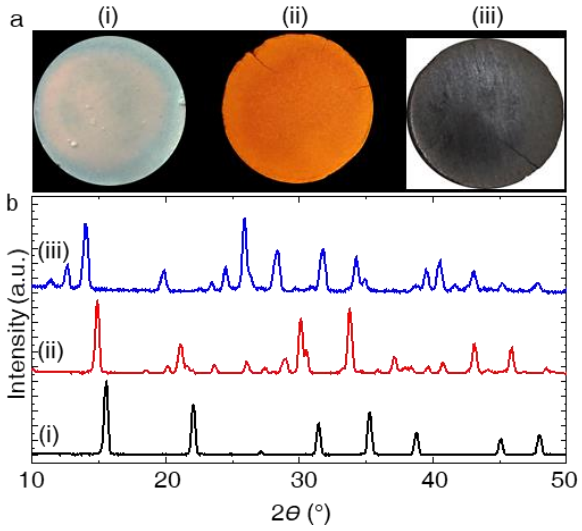

Figure 3.1 Characterization of $MAPbX_3$ (X=Cl, Br, I) perovskite pellets. (a) Photographs and (b) powder XRD patterns of (i) $MAPbCl_3$, (ii) $MAPbBr_3$, and (iii) $MAPbI_3$ perovskite samples.

precursors into perovskites is supported by the structural characterization of these samples, which is carried out by using XRD, as shown in Figure 3.1b. The XRD study reveals different crystal phases of the piezochemically synthesized perovskite samples, which are consistent with the literature reports.[29-34] The XRD pattern of $MAPbCl_3$ reveals cubic crystalline phase with the 100, 110, 111, 200, 210, 211, 220, and 300 crystal planes.[29,30] In the case of $MAPbBr_3$, a mixture of cubic and orthorhombic phases is observed. The Bragg's diffraction peaks of $MAPbBr_3$ at 14.90°, 21.18°, 30.13°, 33.83°, 37.15°, 43.14°, and 45.93° correspond to the 100, 110, 200, 210, 211, 220, and

300 crystal planes, respectively, of a cubic crystalline phase.[31,32] The existence of orthorhombic phase is confirmed by the splitting of a diffraction peak at 30.13° (the 200 crystal plane) and the appearance of a new peak at 30.56° (the 121 crystal plane).[31,33] $MAPbI_3$ perovskite shows tetragonal crystalline phase with characteristic diffraction peaks at 13.99°, 19.86°, 23.46°, 24.48°, 28.36°, 31.79°, 34.29°, 34.95°, 40.56°, and 43.08° that correspond to the 110 or 002, 112, 211, 202, 004 or 200, 114 or 222, 024, 312, 224 or 040, and 314 or 330 crystal planes, respectively.[34]

3.2.2 Optical Properties of $MAPbX_3$ Perovskites

I studied the optical properties of $MAPbX_3$ perovskite pellets using PL and Kubelka-Munk diffused reflectance spectroscopic techniques. The PL spectra of the perovskite samples are shown in Figure 3.2a. Here, $MAPbCl_3$, $MAPbBr_3$, and $MAPbI_3$ perovskite pellets show blue (ca. 450 nm), green (ca. 560 nm) and near infrared (NIR, ca. 760 nm) emission peaks, respectively. I also estimated the optical band-gaps of $MAPbX_3$ perovskites from the Tauc plots, which are shown in Figure 3.2b. The band-gap values

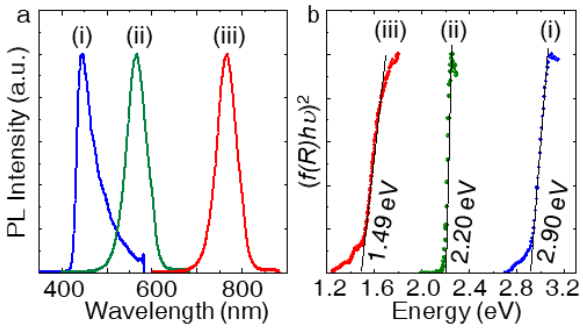

Figure 3.2 Optical properties of $MAPbX_3$ (X=Cl, Br, I) perovskites. (a) PL spectra and (b) the Tauc plots of (i) $MAPbCl_3$, (ii) $MAPbBr_3$, and (iii) $MAPbI_3$ perovskite pellets.

for $MAPbCl_3$, $MAPbBr_3$, and $MAPbI_3$ are 2.90, 2.20, and 1.49 eV, respectively.[35] Here, the red-shift in PL of perovskite samples are correlated to the decrease in band-gap in the order $E_g(MAPbCl_3) > E_g(MAPbBr_3) > E_g(MAPbI_3)$, which is due to the increase in the contribution of halogen's *p*-orbital on the VBM of a lead halide perovskite and the enhancement of SOC when the composition changes from Cl to Br and from Br to I.[35-38] In addition to the halogen-induced red-shift, the PL maxima of these pellets are further shifted to lower energy when compared to the perovskite nanocrystals.[2] Also, the emissions from the pellets have lower intensity when compared to their isolated

crystals, which is due to the increased frequency of nonradiative recombination during the multiple self-absorption and nonradiative energy transfer processes. These red-shifted and low-intensity PL bands in thick perovskite pellets are similar to the photon recycling and inner-filtering processes observed in thick films and large single crystals of perovskites.[15-20,22] Further the Tauc plots, shown in Figure 3.2b, have the low-energy tails, suggesting heterogeneity in these samples induced by the applied pressure. Based on these results, I hypothesize that the closely-packed perovskite crystallites in the pellet have a distribution of energy states or bands. On the other hand, I do not exclude the possibility of excitation light scattering by the microcrystallites in the pellet. Therefore, concerning the close packing of perovskite crystallites with the distribution of energy states in these samples, energy transfer through such energy states should play an important role on photon recycling. The energy transfer in such closely-packed perovskite samples complicates the charge carrier dynamics.

3.2.3 Photon recycling by Energy Transfer in $MAPbBr_{3-x}I_x$ Perovskites

To understand photon recycling through distributed energy states among closely-packed perovskite crystallites, I prepared $MAPbBr_{3-x}I_x$ perovskites with mixed halide composition by the piezochemical method. Based on the E_g values, I assign the bromide-rich domain as energy donor and the iodide-rich domain as energy acceptor. I

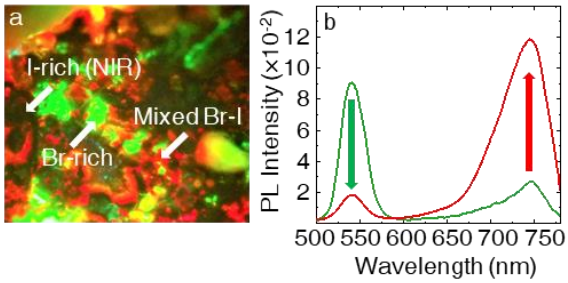

Figure 3.3 Photon recycling by nonradiative energy transfer in a $MAPbBr_{3-x}I_x$ perovskite pellet. **(**a) PL image of the $MAPbBr_{3-x}I_x$ perovskite pellet. The image size is 100 μm×100 μm. (b) PL spectra of the $MAPbBr_{3-x}I_x$ perovskite pellet collected from bromide-rich and iodide-rich domains across the heterojunction.

evaluated the energy transfer process from the donor to the acceptor domain by recording time-resolved PL at the bromide-iodide heterojunction. The microscopic PL image of a $MAPbBr_{3-x}I_x$ pellet is shown in Figure 3.3a which reveals bromide-rich

(green), iodide-rich (NIR), and mixed bromide-iodide (red) domains. Such distinct band-gap domains in a perovskite system are likely to influence photon recycling by nonradiative energy transfer. As shown in the PL spectra in Figure 3.3b, which is recorded at different positions on the mixed halide pellet, some areas showed bromide-rich intense green emission ca. 550 nm and some other areas showed iodide-rich intense NIR emission ca. 750 nm. In other words, across the bromide-iodide heterojunction, the PL from the donor becomes less and less intense which is accompanied by the more and more intense PL from the acceptor, suggesting energy transfer from bromide-rich to iodide-rich domains. Nevertheless, different ratio of bromide and iodide compositions in different areas of mixed halide pellet cannot be excluded based on the variations in PL intensities in these regions.

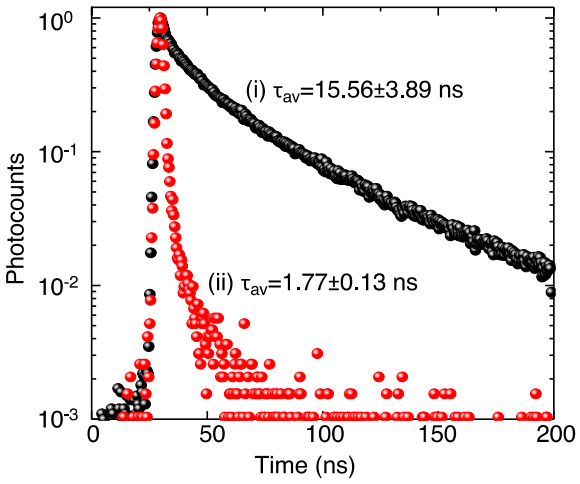

Figure 3.4 PL decay profiles of (i) a pristine $MAPbBr_3$ and (ii) bromide-rich (green emitting) domain in the $MAPbBr_{3-x}I_x$ perovskite pellet. The two decays were collected in the 500-575 nm region.

The nonradiative energy transfer from bromide- to iodide-rich domains is confirmed by comparing the PL decay of a bromide-rich domain at the heterojunction with that of pristine $MAPbBr_3$, which are shown in Figure 3.4. The efficient nonradiative energy transfer from the donor to the acceptor at the interface is obvious from the τ_{av} of a green emitting bromide-rich domain which is much shorter (ca. 1.77±0.33 ns) than that of pristine $MAPbBr_3$ pellet (ca. 15.56±3.89 ns). Photon recycling by multiple self-absorption and re-emission alone should not affect the τ_{av} of the donor, whereas energy transfer from the bromide-rich domain depopulates its excited state and thus lowers the τ_{av}. Nevertheless, the emission from the mixed

bromide-iodide domain is not clearly observed in the PL spectra (Figure 3.3b) which suggests that the mixed halide domains act as both the acceptor for the bromide-rich domain and the efficient donor for the iodide-rich domain. In other words, the mixed halide domain facilitates efficient nonradiative energy transfer from the donor to the acceptor.

From the τ_{av} values of pristine $MAPbBr_3$ perovskite pellet and the bromide-rich domain of the mixed halide perovskite, I estimated the rate of nonradiative energy transfer in the $MAPbBr_{3-x}I_x$ perovskite using equations 3.1 and 3.2 as follows:

$$\tau_0 = \frac{1}{k_{\mathrm{r}} + k_{\mathrm{nr}}} \tag{3.1}$$

$$\tau = \frac{1}{k_{\mathrm{r}} + k_{\mathrm{nr}} + k_{\mathrm{et}}} \tag{3.2},$$

where τ_0 and τ are the PL lifetimes of pristine $MAPbBr_3$ perovskite pellet and green emitting bromide-rich domain at the heterojunction, respectively; k_r and k_{nr} are the rates of radiative and nonradiative relaxations, respectively; and k_{et} is the rate of energy transfer. From τ_0 (15.56 ns) and τ (1.77 ns), the rate of energy transfer is estimated at $5x10^8$ s^{-1} which is one order of magnitude higher than the rate of carrier recombination (radiative and nonradiative) in pristine $MAPbBr_3$ perovskite ($1/\tau_0=6x10^7$ s^{-1}). Here, self-absorption of emitted photons does not add any additional path for the deactivation of the excited state in $MAPbBr_{3-x}I_x$ perovskites. Thus, a considerably decreased τ and a high k_{et} value show that nonradiative energy transfer plays a key role on photon recycling process in them. Although k_{et} in this study is discussed in terms of energy transfer, inter-domain charge carrier migration or electron transfer in such systems may also exist. I also estimated the efficiency of nonradiative energy transfer in a $MAPbBr_{3-x}I_x$ perovskite by using the equation,

$$\eta=1-\tau_{DA}/\tau_D \tag{3.3},$$

where η is the efficiency of energy transfer, τ_{DA} is the PL lifetime of donor (Br-rich domain) in the presence of acceptor (I-rich domain) and τ_D is the PL lifetime of donor in the absence of acceptor (pristine $MAPbBr_3$ pellet). For τ_{DA}=1.77 ns and τ_D=15 ns, η is 0.88, which is quite high and supports efficient nonradiative energy transfer in mixed

halide perovskites.

3.2.4 Effect of Pressure on the PL Properties and Energy Transfer

The efficiency of nonradiative energy transfer depends upon the degree of close packing among perovskite crystallites. Therefore, I prepared $MAPbBr_3$ perovskite pellets at different pressures of 1.2, 3.6, 4.8 and 6.0 GPa and compared the PL properties of these samples. The PL spectra of $MAPbBr_3$ perovskite pellets synthesized at different pressures are given in Figure 3.5. When the pressure was increased from 1.2 to 2.4 GPa, a red-shift of ca. 90 meV in the PL maximum with spectral narrowing from a full width at half maximum (FWHM) of 34 to 23 nm was detected. This red-shifting and spectral

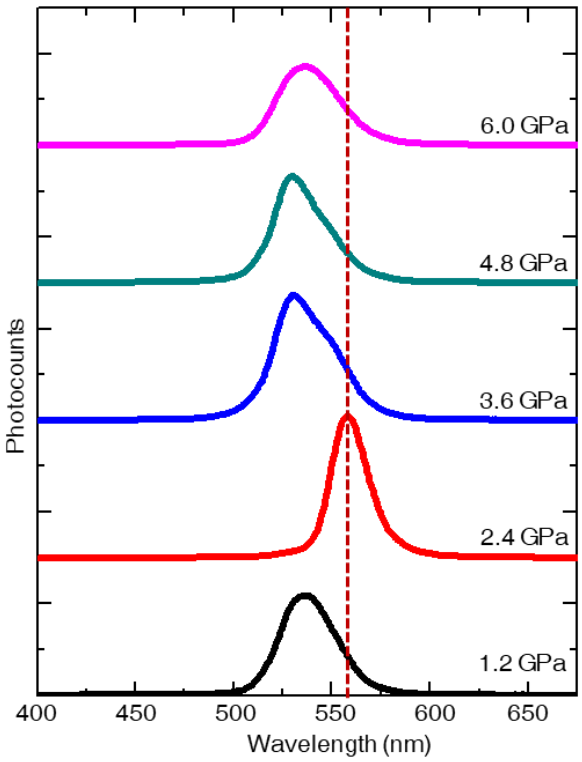

Figure 3.5 Pressure-dependent PL spectra of $MAPbBr_3$ perovskite pellets.

narrowing of PL band is ascribed to the Pb-X-Pb bond-length compression upon the increment of pressure. Further, when the pressure was increased from 2.4 to 3.6 GPa and from 3.6 to 4.8 GPa, a blue-shift of ca. 120 meV with an increase in the broadening of PL band from a FWHM of 23 nm at 2.4 GPa to 34 nm at 4.8 GPa was revealed. This is discussed in terms of octahedral tilt, which is the decrease in Pb-X-Pb bond-angle from 180° to the lower values. At 6.0 GPa, which is the maximum applied pressure in this study, I observed a further increase in the FWHM (38 nm) of the PL band. However,

the spectral broadening in this case was accompanied by a red-shift (30 meV) in the PL maximum which indicates the disordering of organic cation (MA^+) and amorphization of the perovskite lattice at a very high pressure. The variation in PL properties of perovskite pellets at different pressures is due to the enhancement and weakening of SOC which is induced by the compression of Pb-X bond and decrease of Pb-X-Pb bond-angle, respectively.[8-10] A large blue-shift (120 meV) of PL spectra in 2.4 to 4.8 GPa pressure range suggests a significant octahedral tilting of the perovskite lattice, which changes the band-gap and PL maximum through the weakening of SOC. In closely-packed perovskite structures with distributed band-gaps, the PL shift can affect the efficiency of energy transfer by influencing the spectral overlap between donor and acceptor. Thus, sample-to-sample variation in pressure can affect the energy transfer and photon recycling.

3.2.5 Mechanism of Photon Recycling by Energy Transfer

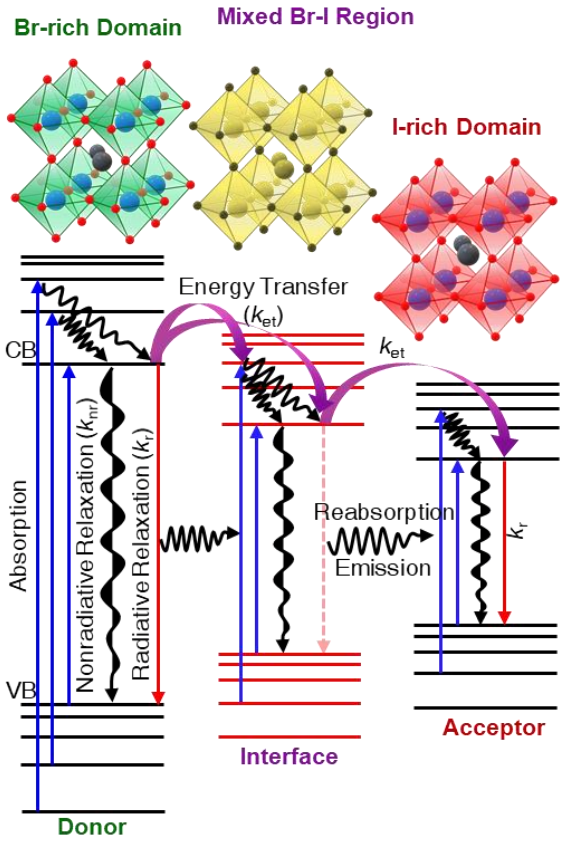

Figure 3.6 A scheme of photon recycling and energy transfer in the mixed bromide-iodide (heterojunction) perovskite.

Although multiple self-absorption and re-emission of photons are the major processes

in photon recycling, the role of nonradiative energy transfer is obvious from the above results. In this regard, in addition to the radiative processes which are involved in photon recycling, nonradiative energy transfer should also be considered alongside, which is shown schematically in Figure 3.6. In the scheme, the energy states of the bromide-rich donor and the iodide-rich acceptor are depicted to the left and right sides, respectively. The energy states formed by the mixed halide (bromide-iodide) domain at the interface whose band-gap is intermediate between the bromide- and iodide-rich domains are shown in between. Mixed halide domain acts as both the acceptor and the donor. When photoexcited, all the three perovskite domains across the heterojunction show various radiative and nonradiative processes. Besides, some of the photons emitted by donor are absorbed and emitted again by the acceptor, marking the radiative photon recycling process. However, when the nonradiative energy transfer surpass the interband relaxation, the excited state of the bromide-rich donor depopulates by efficiently transferring the energy nonradiatively to acceptors. Here, the mixed halide region helps to channel the energy efficiently from bromide- to iodide-rich domains, but without undergoing radiative relaxation, which is also discussed earlier in Figure 3.3.

3.2.6 Photon Recycling by Self-absorption in Perovskite Microcrystals

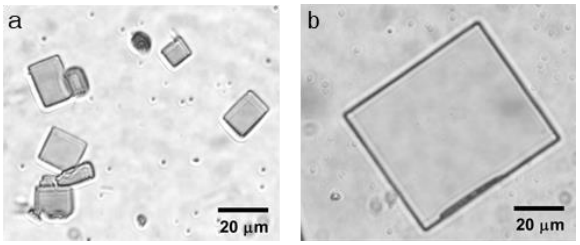

Figure 3.7 Optical microscopic images of (a) small and (b) large size $MAPbBr_3$ microcrystals synthesized by AVC method.

In thick perovskite samples, photon recycling by multiple self-absorption and re-emission leading to a delayed PL is well established.[15-20] However, in this study, the piezochemically synthesized closely-packed pellets of lead halide perovskites with considerable thickness (ca. 1 mm) show short τ_{av} values when compared to the perovskite samples involving strong photon recycling[15-20] or long-range carrier migration,[1,5,13,14,29,39,40] suggesting the role of efficient nonradiative energy transfer in photon recycling. On the other hand, the trap states and grain boundaries induced by

the heterogeneity in these samples might have also affected the PL properties and charge carrier dynamics. Concerning these facts, I studied the surface and bulk PL properties of $MAPbBr_3$ microcrystals which are prepared by the AVC method[41] and are shown in Figure 3.7a,b. These microcrystals show size distribution within few tens of micrometer range.

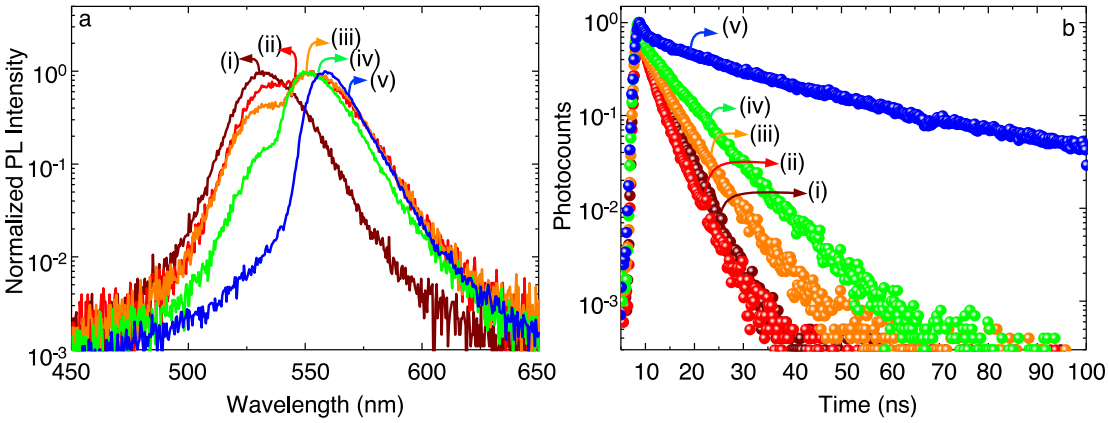

Figure 3.8 PL properties of $MAPbBr_3$ microcrystals with different size. (a) PL spectra recorded from (i) small to (v) large size $MAPbBr_3$ microcrystals showing asymmetric and red-shifted emission bands. (b) PL decay profiles corresponding to the (i-v) PL spectra shown in (a).

To study the effect of photon recycling on the PL properties of perovskite microcrystals, I recorded the PL spectra and decay profiles of these samples, which are shown in Figure 3.8a and b, respectively. As shown in Figure 3.8a, I observed asymmetric PL spectra with red-shift in emission wavelength which are recorded from the small (ca. 10 μm) to the large (ca. 80 μm) size $MAPbBr_3$ microcrystals. The PL spectra (i) from a small size microcrystal shows emission maxima ca. 530 nm, which is red-shifted to 560 nm in (v) for a large size microcrystal. On the other hand, the intermediate PL spectra (ii-iv) show emission maxima at 550 nm with a shoulder at higher energy region ca. 530 nm, which gradually decreases as the crystal size increases. Here, these PL spectra are recorded in transmission mode by exciting the microcrystals at one side and collecting the emission from another side. Therefore, the PL generated on the surface of the microcrystal has to travel across certain thickness of the crystal to reach the detector. This results in two possibilities, inner-filtering and photon recycling, for the origin of above spectral features.[15-19,22] In photon recycling, the PL generated by the carrier recombination at the excitation spot propagates inside the crystal, which is

self-absorbed and re-emitted far away from the excitation spot, resulting in reduced PL energy. The largely red-shifted (ca. 30 nm) PL spectra (v) when compared to (i) in Figure 3.8a is attributed to such photon recycling effect. On the other hand, during inner-filtering, the photons are self-absorbed inside the crystal during propagation, but they are not re-emitted. As the result, the PL at higher energy weakens while the wavelength of lower energy PL does not shift even with the increase in the propagation distance. The intermediate PL spectra (ii-iv) in Figure 3.8a suggests the dominance of inner-filtering effect in the corresponding crystals. To further support these phenomena in lead halide perovskite microcrystals, I recorded the PL decay profiles (Figure 3.8b) which correspond to (i-v) PL spectra shown in Figure 3.8a and estimated the τ_{av} values. The photon recycling process includes both the self-absorption and re-emission, in which the high energy photons are absorbed and only the low energy photons are regenerated. As the result, the τ_{av} should increase. This is indeed the case for the large $MAPbBr_3$ microcrystal with the most red-shifted PL spectra (v). The τ_{av} value is ca. 20 ns, which is longest when compared to all other microcrystals in this study. On the other hand, during the inner-filtering effect, the τ_{av} is not much affected, which is again consistent with the estimated τ_{av} values which varies in the range of 2-4 ns, as shown in Figure 3.8b, for the crystals with intermediate PL spectra (ii-iv).

Although inner-filtering and photon recycling plays important role on the PL properties of perovskite microcrystals, the involvement of carrier diffusion in these systems cannot be completely ruled out. Therefore, in order to distinguish the contribution of carrier diffusion and photon recycling on the PL lifetime of perovskite microcrystals, I recorded the temporally- and spectrally-resolved PL in the reflection mode of a large size (ca. 80 μm) microcrystal and compared the results with those obtained from the transmission mode measurements of the same crystal, as shown in Figure 3.9. Under the reflection mode, the PL spectra and the decay profiles were recorded from the same side of the microcrystal where it was excited. Therefore, the reflection and the transmission modes of PL collection help to distinguish between the surface and the bulk PL properties of the perovskite microcrystal, respectively. The PL spectra in Figure 3.8a shows that the PL under the reflection mode is broad and blue-shifted by 20 nm when compared to the PL under the transmission mode. Further, the τ_{av} at the reflection mode is very short (ca. 2 ns) when compared to that (ca. 20 ns) at the transmission mode (Figure 3.9b). These differences in the PL spectra and τ_{av} values

indicates that there must be different mechanisms controlling the PL and charge carrier dynamics on the surface and in the bulk of the crystal. The fast PL decay with emission band at higher energy recorded under the reflection mode suggests that the major contribution is from the short-range diffusion and fast recombination of photogenerated charge carriers, which is mainly influenced by the trap-states or defects.[16] In other words, the surface-related PL is least affected by the photon recycling. On the other

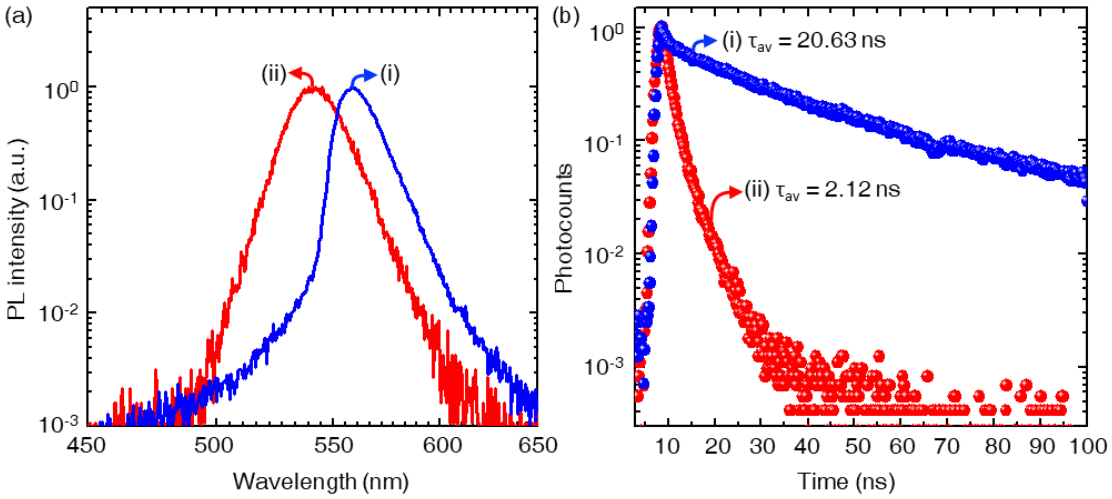

Figure 3.9 Surface and bulk PL properties of a $MAPbBr_3$ microcrystal. (a) PL spectra and (b) corresponding PL decay profiles of the $MAPbBr_3$ microcrystal measured under (i) transmission and (ii) reflection modes.

hand, the slow PL decay with emission band at lower energy recorded under the transmission mode infers that, in addition to the carrier diffusion, photon recycling also contributes to the PL properties and charge carrier dynamics of the microcrystals in their bulk.[15-19,22] Since the PL decay at the surface of the $MAPbBr_3$ microcrystals is much faster when compared to the bulk, the photon self-absorption and re-emission processes (photon recycling and inner-filtering) are dominantly influencing the PL properties in these samples rather than the long-range carrier diffusion in these samples.

3.3 Conclusions

In summary, I studied the role of photon recycling and energy transfer in the PL properties and charge carrier dynamics of closely-packed perovskite crystallites and microcrystals. I introduced piezochemical synthesis to prepare closely-packed pellets of lead halide perovskites which are ideal for studying the energy transfer processes. I

prepared pristine $MAPbX_3$ (X=Cl, Br, I) and mixed halide $MAPbBr_{3-x}I_x$ perovskite pellets by applying a hydraulic pressure to their precursors. Since the perovskite pellets are thick, and they have closely-packed crystallites, photon recycling along with the energy transfer processes must be considered to explain the PL and the carrier dynamics in such samples. In this regard, I showed photon recycling in closely-packed perovskite pellets through efficient nonradiative energy transfer. From the PL quenching of the donor (bromide-rich domain) and PL enhancement of the acceptor (iodide-rich domain) at different positions on the mixed halide perovskites, I confirmed an efficient nonradiative energy transfer in $MAPbBr_{3-x}I_x$ perovskite systems. In such mixed halide perovskites, photon recycling by self-absorption of emitted photon alone should not contribute to a fast PL relaxation of the donor. On the other hand, the results showed an extremely fast PL decay of the green emitting bromide-rich domain when compared to that of pristine $MAPbBr_3$ perovskite, suggesting the depopulation of the excited state in donor by efficient energy transfer to the acceptor across the heterojunction. In fact, not only repeated absorption and emission but also the nonradiative energy transfer among the distributed energy states contributes significantly to the photon recycling process in thick, closely-packed perovskites. On the other hand, in the case of $MAPbBr_3$ microcrystals, I observed that the photon recycling through self-absorption and re-emission of photons play dominant role on the PL properties and charge carrier dynamics. Migration of charge carrier under photoactivation in these pellets and microcrystal samples cannot be excluded. However, based on the fast PL decays in these samples when compared to the films and single crystals of perovskites reported previously,[1,5,13,14,29,39,40] one can say that there is no long-range diffusion of charge carriers. One possible reason for this is the dominance of trap states or defects in these samples. Although piezochemical synthesis is novel method for synthesizing closely-packed perovskites which are ideal for studying the energy transfer and the photon recycling processes, the limited PL and charge carrier properties of perovskites prepared by this method are not promising for their applications to energy-harvesting and lighting systems. Therefore, processing of lead halide perovskites into closely-packed structures or assemblies, but without compromising their PL properties, is necessary for their efficient applications.

References

1. Shi, D.; Adinolfi, V.; Comin, R.; Yuan, M.; Alarousu, E.; Buin, A.; Chen, Y.; Hoogland, S.; Rothenberger, A.; Katsiev, K.; Losovyj, Y.; Zhang, X.; Dowben, P. A.; Mohammed, O. F.; Sargent, E. H.; Bakr, O. M. Low Trap-State Density and Long Carrier Diffusion in OrganoLead Trihalide Perovskite Single Crystals. *Science* **2015**, *347*, 519–522.

2. Zhang, F.; Zhong, H.; Chen, C.; Wu, X.; Hu, X.; Huang, H.; Han, J.; Zou, B.; Dong, Y. Brightly Luminescent and Color-Tunable Colloidal $CH_3NH_3PbX_3$ (X = Br, I, Cl) Quantum Dots: Potential Alternatives for Display Technology. *ACS Nano* **2015**, *9*, 4533–4542.

3. Xing, G.; Mathews, N.; Lim, S. S.; Yantara, N.; Liu, X.; Sabba, D.; Grätzel, M.; Mhaisalkar, S.; Sum, T. C. Low-Temperature Solution-Processed Wavelength-Tunable Perovskites for Lasing. *Nat. Mater.* **2014**, *13*, 476–480.

4. Sadhanala, A.; Ahmad, S.; Zhao, B.; Giesbrecht, N.; Pearce, P. M.; Deschler, F.; Hoye, R. L. Z.; Gödel, K. C.; Bein, T.; Docampo, P.; Dutton, S. E.; De Volder, M. F. L.; Friend, R. H. Blue-Green Color Tunable Solution Processable Organolead Chloride–Bromide Mixed Halide Perovskites for Optoelectronic Applications. *Nano Lett.* **2015**, *15*, 6095–6101.

5. Nair, V. C.; Muthu, C.; Rogach, A. L.; Kohara, R.; Biju, V. Channeling Exciton Migration into Electron Transfer in Formamidinium Lead Bromide Perovskite Nanocrystal/Fullerene Composites. *Angew. Chem. Int. Ed.* **2017**, *56*, 1214–1218.

6. Jana, A.; Mittal, M.; Singla, A.; Sapra, S. Solvent-free, Mechanochemical Syntheses of Bulk Trihalide Perovskites and their Nanoparticles. *Chem. Comm.* **2017**, *53*, 3046–3049.

7. Prochowicz, D.; Yadav, P.; Saliba, M.; Saski, M.; Zakeeruddin, S. M.; Lewiński, J.; Grätzel, M. Mechanosynthesis of Pure Phase Mixed-Cation $MA_xFA_{1-x}PbI_3$ Hybrid Perovskites: Photovoltaic Performance and Electrochemical Properties. *Sustainable Energy Fuels* **2017**, *1*, 689–693.

8. Wang, Y.; Lü, X.; Yang, W.; Wen, T.; Yang, L.; Ren, X.; Wang, L.; Lin, Z.; Zhao, Y. Pressure-Induced Phase Transformation, Reversible Amorphization, and Anomalous Visible Light Response in Organolead Bromide Perovskite. *J. Am. Chem. Soc.* **2015**, *137*, 11144−11149.

9. Jaffe, A.; Lin, Y.; Beavers, C. M.; Voss, J.; Mao, W. L.; Karunadasa, H. I. High-Pressure Single-Crystal Structures of 3D Lead-Halide Hybrid Perovskites and Pressure Effects on their Electronic and Optical Properties. *ACS Cent. Sci.* **2016**, *2*, 201−209.

10. Cao, Y.; Qi, G.; Liu, C.; Wang, L.; Ma, Z.; Wang, K.; Du, F.; Xiao, G.; Zou, B. Pressure-Tailored Band-gap Engineering and Structure Evolution of Cubic Cesium Lead Iodide Perovskite Nanocrystals. *J. Phys. Chem. C* **2018**, *122*, 9332−9338.

11. Davis, N. J. L. K.; de la Peña, F. J.; Tabachnyk, M.; Richter, J. M.; Lamboll, R. D.; Booker, E. P.; Rivarola, F. W. R.; Griffiths, J. T.; Ducati, C.; Menke, S. M.; Deschler, F.; Greenham, N. C. Photon Reabsorption in Mixed $CsPbCl_3$:$CsPbI_3$ Perovskite Nanocrystal Films for Light-Emitting Diodes. *J. Phys. Chem. C* **2017**, *121*, 3790−3796.

12. Bouduban, M. E. F.; Burgos-Caminal, A.; Ossola, R.; Teuschera, J.; Moser, J.-E. Energy and Charge Transfer Cascade in Methylammonium Lead Bromide Perovskite Nanoparticle Aggregates. *Chem. Sci.* **2017**, *8*, 4371−4380.

13. Saba, M.; Cadelano, M.; Marongiu, D.; Chen, F.; Sarritzu, V.; Sestu, N.; Figus, C.; Aresti, M.; Piras, R.; Geddo Lehmann, A.; Cannas, C.; Musinu, A.; Quochi, F.; Mura, A.; Bongiovanni, G. Correlated Electron−Hole Plasma in Organometal Perovskites. *Nat. Commun.* **2014**, *5*, 5049.

14. deQuilettes, D. W.; Vorpahl, S. M.; Stranks, S. D.; Nagaoka, H.; Eperon, G. E.; Ziffer, M. E.; Snaith, H. J.; Ginger, D. S. Impact of Microstructure on Local Carrier Lifetime in Perovskite Solar Cells. *Science* **2015**, *348*, 683−686.

15. Yamada, Y.; Yamada, T.; Phuong, L. Q.; Maruyama, N.; Nishimura, H.; Wakamiya, A.; Murata, Y.; Kanemitsu, Y. Dynamic Optical Properties of

$CH_3NH_3PbI_3$ Single Crystals as Revealed by One- and Two-Photon Excited Photoluminescence Measurements. *J. Am. Chem. Soc.* **2015**, *137*, 10456–10459.

16. Yamada, T.; Yamada, Y.; Nishimura, H.; Nakaike, Y.; Wakamiya, A.; Murata, Y.; Kanemitsu, Y. Fast Free-Carrier Diffusion in $CH_3NH_3PbBr_3$ Single Crystals Revealed by Time-Resolved One- and Two-Photon Excitation Photoluminescence Spectroscopy. *Adv. Electron. Mater.* **2016**, *2*, 1500290.

17. Yamada, T.; Aharen, T.; Kanemitsu, Y. Near-Band-Edge Optical Responses of $CH_3NH_3PbCl_3$ Single Crystals: Photon Recycling of Excitonic Luminescence. *Phys. Rev. Lett.* **2018**, *120*, 057404.

18. Diab, H.; Arnold, C.; Ledée, F.; Trippe-Allard, G.; Delport, G.; Vilar, C.; Bretenaker, F.; Barjon, J.; Lauret, J.-S.; Deleporte, E.; Garrot, D. Impact of Reabsorption on the Emission Spectra and Recombination Dynamics of Hybrid Perovskite Single Crystals. *J. Phys. Chem. Lett.* **2017**, *8*, 2977–2983.

19. Dursun, I.; Zheng, Y.; Guo, T.; De Bastiani, M.; Turedi, B.; Sinatra, L.; Haque, M. A.; Sun, B.; Zhumekenov, A. A.; Saidaminov, M. I.; de Arquer, F. P. G.; Sargent, E. H.; Wu, T.; Gartstein, Y. N.; Bakr, O. M.; Mohammed, O. F.; Malko, A. V. Efficient Photon Recycling and Radiation Trapping in Cesium Lead Halide Perovskite Waveguides. *ACS Energy Lett.* **2018**, *3*, 1492–1498.

20. Pazos-Outón, L. M.; Szumilo, M.; Lamboll, R.; Richter, J. M.; Crespo-Quesada, M.; Abdi-Jalebi, M.; Beeson, H. J.; Vrućinić, M.; Alsari, M.; Snaith, H. J.; Ehrler, B.; Friend, R. H.; Deschler, F. Photon Recycling in Lead Iodide Perovskite Solar Cells. *Science* **2016**, *351*, 1430–1433.

21. Fang, Y.; Wei, H.; Dong, Q.; Huang, J. Quantification of Re-absorption and Re-emission Processes to Determine Photon Recycling Efficiency in Perovskite Single Crystals. *Nat. Commun.* **2017**, *8*, 14417.

22. Gan, Z.; Wen, X.; Chen, W.; Zhou, C.; Yang, S.; Cao, G.; Ghiggino, K. P.; Zhang, H.; Jia, B. The Dominant Energy Transport Pathway in Halide Perovskites: Photon Recycling or Carrier Diffusion? *Adv. Energy Mater.* **2019**, *9*, 1900185.

23. de Weerd, C.; Gomez, L.; Zhang, H.; Buma, W. J.; Nedelcu, G.; Kovalenko, M. V.; Gregorkiewicz, T. Energy Transfer between Inorganic Perovskite Nanocrystals. *J. Phys. Chem. C* **2016**, *120*, 13310−13315.

24. Jodlowski, A. D.; Yépez, A.; Luque, R.; Camocho, L.; de Miguel, G. Benign-by-Design Solventless Mechanochemical Synthesis of Three-, Two-, and One-Dimensional Hybrid Perovskites. *Angew. Chem. Int. Ed.* **2016**, *55*, 14972−14977.

25. Askar, A. M.; Karmakar, A.; Bernard, G. M.; Ha, M.; Terskikh, V. V.; Wiltshire, B. D.; Patel, S.; Fleet, J.; Shankar, K.; Michaelis, V. K. Composition-Tunable Formamidinium Lead Mixed Halide Perovskites via Solvent-Free Mechanochemical Synthesis: Decoding the Pb Environments Using Solid-State NMR Spectroscopy. *J. Phys. Chem. Lett.* **2018**, *9*, 2671−2677.

26. Karmakar, A.; Dodd, M. S.; Zhang, X.; Oakley, M. S.; Klobukowskia, M.; Michaelis, V. K. Mechanochemical Synthesis of 0D and 3D Cesium Lead Mixed Halide Perovskites. *Chem. Commun.* **2019**, *55*, 5079−5082.

27. Hirose, K.; Sinmyo, R.; Hernlund, J. Perovskite in Earth's Deep Interior. *Science* **2017**, *358*, 734−738.

28. Ghimire, S.; Takahashi, K.; Takano, Y.; Nakamura, T.; Biju, V. Photon Recycling by Energy Transfer in Piezochemically Synthesized and Close-Packed Methylammonium Lead Halide Perovskites. *J. Phys. Chem. C* **2019**, *123*, 27752−27758.

29. Maculan, G.; Sheikh, A. D.; Abdelhady, A. L.; Saidaminov, M. I.; Haque, M. A.; Murali, B.; Alarousu, E.; Mohammed, O. F.; Wu, T.; Bakr, O. M. $CH_3NH_3PbCl_3$ Single Crystals: Inverse Temperature Crystallization and Visible-Blind UV-Photodetector. *J. Phys. Chem. Lett.* **2015**, *6*, 3781−3786.

30. Baikie, T.; Barrow, N. S.; Fang, Y.; Keenan, P. J.; Slater, P. R.; Piltz, R. O.; Gutmann, M.; Mhaisalkar, S. G.; White, T. J. A Combined Single Crystal Neutron/X-Ray Diffraction and Solid-State Nuclear Magnetic Resonance Study of the Hybrid Perovskites $CH_3NH_3PbX_3$ (X = I, Br and Cl). *J. Mater. Chem. A* **2015**, *3*, 9298−9307.

31. Yang, M.; Peng, H.-S.; Zeng, F.-L.; Teng, F.; Qu, Z.; Yang, D.; Wang, Y.-Q.; Chen, G.-X.; Wang, D.-W. In Situ Silica Coating-Directed Synthesis of Orthorhombic Methylammonium Lead Bromide Perovskite Quantum Dots with High Stability. *J. Colloid Interface Sci.* **2018**, *509*, 32–38.

32. Wang, K.-H.; Li, L.-C.; Shellaiah, M.; Sun, K. W. Structural and Photophysical Properties of Methylammonium Lead Tribromide ($MAPbBr_3$) Single Crystals. *Sci. Rep.* **2017**, *7*, 13643.

33. Galkowski, K.; Mitioglu, A.; Miyata, A.; Plochocka, P.; Portugall, O.; Eperon, G. E.; Wang, J. T.-W.; Stergiopoulos, T.; Stranks, S. D.; Snaith, H. J.; Nicholas, R. J. Determination of the Exciton Binding Energy and Effective Masses for Methylammonium and Formamidinium Lead Tri-Halide Perovskite Semiconductors. *Energy Environ. Sci.* **2016**, *9*, 962–970.

34. Chin, X.Y.; Cortecchia, D.; Yin, J.; Bruno, A.; Soci, C. Lead Iodide Perovskite Light-Emitting Field-Effect Transistor. *Nat. Commun.* **2015**, *6*, 7383.

35. Manser, J. S.; Christians, J. A.; Kamat, P. V. Intriguing Optoelectronic Properties of Metal Halide Perovskites. *Chem. Rev.* **2016**, *116*, 12956–13008.

36. Tanaka, K.; Takahashi, T.; Ban, T.; Kondo, T.; Uchida, K.; Miura, N. Comparative Study on the Excitons in Lead-Halide-Based Perovskite-Type Crystals $CH_3NH_3PbBr_3$ $CH_3NH_3PbI_3$. *Solid State Commun.* **2003**, *127*, 619–623.

37. Even, J.; Pedesseau, L.; Jancu, J.-M.; Katan, C. Importance of Spin–Orbit Coupling in Hybrid Organic/Inorganic Perovskites for Photovoltaic Applications. *J. Phys. Chem. Lett.* **2013**, *4*, 2999–3005.

38. Even, J.; Pedesseau, L.; Katan, C. Analysis of Multivalley and Multibandgap Absorption and Enhancement of Free Carriers Related to Exciton Screening in Hybrid Perovskites. *J. Phys. Chem. C* **2014**, *118*, 11566–11572.

39. Dong, Q.; Fang, Y.; Shao, Y.; Mulligan, P.; Qiu, J.; Cao, L.; Huang, J. Electron-Hole Diffusion Lengths > 175 μm in Solution-Grown $CH_3NH_3PbI_3$ Single Crystals. *Science* **2015**, *347*, 967–970.

40. Bi, Y.; Hutter, E. M.; Fang, Y.; Dong, Q.; Huang, J.; Savenije, T. J. Charge Carrier Lifetimes Exceeding 15 μs in Methylammonium Lead Iodide Single Crystals. *J. Phys. Chem. Lett.* **2016**, *7*, 923–928.

41. Ghimire, S.; Chouhan, L.; Takano, Y.; Takahashi, K.; Nakamura, T.; Yuyama, K.; Biju, V. Amplified and Multicolor Emission from Films and Interfacial Layers of Lead Halide Perovskite Nanocrystals. *ACS Energy Lett.* **2019**, *4*, 133–141.

Chapter 4

Charge Carrier Dynamics in Self-assembled Perovskite Nanocrystal Clusters and Films

Abstract

The stabilization of photogenerated charge carriers in lead halide perovskites is fundamental for their utilization in energy-harvesting and lighting-emitting applications. In this chapter, I discuss the charge carrier dynamics in perovskite nanocrystals as the function of excitation intensity. In these samples, the nanocrystals are self-assembled into closely-packed structures. In the clusters and films of formamidinium and methylammonium lead bromide perovskite nanocrystals, I detect unusually delayed (>1 microsecond) recombination of charge carriers at low-intensity excitation, which becomes extremely fast (<<100 nanoseconds) and associates with amplified emission at high-intensity excitation. The prolonged photoluminescence lifetime at low-intensity excitation is attributed to the generation and diffusion of low-density charge carriers through interparticle states formed among close-packed perovskite nanocrystals. On the other hand, high-intensity excitation results in the generation of high-density and spatially confined charge carriers among close-packed perovskite nanocrystals, which recombine radiatively resulting in the fast and amplified photoluminescence. I precisely detect the photoluminescence from an irradiated area or outside and reveal the migration as well as confinement of photogenerated charge carriers in such perovskite nanocrystal self-assemblies. While the stabilization of charge carriers is promising for the efficient harvesting of charge carriers in solar cells, the generation and radiative recombination of multiple charge carriers suggest the potential application of perovskite nanocrystal assemblies in luminescent displays.

4.1 Introduction

Lead halide perovskites have emerged into promising light-harvesting and light-emitting materials, which is owing to the high charge carrier mobility and high PLQY of these materials.[1-7] The photovoltaic and optoelectronic applications of lead halide perovskites are influenced by the carrier recombination dynamics in these materials. The interplay of bound excitonic and free charge carrier states largely determines the carrier recombination dynamics in lead halide perovskites.[8-14] While charge carriers in individual PNCs, owing to the formation of bound excitons (or electron-hole pairs), follow fast radiative recombination,[12,15-19] this process is unusually delayed in large single crystals and bulk films due to the presence of free charge carriers.[2,9,20-25] The delayed radiative recombination in lead halide perovskites is associated with the long diffusion lengths of free charge carriers, which are the consequence of dissociation of photogenerated excitons due to the small exciton binding energy. Therefore, the dynamics of photogenerated charge carriers can be different among the individual PNCs and their closely-packed assemblies. In this chapter, I study the charge carrier dynamics in closely-packed assembly of organic-inorganic hybrid and all-inorganic lead halide PNCs.[26,27]

The long-range migration of charge carriers in perovskite single crystals[20-22,24,25] has attracted much attention to the carrier dynamics in films of lead halide perovskites.[2,3,9-11,23] For instance, delayed emission was observed in the thin films of polycrystalline $MAPbI_3$ perovskite by Ginger and coworkers.[2] Similarly, Noel *et al.* have discussed high carrier mobility in highly-crystalline $MAPbBr_3$ perovskite films, and developed high-voltage solar cells using such materials.[3] Saba *et al.* have shown that, in bulk films of $MAPbI_3$ and mixed halide ($MAPbI_{3-x}Cl_x$) perovskites, photoexcitation populates Coulomb-correlated, free charge carriers with negligible bound excitons.[9] The migration of photogenerated charge carriers are observed in the films of PNCs as well.[13,28,29] Previously, Kamat and coworkers detected ultrafast charge carrier migration to the iodide-rich domains in a film of mixed halide perovskite formed by the layer-by-layer deposition of $CsPbI_3$ on $CsPbBr_3$ PNC film.[28] Similarly, Pérez-Prieto and coworkers have shown that, in $MAPbBr_3$ PNC films, the photogenerated charge carriers or excitons migrate among nanocrystals, and during the migration, they collect into deep trap-states resulting in delayed emission.[13] Here, the

diffusion of charge carriers, which are generated and confined within the individual photoexcited PNCs, is possible only when these nanocrystals are assembled into closely-packed structures, which is an interesting subject to explore. However, in chapter 3, I have shown that even when the perovskite crystallites are closely-packed by applying a pressure, long-range diffusion of charge carriers is not detected. Instead, such samples show efficient nonradiative energy transfer through the distributed energy states. These results suggest that the long-range migration of charge carriers is a special case, where only the close packing of perovskite crystallites with distributed band-gaps is insufficient for such diffusion. Indeed, the quality of the perovskite crystallites and their assembly matters. Therefore, it is interesting to study the charge carrier dynamics in a perovskite system by systematically arranging the high-quality individual crystallites into closely-packed structures. The low binding energy of excitons and the long-range diffusion of charge carriers in large single crystals of perovskites attracted me to assemble PNCs into closely-packed films and clusters and study the PL properties and charge carrier dynamics in PNC assemblies.

The surface of PNCs is stabilized by hydrophobic ligands, which are long-chain organic acid (for example, oleic acid) and long-chain organic amine (for example, oleyl amine). Using these ligands, size-controlled PNCs are synthesized by LARP[4,29,16] and hot-injection methods.[15,31] These ligands not only control the size of the PNCs by surface capping but also help to disperse the nanocrystals in solutions through the repulsive interaction of their bulky hydrophobic carbon chain. However, the hydrophobic interaction between ligands can facilitate the assembly formation among nanocrystals on a substrate.[29,30] In this study, I used combinations of oleic acid and hexadecyl amine or octylammonium bromide as hydrophobic ligands to synthesize the nanocrystals of $MAPbBr_3$ and $FAPbBr_3$ perovskites by LARP[4,29] and $CsPbBr_3$ perovskite by hot-injection methods.[31] The PNCs in the colloidal solution or at the single particle level were stabilized by these capping ligands. On the other hand, in films or clusters, the capping ligands assisted PNCs to self-assemble into closely-packed structures.

4.2 Results and Discussion

4.2.1 Characterization of Perovskite Nanocrystals

I characterized the synthesized PNCs by using TEM, XRD and UV-Vis absorption and PL spectroscopy. Figure 4.1(a-c) shows the TEM images of $MAPbBr_3$, $FAPbBr_3$ and $CsPbBr_3$ PNCs. TEM image of $FAPbBr_3$ PNCs reveals spherical morphology (Figure 4.1b), whereas $MAPbBr_3$ and $CsPbBr_3$ appear cubic (Figure 4.1a,c). The morphological differences among PNCs suggests the role of ligands in controlling the shape of the nanocrystals. Here, *n*-octylamine hydrobromide was the ligand for $FAPbBr_3$ PNCs, whereas hexadecylamine was used in the case of $MAPbBr_3$ and $CsPbBr_3$ PNCs.

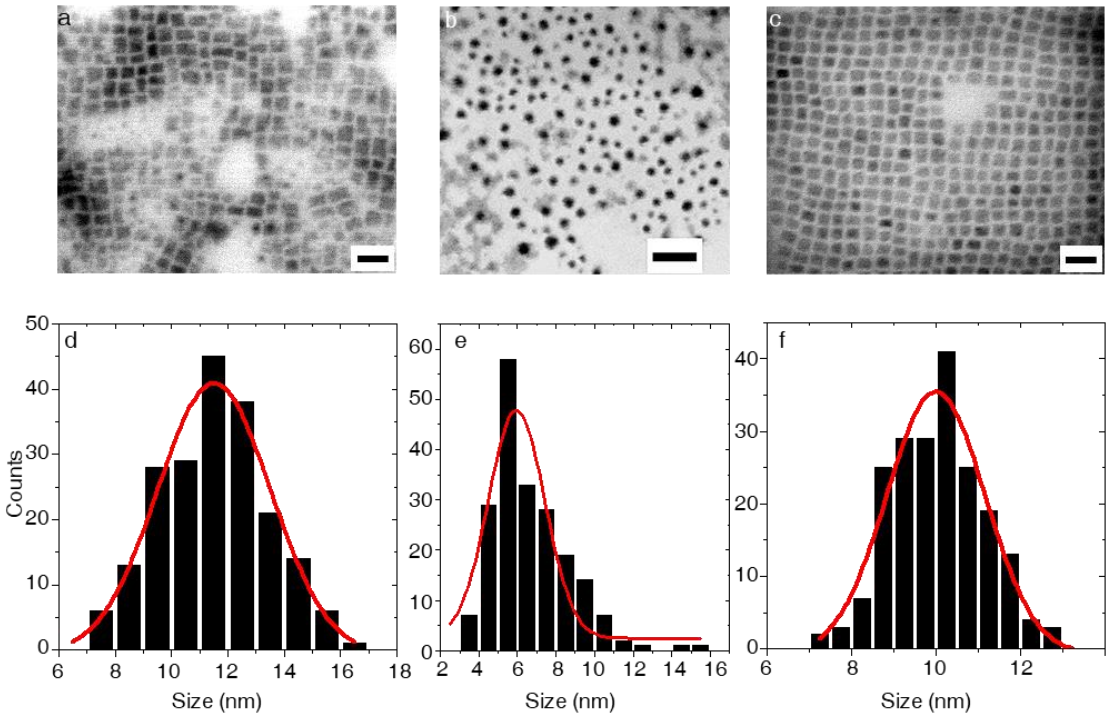

Figure 4.1 (a-c) TEM images of (a) $MAPbBr_3$, (b) $FAPbBr_3$, and (c) $CsPbBr_3$ PNCs. Scale bars correspond to 20 nm. (d-f) Size distributions of (d) $MAPbBr_3$, (e) $FAPbBr_3$, and (e) $CsPbBr_3$ PNCs.

Similarly, the TEM images reveal uniform size distribution of these nanocrystals. I analyzed the TEM images using imageJ software and estimated the apparently uniform size distribution of PNCs, which is 11.5 nm for $MAPbBr_3$, 6 nm for $FAPbBr_3$, and 10 nm for $CsPbBr_3$ PNCs. The size distribution histograms of PNCs are shown in Figure 4.1(d-f).

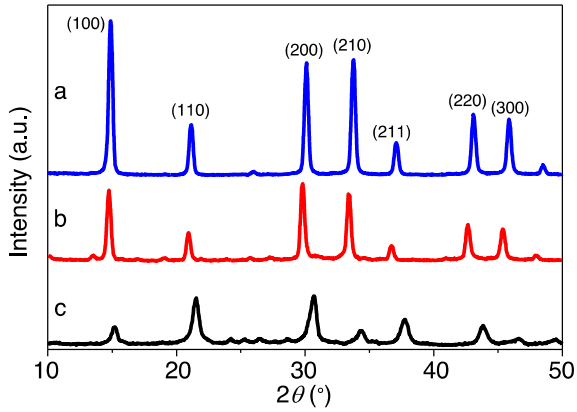

Figure 4.2 Powder XRD patterns of (a) $MAPbBr_3$, (b) $FAPbBr_3$ and (c) $CsPbBr_3$ PNCs.

The crystal structures of PNCs were characterized by powder XRD studies. Figure 4.2 shows the XRD patterns of PNCs. Based on the literature,[21,32,33] I assigned the XRD patterns of all three types of PNCs to the 100, 110, 200, 210, 211, 220, and 300 crystal planes of a cubic unit cell with *Pm*3*m* space group. The Bragg's diffraction peaks in Figure 4.2 show small shift to higher 2θ values from $FAPbBr_3$ to $MAPbBr_3$ and to $CsPbBr_3$, which is attributed to the difference in lattice parameters among different PNC samples induced by the decreasing size of A-site cations in the order: $FA^+ > MA^+ > Cs^+$.

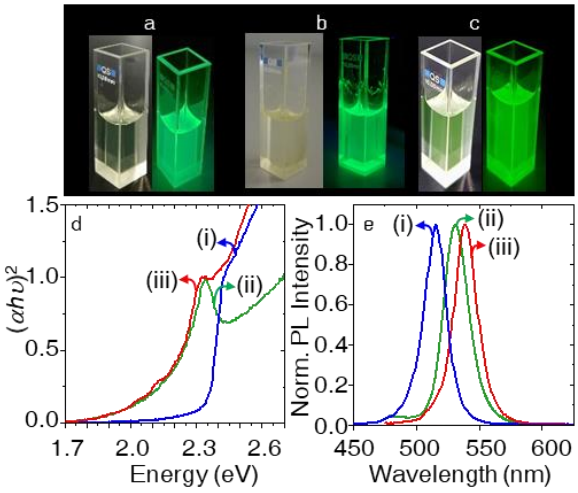

Figure 4.3 Optical characterization of PNC samples. (a-c) Photographs of (a) $CsPbBr_3$, (b) $MAPbBr_3$, and (c) $FAPbBr_3$ PNC solutions at (left) room light and (right) UV light. (d) Tauc plots and (e) PL spectra of (i) $CsPbBr_3$, (ii) $MAPbBr_3$, and (iii) $FAPbBr_3$ PNC solutions. The PL spectra were collected by exciting the samples at 400 nm wavelength.

The optical characterization of the PNCs is carried out by UV-Vis absorption and steady-state PL measurements. As shown in Figure 4.3(a-c), the colloidal solutions of

Cs-, MA-, and FA-based lead bromide PNCs show green emission under 365 nm UV light. The characteristic emission peaks are estimated ca. 540 nm for $FAPbBr_3$, 532 nm for $MAPbBr_3$, and 516 nm for $CsPbBr_3$ PNCs from the PL spectra, which are shown in Figure 4.3e. Here, the blueshift in PL spectra from $FAPbBr_3$ to $MAPbBr_3$ and to $CsPbBr_3$ is associated with the increase in E_g value in the order, $FAPbBr_3$ (2.18 eV) < $MAPbBr_3$ (2.22 eV) < $CsPbBr_3$ (2.36 eV). The band-gaps in PNC samples are estimated from the Tauc plots shown in Figure 4.3d, which is derived from the UV-Vis absorption spectra. This variation in optical properties of PNCs is correlated with the size of different A-site cations, rendering different band-gap values. It has been shown that upon the replacement of a large A-site cation (FA^+) with the smaller cation (Cs^+), octahedral tilt occurs due to the decrease of Pb-X-Pb dihedral angle.[34-36] Such a tilt in PbX_6 octahedra weakens the SOC by lowering the orbital overlap between Pb and X. The decrease in SOC increases the band-gap and shifts the PL band to blue. Furthermore, the optical properties of lead halide perovskites are also influenced by the hydrogen bonding between MA^+ or FA^+ ion and PbX_6 octahedra.[34] It has been reported that FA^+ ion has greater extent of hydrogen bonding with PbX_6 octahedra than MA^+ ion, whereas such hydrogen bonding is absent in the case of Cs^+ ion.[34] The enhanced hydrogen bonding in the case of FA^+ ion increases the ionic character of Pb-X bond, which strengthens the SOC and decreases the band-gap in $FAPbBr_3$ perovskites when compared to their MA or Cs counterparts. Such tunable optical properties of PNCs can be utilized in the optoelectronic applications of these materials. In this regard, the photostability of PNCs is necessary for their efficient use as light-emitting and light-harvesting materials.

4.2.2 Photostability of Perovskite Nanocrystals

The PNCs were photostable in solution at the ensemble level. In order to clearly understand the photostability of PNCs at their single particle level, I recorded and analyzed temporally- and spectrally-resolved photons emitted by the same single PNC at different excitation intensities or the excitation pulse energies. The time-traced total number of photons emitted by single $FAPbBr_3$ PNCs which were periodically excited by regulating the laser ON and OFF periods at 1.75, 3.5 and 5.25 mJ cm^{-2} excitations are shown in Figure 4.4a. Interestingly, the number of photons emitted by each single PNC has increased linearly with increase in the energy of excitation pulse, and the PL

intensity is apparently same over time for a particular energy of excitation pulse. The PL intensity histograms of more than 500 single $FAPbBr_3$ PNCs and the PL image of corresponding single PNCs are shown respectively in Figure 4.4b and its inset. Here, a 3-fold increase in the number of emitted photons validates the radiative process as the major process of charge carrier relaxation in a single PNC at high-intensity excitations. Similarly, this increase in the number of photons along with the apparently constant PL

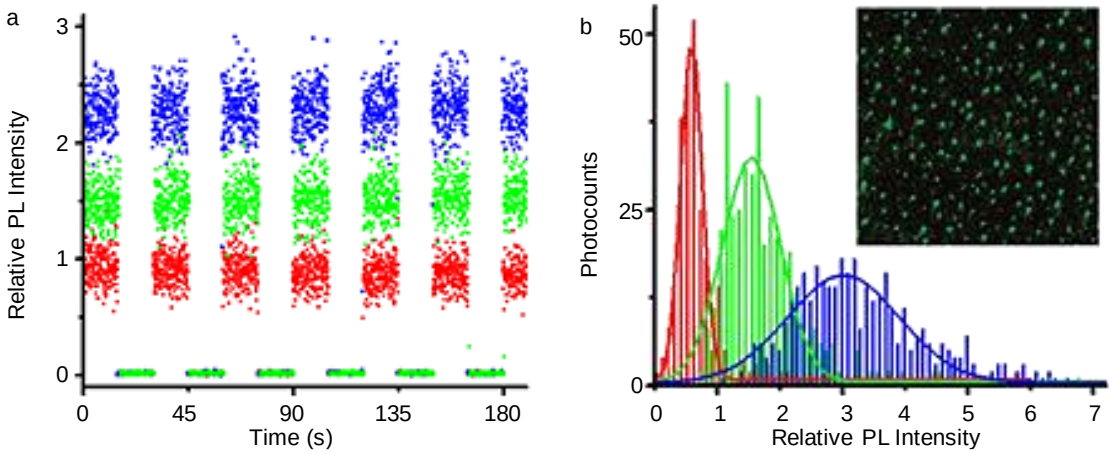

Figure 4.4 Photostability of $FAPbBr_3$ PNCs at single-particle level. (a) PL intensity trajectories and (b) PL intensity histograms of single $FAPbBr_3$ PNCs photoactivated with different laser intensities: 1.75 (red), 3.5 (green), and 5.25 (blue) mJ cm^{-2}. Inset in (b): PL image (100×100 μm^2) of single $FAPbBr_3$ PNCs. The samples were excited by using a 400 nm femtosecond laser.

intensity over time for a particular intensity of excitation suggests the photostability of single PNCs. Nevertheless, radiative bi-exciton recombination cannot be ruled out in these PNCs.[19,37,38] The excellent photostability and high rate of radiative recombination in PNCs at their single-particle level observed in this study are highly desirable not only for their photovoltaic and light-emitting applications but also for the PL and carrier dynamic studies of these nanocrystals, which are fundamental for understanding how efficiently these materials can be utilized for their diverse applications.

4.2.3 Charge Carrier Dynamics in Isolated Perovskite Nanocrystals

To understand charge carrier dynamics in PNCs, I studied the time-resolved PL properties of these nanocrystals in the colloidal solution and at the single-particle level. As shown in Figure 4.5a, PNCs in solution show fast PL decay, where the τ_{av} value

decreases in the order: $FAPbBr_3$ (14 ns) > $MAPbBr_3$ (8 ns) > $CsPbBr_3$ (6 ns). This variation in τ_{av} values is also correlated with the size of A-site cations – FA^+, MA^+, and Cs^+ – present in PNCs.[34-36] The τ_{av} was further decreased when PNCs were isolated as single particles. Here, an isolated $FAPbBr_3$ PNC at the single-particle level shows comparatively fast PL decay within 7 ns with a sharp emission ca. 545 nm (Figure 4.5b).

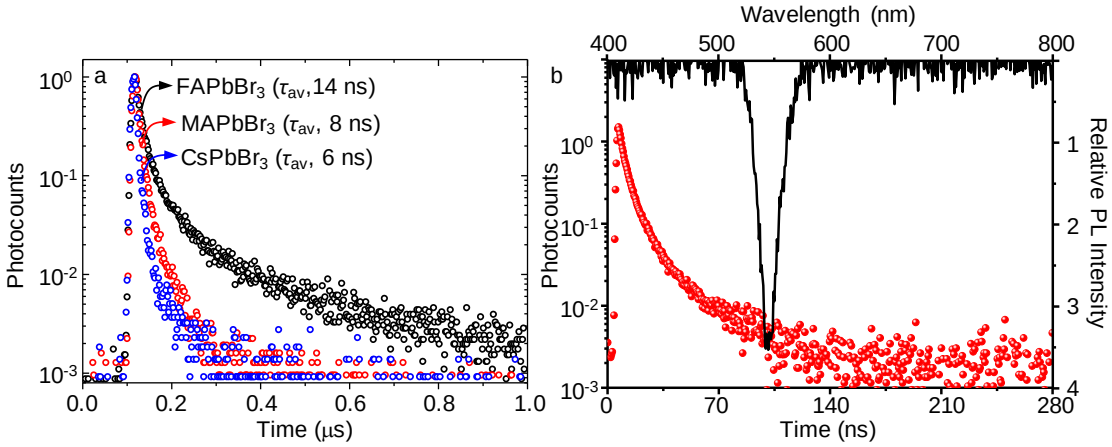

Figure 4.5 Time-resolved PL properties of PNCs in the colloidal solution and at the single particle level. (a) PL decay profiles of colloidal PNCs. (b) PL spectra (black) and the PL decay profile (red) of PNCs at the single particle level. In (a), the samples were excited by using a 400 nm femtosecond laser, and in (b), the sample was excited by using a 465 nm picosecond laser.

The difference in τ_{av} values and emission wavelengths of PNCs in solution and at the single-particle level is attributed to the ensemble averaging among the large number of isolated PNCs in the solution. Here, the fast carrier recombination in PNCs suggests the confinement of photogenerated electrons and holes within the individual nanocrystals. Nevertheless, the charge carrier properties of PNCs are modified when they are arranged in closely-packed assembly.[13,28,29]

4.2.4 Charge Carrier Dynamics in the Clusters and Films of Perovskite Nanocrystals

Guided by the long-range diffusion of charge carriers in large single crystals and films of perovskites,[2,9,20-25] I assembled the PNCs into closely-packed clusters and films and studied the time-resolved PL properties of these samples. Here, the PNC clusters were collected as precipitates, and these samples were difficult to disperse in the solvents

like toluene or hexane. The colloidal or the single-particle studies were carried out by sonicating the PNC precipitates for a long time (ca. 30–45 min) and removing the larger clusters by centrifugation or decantation. This suggests a strong interaction among the individual nanocrystals in clusters, which is mediated by the capping ligands. To understand the carrier dynamics in such clusters of strongly interacting particles, I studied the time-resolved PL properties of $FAPbBr_3$ PNC clusters under different excitation intensity, which is in the sequence: 0.044, 0.088, 0.440, 0.880, 4.40, 8.80, 17.50, 43.75, and 88 mJ cm^{-2}. The PL decay profiles of PNC clusters under the

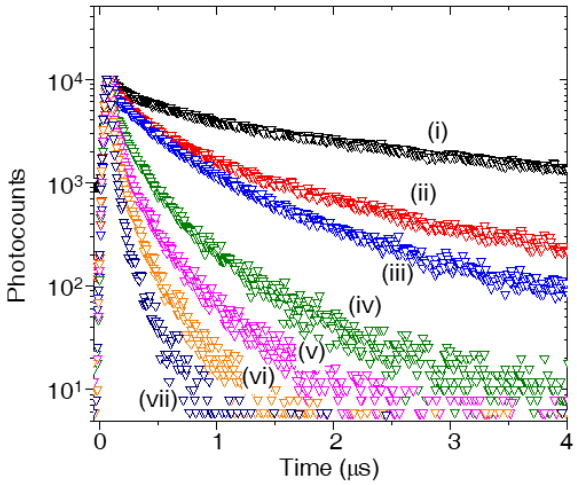

Figure 4.6 PL decay profiles of $FAPbBr_3$ PNC clusters under increasing intensity of 400 nm femtosecond excitation laser: (i) 0.044, (ii) 0.440, (iii) 0.880, (iv) 4.40, (v) 8.80, (vi) 17.50, and (vii) 88 mJ cm^{-2}.

increasing excitation intensity are shown in Figure 4.6. At the lowest intensity of excitation, the τ_{av} value of $FAPbBr_3$ PNC clusters was 800 ns, which is exceptionally long when compared with that of an isolated single PNC or the PNCs in solution. On the other hand, by increasing the intensity of excitation from 0.044 to 88 mJ cm^{-2}, the τ_{av} value of the clusters decreased systematically from 800 to 40 ns. The exceptionally long τ_{av} in PNC clusters at low-intensity excitation suggests the long-range migration of photogenerated charge carriers among strongly-interacting and closely-packed nanocrystals.

To account for the faster PL decay at high-intensity excitation, I studied the variation in number of emitted photons and τ_{av} values of PNCs in the clusters as the function of excitation laser intensity, which is shown in Figure 4.7. Here, the decrease

in τ_{av} values with the increase in the intensity of excitation laser is associated with a nonlinear increase in the number of emitted photons by the PNC clusters. On the one hand this correlation study points towards the possibility of photoinduced curing of defects with an increase in the PLQY, but on the other hand it also suggests the increase in the rate of carrier-carrier interaction and radiative recombination at high concentrations of charge carriers generated among nanocrystals at high-intensity excitation. Although the photoinduced defect curing and PLQY increase are reported in microcrystals of lead halide perovskites,[39,40] this process alone cannot account for an enormous enhancement of PL in PNCs, which was by a factor of 10^3 in these PNC clusters, when the excitation laser intensity was modulated from low to high. Further,

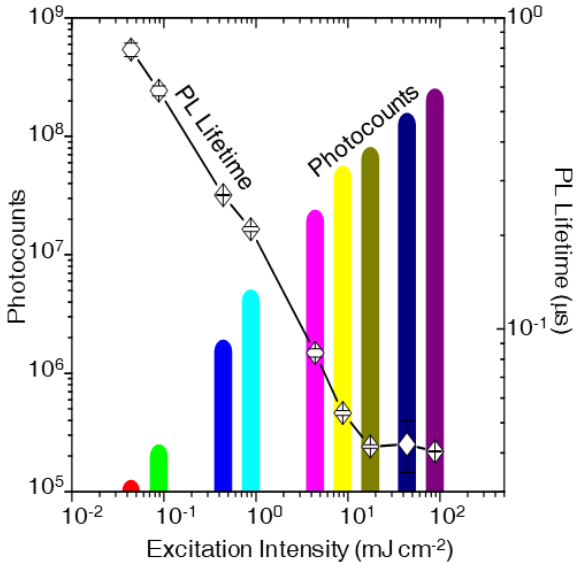

Figure 4.7 Correlation between emitted photons and τ_{av} values of $FAPbBr_3$ PNC clusters as the function of excitation laser intensity.

it is known that the defects in lead halide perovskites are shallow, and they do not contribute significantly to the trap-assisted nonradiative recombination of charge carriers.[7,21,22,24,25,41] Therefore, the observed carrier dynamics at different excitation intensities in PNC clusters is interpreted as follows. At low-intensity excitation, the density of charge carriers photogenerated among closely-packed PNCs in the clusters is low. As the result, charge carriers find larger space to diffuse, leading to delayed recombination or long τ_{av}. At the high-intensity excitation, the number of photogenerated charge carriers in PNC clusters increases and confines within a small area. Therefore, the probability of radiative charge carrier recombination dominates over their migration which shortens the τ_{av} of PNCs in the clusters. However, in highly-

excited chalcogenide quantum dots, photogenerated charge carriers are largely deactivated by the nonradiative Auger recombination which significantly shortens the τ_{av} and lowers the number of emitted photons.[42-47] In the PNC clusters, although Auger and bi-exciton recombination cannot be ruled out, an increase in the rate of radiative carrier recombination dominates the nonradiative processes, which is by the generation of multiple charges among many interacting PNCs.

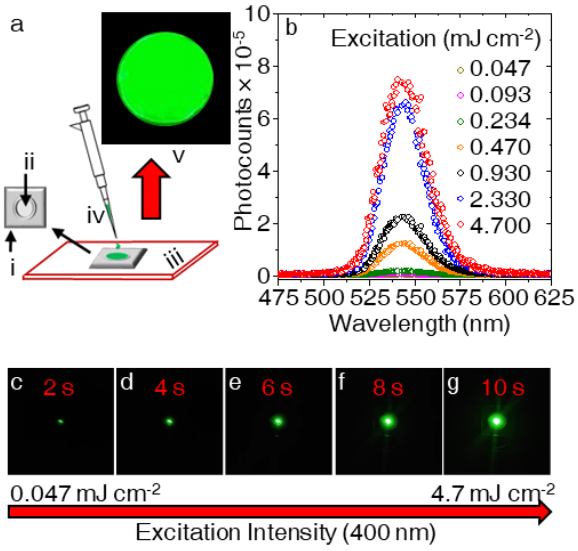

Figure 4.8 Amplified emission from a PNC film. (a) Scheme of PNC film deposition on a glass coverslip: (i) silicon rubber, (ii) sample well, (iii) glass coverslip, (iv) PNC solution, and (v) photograph of the deposited film of $MAPbBr_3$ PNCs under UV light. (b) PL spectra of $MAPbBr_3$ PNC film recorded at different excitation laser intensity. (c-g) Photographs of a $MAPbBr_3$ PNC film showing amplified emission with an increase in the intensity of excitation laser.

The remarkably delayed PL shown by the PNC clusters when compared to their colloidal solutions or isolated single nanocrystals motivated me to arrange PNCs systematically into a closely-packed film and study the carrier dynamics further.[27] Figure 4.8a shows the preparation of film sample by the deposition of PNC solutions on a glass coverslip. Here, the PNCs self-assembles into a thin film, which is facilitated by hydrophobic interactions among ligands. The films of PNCs deposited on the glass coverslips were studied by exciting the samples at systematically increased intensity of excitation light in the 0.0024 to 24 mJ cm^{-2} range with a 400 nm femtosecond laser. As shown in Figure 4.8(c-g), an enormous increase in the intensity of green emission from the film is observed. The corresponding excitation intensity-dependent PL spectra are

shown in Figures 4.8b. Such an increase in PL intensity indicates amplified emission via increase in the concentration and rate of radiative recombination of photogenerated charge carriers.

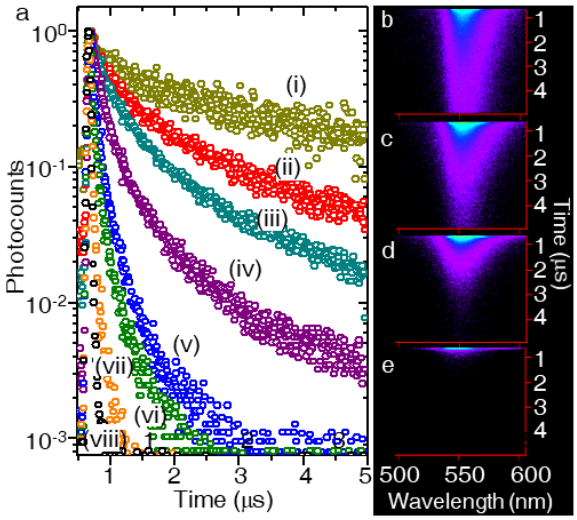

Figure 4.9 Excitation laser intensity-dependent, time-resolved PL properties of PNC films. (a) PL decay profiles of a $MAPbBr_3$ PNC film under increasing intensity of excitation laser: (i) 0.0024, (ii) 0.024, (iii) 0.047, (iv) 0.240, (v) 0.930, (vi) 2.40, (vii) 9.30, and (viii) 24.00 mJ cm^{-2}. (b-e) Temporally- and spectrally-resolved photocount maps of a $FAPbBr_3$ PNC film, with increase in intensity of excitation laser: (c) 0.024, (d) 0.24, (e) 2.40 and (f) 24.00 mJ cm^{-2}.

The charge carrier dynamics in these closely-packed PNC films are studied by estimating the τ_{av} values of the samples at different excitation intensities. The PL decay profiles of a $MAPbBr_3$ PNC film under the increasing intensity of excitation are shown in Figure 4.9a and the corresponding temporally- and spectrally-resolved photocount maps are shown in Figure 4.9(b-e). A remarkably delayed (1.86 μs for $FAPbBr_3$, and 915 ns for $MAPbBr_3$) recombination of a low density of charge carriers generated at low-intensity excitation is observed.[27] Such a delayed recombination of photogenerated charges in large single crystals and bulk films of perovskites is assigned to the free diffusion of excitations.[2,3,9,11,20-25] The delayed recombination of charges in PNC films suggests carrier diffusion among PNCs.[27,29] On the other hand, a high rate (k_r = 0.7~1×10^8 s^{-1}, Figure 4.5) of radiative recombination for PNCs isolated in a solution or on a substrate and excited with low-intensity light is observed, which excludes the possibility of delayed recombination within individual PNCs. Interestingly, the rate of

radiative recombination in PNC films increases with increase in the concentration of photogenerated charge carriers, which is obvious from the fast PL decays (Figure 4.9a) and enhanced photocounts [Figure 4.9(b-e)]. In a $FAPbBr_3$ PNC film, the τ_{av} value is decreased from 1.86 μs to 28 ns, which is from 915 ns to 24 ns for a $MAPbBr_3$ PNC film, upon increasing the excitation laser intensity from 0.0024 to 24.00 mJ cm^{-2}.[27]

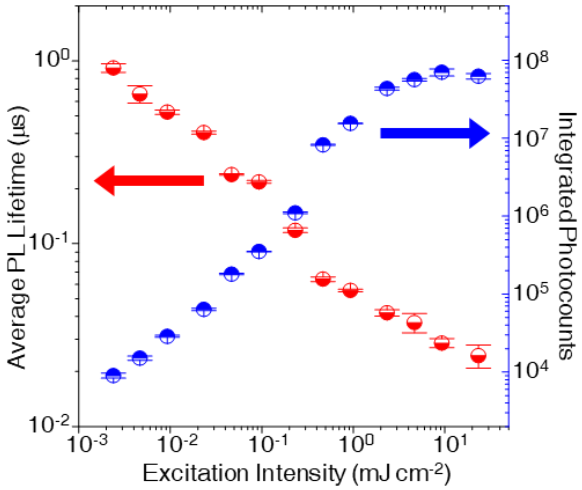

Figure 4.10 Plots of τ_{av} values and the total number of photons emitted by a $MAPbBr_3$ PNC film as the function of excitation intensity.

Such an excitation laser intensity dependent PL and charge carrier dynamics in PNC films suggest a strong correlation among excitation intensity, the density and diffusion of charge carriers, and the rate of radiative recombination, which is shown in Figures 4.10, taking $MAPbBr_3$ PNC film as an example. Here, the number of emitted photons is increased, and the τ_{av} value is decreased, both nonlinearly with increase in excitation intensity. These results support the spatial confinement and amplified radiative recombination of photogenerated charge carriers. However, the amplified emission was not accompanied by any spectral narrowing, showing ensemble averaging. Increase in the PL intensity accompanied by the evolution of PL band narrowing under high-intensity excitation is the signature of amplified spontaneous emission (ASE) or lasing which will be discussed in detail in Chapter 5.

In addition, as discussed before in the case of colloidal PNCs, different A-site cations (Cs^+, MA^+ or FA^+) may influence the PL and charge carrier properties of closely-packed PNC assemblies as well. To investigate the relations of carrier lifetime to A-site cations, I examined the time-correlated PL properties of all inorganic $CsPbBr_3$

PNC film and compared those with $MAPbBr_3$ and $FAPbBr_3$ PNC films. Although the τ_{av} value was decreased and the PL intensity was increased with increase in the intensity of excitation light for a $CsPbBr_3$ PNC film, the longest τ_{av} (50 ns) estimated was two orders of magnitude lower than that for the organic-inorganic perovskites. Figure 4.11

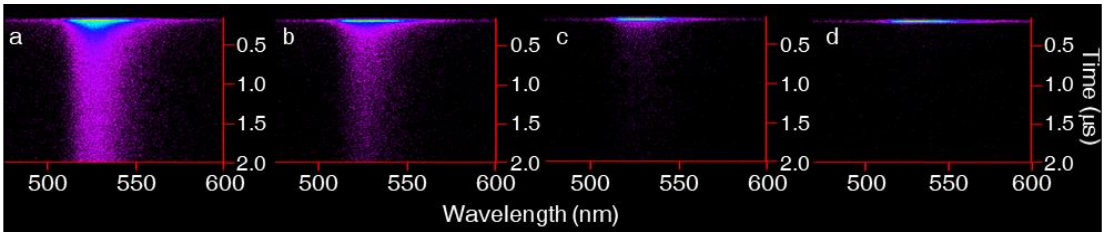

Figure 4.11 Temporally- and spectrally-resolved photocount maps of a $CsPbBr_3$ PNC film under increasing intensity of excitation laser: (a) 0.0061, (b) 0.061, (c) 0.61, and (d) 6.10 mJ cm^{-2}.

shows the spectrally- and temporally-resolved photocount maps of a $CsPbBr_3$ PNC film at different intensity of excitation. While the roles of A-site cations such as Cs^+, MA^+ or FA^+ on modulation of the conduction band minimum of PNCs are known,[34-36] the relations of A-site cations to carrier recombination time are poorly understood. The unexpectedly short τ_{av} of a $CsPbBr_3$ PNC film compared with that of a $MAPbBr_3$ or $FAPbBr_3$ PNC film suggests that the A-site organic cation (MA^+ or FA^+) is favorable for an extended diffusion of charges in a PNC film.

The dynamics of charge carriers generated in a PNC film at low- and high-intensity excitations are shown schematically in Figure 4.12a. Exposure of PNC films to high-intensity laser results in the generation of multitude of charge carriers among different PNCs in the irradiated area. At low-intensity excitation, the density of photogenerated charge carriers is low, minimizing carrier-carrier interactions and allowing for long-range carrier diffusion in the film. Because of such a long-range diffusion, PNC films excited with low-intensity laser show unexpectedly long τ_{av} values. On the other hand, by increasing the intensity of excitation laser, the diffusion of photogenerated charge carriers is spatially confined, which is due to an upsurge in the carrier concentration. Consequently, the rate of radiative recombination within the irradiated area dominates over diffusion, providing amplified emission. However, as discussed in Chapter 3 and reported elsewhere,[48-52] the PL dynamics in bulk perovskite films and single crystals involve photon recycling process, which cannot be ruled out

in the case of PNC films and clusters as well. In addition to the carrier diffusion, the long-range energy transport through photon recycling may contribute to the delayed emission and long τ_{av} values in such perovskite samples.

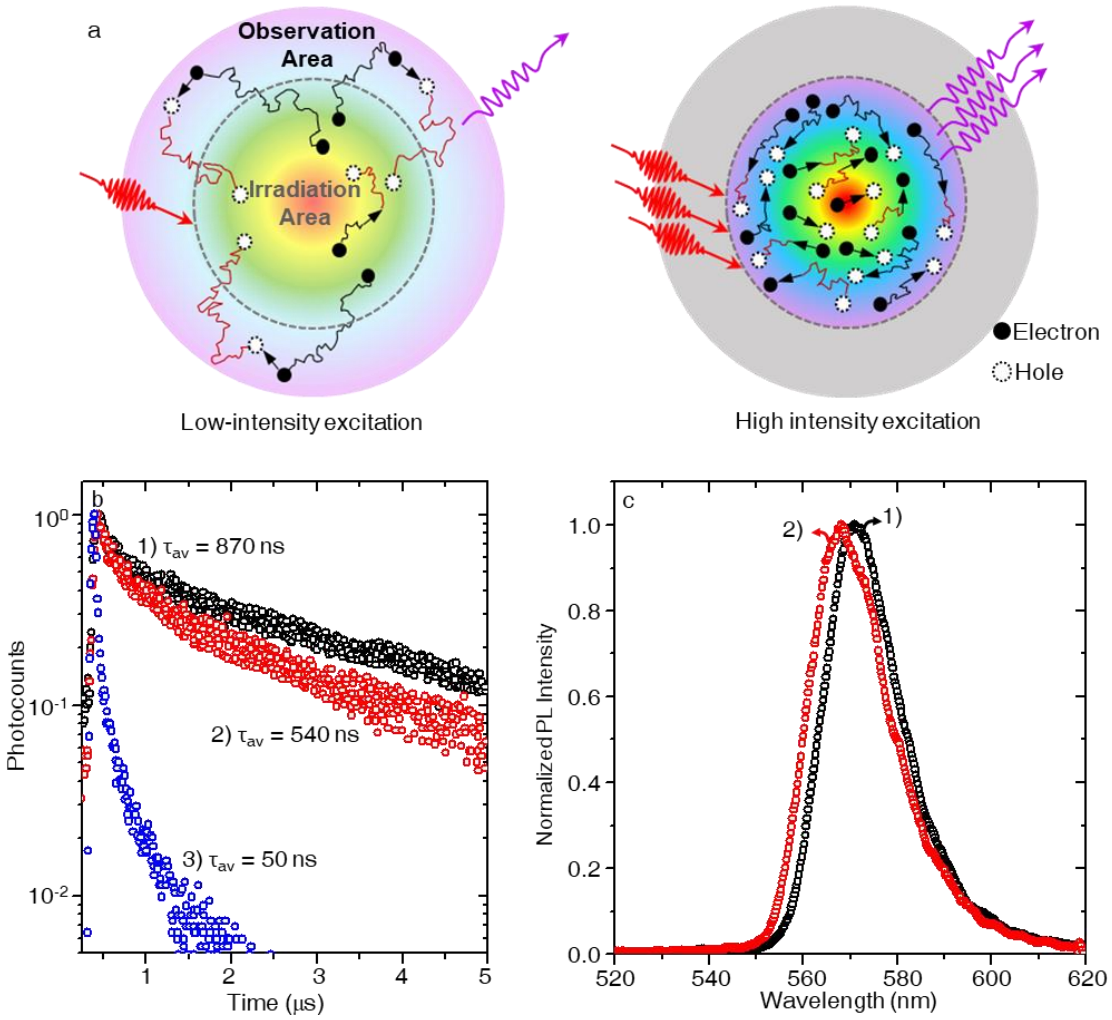

Figure 4.12 Diffusion of charge carriers in a PNC film. (a) Scheme of charge carrier diffusion and recombination. (b) PL decay profiles of a $FAPbBr_3$ PNC film recorded by selectively collecting photons from (1) non-irradiated area and (2) irradiated area, both at low-intensity excitation (0.012 mJ cm^{-2}), and (3) irradiated area at high-intensity excitation (24.00 mJ cm^{-2}). (c) PL spectra of a $FAPbBr_3$ PNC film from (1) non-irradiated and (2) irradiated areas, both at low-intensity excitation.

To verify the mechanism of excitation intensity-controlled generation and the confinement of charge carriers in a PNC film, I carried out PL masking and unmasking experiments. Here, time-resolved PL measurements on a $FAPbBr_3$ PNC film were carried out by selectively collecting the emitted photons at low and high excitation

intensities from irradiated or non-irradiated area (Figure 4.12). At low-intensity excitation, the τ_{av} (Figure 4.12b, 540 ns) of PNCs in the irradiated area was smaller than the non-irradiated area (Figure 4.12b, 870 ns). Furthermore, as shown in Figure 4.12c, the emission spectrum collected from the non-irradiated area is red-shifted compared to the irradiated area. The larger τ_{av} value and the red-shifted spectrum outside the irradiated area support the diffusion of photogenerated charge carriers from the irradiated to the non-irradiated area. The delayed and red-shifted PL suggest the presence of interparticle states that promote long-range carrier diffusion. Nevertheless, the extent of charge carrier migration depends largely on the packing density of PNCs in the film. To examine the fate of high-density charge carriers generated at high-

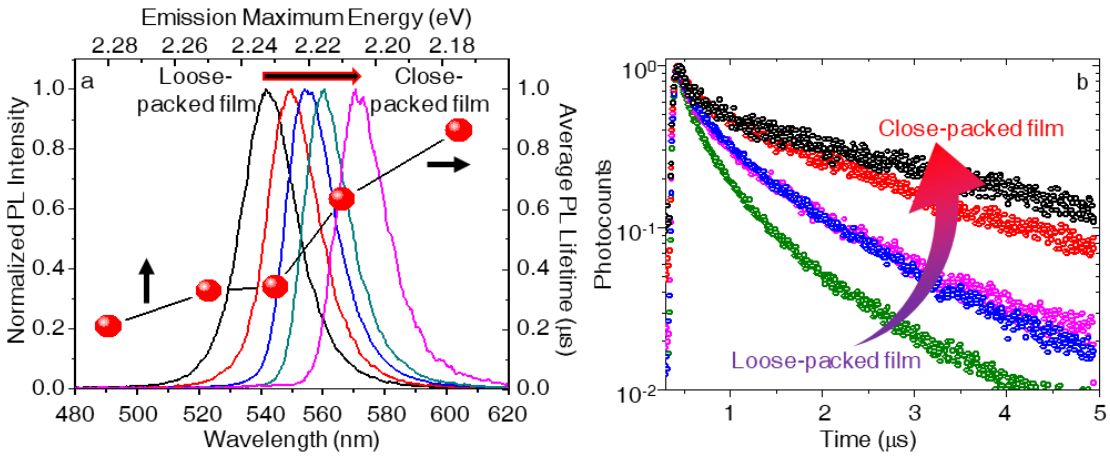

Figure 4.13 Energy loss and delayed charge carrier recombination in PNC films. (a) PL spectra and (b) PL decay profiles of $FAPbBr_3$ PNC films with different PNC density. The corresponding τ_{av} values are shown in the line-symbol plot in (a).

intensity excitation, photons were collected from the irradiated or the non-irradiated area. The τ_{av} value in the irradiated area, at high-intensity excitation, was estimated at 50 ns (Figure 4.12b), which is much smaller than at low-intensity excitation. Importantly, unlike at low-intensity excitation, I couldn't distinguish the dynamics of photogenerated charge carrier in the non-irradiated area from the irradiated area at high-intensity excitation. The small τ_{av}, which is associated with an enormous increase in PL intensity in the irradiated area support spatial confinement of charge carriers. In other words, a high density of photogenerated charge carriers in the irradiated area radiatively recombine, but without any long-range diffusion, providing amplified emission. This also indicates that the contribution of photon recycling on the carrier dynamics in PNC

films is less, although this process in the samples cannot be completely ruled out.

The degree of charge carrier migration across PNCs is further examined by recording PL spectra of closely- and loosely-packed films. As seen in Figure 4.13a, the PL spectrum of a loosely-packed $FAPbBr_3$ PNC film is shifted to the high energy side, whereas that of a closely-packed film is shifted to the low energy side. The closely- and loosely-packed PNC films were prepared by varying the density of PNCs in the solution deposited on the glass substrate, which is discussed in Chapter 2. The corresponding PL decay profiles are shown in Figure 4.13b. Interestingly, a red-shifted PL spectrum is associated with the longer τ_{av} value. The inverse relation between the energies of emitted photons and PL lifetime should be considered in terms of diffusion of charge carriers through closely-spaced states in PNC films.

4.2.5 Charge Carrier Dynamics at the Interfacial Layers of Perovskite Nanocrystals

For obtaining further insight into the relations of carrier diffusion to chemical composition, I examined the interfacial migration of charge carriers in multilayer perovskites with different halogen compositions. I deposited $MAPbBr_3$ PNCs on a $MAPbCl_3$ microcrystal film and studied the time-resolved PL characteristics of the interface in real-time. Immediately after deposition, I observed distinct blue (ca. 440 nm) and green (ca. 520 nm) emissions, respectively from the $MAPbCl_3$ and $MAPbBr_3$ layers (Figure 4.14a,d). Within a few minutes after the deposition, a new, distinct emission band ca. 465 nm (Figure 4.14b,e) emerged. The PL intensities of individual perovskites at the interface decreased with time, which was accompanied by an enormous increase in the intensity of the new band (Figure 4.14c,f). Like in several reports about halogen exchange reactions,[4,6,16,28,31,33] the new emission is attributed to interfacial exchange of chloride and bromide, and the formation of mixed chloride-bromide perovskites. The τ_{av} values of $MAPbCl_3$ and $MAPbBr_3$, recorded immediately after deposition of the layers, are 3.0 and 3.5 ns, respectively. The lifetime of the mixed halide perovskite formed at the interface is estimated at 6 ns. These lifetime values are much smaller than a $MAPbBr_3$ PNC film (915 ns), indicating poor migration of charge carriers at the interface. However, the fast, temporal evolution of mixed halide perovskite interface limited the further extraction of information about charge carrier dynamics at the interface. Kamat and coworkers[53] have demonstrated layer-by-layer

deposition of $CsPbX_3$ (X = Cl, Br, I) through electrophoresis, wherein a white light emitting multilayer perovskite structure is accomplished by employing $PbSO_4$-Oleate

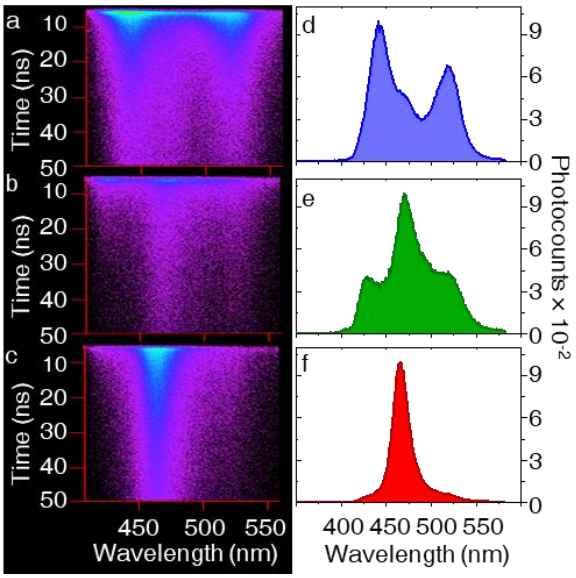

Figure 4.14 Temporally- and spectrally-resolved PL from the interface between $MAPbBr_3$ and $MAPbCl_3$ films. (a-c) Streak camera images and (d-f) the corresponding PL spectra.

ligand that suppresses halogen exchange. By adapting such methods, I expect to prevent halogen exchange and resolve charge carrier migration at interfaces between PNC films.

4.3 Conclusions

While lead halide perovskites are exciting materials for photovoltaic and optoelectronic devices, the potential applications of self-assembled and close-packed PNCs in LEDs and solar cells are yet to be explored. In this chapter, I demonstrated excitation-intensity dependent charge carrier dynamics in lead halide PNCs which are closely-packed and self-assembled into clusters and films. I studied organic-inorganic $MAPbBr_3$ and $FAPbBr_3$ PNCs and all-inorganic $CsPbBr_3$ PNCs. I detected unusually long τ_{av} values in the clusters and films of organic-inorganic PNCs at low-intensity excitation, which resulted from the diffusion of charge carriers over long distances across the nanocrystal assembly. In other words, the PNC assembly stabilized the charge carriers under low-intensity excitation, resulting in delayed PL. On the other hand, at high-intensity excitation, I found amplified PL with short lifetime from the clusters and films of these PNCs. This is attributed to the increased rate of radiative recombination of spatially-

confined manifold charge carriers generated at high-intensity excitation in close-packed nanocrystals. These results suggest the potentials of harvesting freely-diffusing charge carriers in solar cells and utilization of amplified emission in LEDs. Compared to organic-inorganic perovskites, the all-inorganic $CsPbBr_3$ PNC assembly showed short τ_{av} values, suggesting the role of A-site organic cation (MA^+ or FA^+) for an extended diffusion of charges in the nanocrystal assembly. Although multicolor emission was detected at the interface of chloride-bromide perovskites, the migration of charge carriers across the interface was complicated by halogen exchange. By controlling the migration of charge carriers and halogens, novel interfacial properties and device applications of layered perovskites can be realized.

References

1. Kojima, A.; Teshima, K.; Shirai, Y.; Miyasaka, T. Organometal Halide Perovskites as Visible-Light Sensitizers for Photovoltaic Cells. *J. Am. Chem. Soc.* **2009**, *131*, 6050−6051.

2. deQuilettes, D. W.; Vorpahl, S. M.; Stranks, S. D.; Nagaoka, H.; Eperon, G. E.; Ziffer, M. E.; Snaith, H. J.; Ginger, D. S. Impact of Microstructure on Local Carrier Lifetime in Perovskite Solar Cells. *Science* **2015**, *348*, 683−686.

3. Noel, N. K.; Wenger, B.; Habisreutinger, S. N.; Patel, J. B.; Crothers, T.; Wang, Z.; Nicholas, R. J.; Johnston, M. B.; Herz, L. M.; Snaith, H. J. Highly Crystalline Methylammonium Lead Tribromide Perovskite Films for Efficient Photovoltaic Devices. *ACS Energy Lett.* **2018**, *3*, 1233−1240.

4. Zhang, F.; Zhong, H.; Chen, C.; Wu, X.; Hu, X.; Huang, H.; Han, J.; Zou, B.; Dong, Y. Brightly Luminescent and Color-Tunable Colloidal $CH_3NH_3PbX_3$ (X=Br, I, Cl) Quantum Dots: Potential Alternatives for Display Technology. *ACS Nano* **2015**, *9*, 4533−4542.

5. Xing, G.; Mathews, N.; Lim, S. S.; Yantara, N.; Liu, X.; Sabba, D.; Grätzel, M.; Mhaisalkar, S.; Sum, T. C. Low-Temperature Solution-Processed Wavelength-Tunable Perovskites for Lasing. *Nat. Mater.* **2014**, *13*, 476−480.

6. Kim, Y.-H.; Cho, H.; Heo, J. H.; Kim, T.-S.; Myoung, N.; Lee, C.-L.; Im, S. H.; Lee, T.-W. Multicolored Organic/Inorganic Hybrid Perovskite Light-Emitting Diodes. *Adv. Mater.* **2015**, *27*, 1248−1254.

7. Herz, L. M. Charge carrier Mobilities in Metal Halide Perovskites: Fundamental Mechanisms and Limits. *ACS Energy Lett.* **2017**, *2*, 1539−1548.

8. Stranks, S. D.; Burlakov, V. M.; Leijtens, T.; Ball, J. M.; Goriely, A.; Snaith, H. J. Recombination Kinetics in Organic-Inorganic Perovskites: Excitons, Free Charge, and Subgap States. *Phys. Rev. Appl.* **2014**, *2*, 034007.

9. Saba, M.; Cadelano, M.; Marongiu, D.; Chen, F.; Sarritzu, V.; Sestu, N.; Figus, C.; Aresti, M.; Piras, R.; Lehmann, A. G.; Cannas, C.; Musinu, A.; Quochi, F.; Mura, A.; Bongiovanni, G. Correlated Electron–Hole Plasma in Organometal Perovskites. *Nat. Commun.* **2014**, *5*, 5049.

10. Yang, Y.; Yang, M.; Li, Z.; Crisp, R.; Zhu, K.; Beard, M. C. Comparison of Recombination Dynamics in $CH_3NH_3PbBr_3$ and $CH_3NH_3PbI_3$ Perovskite Films: Influence of Exciton Binding Energy. *J. Phys. Chem. Lett.* **2015**, *6*, 4688−4692.

11. Phuong, L. Q.; Yamada, Y.; Nagai, M.; Maruyama, N.; Wakamiya, A.; Kanemitsu, Y. Free Carriers versus Excitons in $CH_3NH_3PbI_3$ Perovskite Thin Films at Low Temperatures: Charge Transfer from the Orthorhombic Phase to the Tetragonal Phase. *J. Phys. Chem. Lett.* **2016**, *7*, 2316−2321.

12. Liu, Q.; Wang, Y.; Sui, N.; Wang, Y.; Wang, X.; Chi, X.; Wang, Q.; Chen, Y.; Ji, W.; Zou, L.; Zhang, H. Exciton Relaxation Dynamics in Photo-Excited $CsPbI_3$ Perovskite Nanocrystals. *Sci. Rep.* **2016**, *6*, 29442.

13. Chirvony, V. S.; González-Carrero, S.; Suárez, I.; Galian, R. E.; Sessolo, M.; Bolink, H. J.; Martínez-Pastor, J. P.; Pérez-Prieto, J. Delayed Luminescence in Lead Halide Perovskite Nanocrystals. *J. Phys. Chem. C* **2017**, *121*, 13381−13390.

14. Jha, A.; Duan, H.-G.; Tiwari, T.; Nayak, P. K.; Snaith, H. J.; Thorwart, M.; Miller, R. J. D. Direct Observation of Ultrafast Exciton Dissociation in Lead Iodide Perovskite by 2D Electronic Spectroscopy. *ACS Photonics* **2018**, *5*, 852−860.

15. Butkus, J. Vashishtha, P.; Chen, K.; Gallaher, J. K.; Prasad, S. K. K.; Metin, D. Z.; Laufersky, G.; Gaston, N.; Halpert, J. E.; Hodgkiss, J. M. The Evolution of Quantum Confinement in $CsPbBr_3$ Perovskite Nanocrystals. *Chem. Mater*. **2017**, *29*, 3644−3652.

16. Levchuk, I.; Osvet, A.; Tang, X.; Brandl, M.; Perea, J. D.; Hoegl, F.; Matt, G. J.; Hock, R.; Batentschuk, M.; Brabec, C. J. Brightly Luminescent and Color-Tunable Formamidinium Lead Halide Perovskite $FAPbX_3$ (X=Cl, Br, I) Colloidal Nanocrystals. *Nano Lett.* **2017**, *17*, 2765−2770.

17. Zheng, K.; Zhu, Q.; Abdellah, M.; Messing, M. E.; Zhang, W.; Generalov, A.; Niu, Y.; Ribaud, L.; Canton, S. E.; Pullerits, T. Exciton Binding Energy and the Nature of Emissive States in Organometal Halide Perovskites. *J. Phys. Chem. Lett.* **2015**, *6*, 2969−2975.

18. Li, M.; Bhaumik, S.; Goh, T. W.; Kumar, M. S.; Yantara, N.; Grätzel, M.; Mhaisalkar, S.; Mathews, N.; Sum, T. C. Slow Cooling and Highly Efficient Extraction of Hot Carriers in Colloidal Perovskite Nanocrystals. *Nat. Commun.* **2017**, *8*, 14350.

19. Li, M.; Begum, R.; Fu, J.; Xu, Q.; Koh, T. M.; Veldhuis, S. A.; Grätzel, M.; Mathews, N.; Mhaisalkar, S.; Sum, T. C. Low Threshold and Efficient Multiple Exciton Generation in Halide Perovskite Nanocrystals. *Nat. Commun.* **2018**, *9*, 4197.

20. Stranks, S. D.; Eperon, G. E.; Grancini, G.; Menelaou, C.; Alcocer, M. J. P.; Leijtens, T.; Herz, L. M.; Petrozza, A.; Snaith, H. J. Electron-Hole Diffusion Lengths Exceeding 1Micrometer in an Organometal Trihalide Perovskite Absorber. *Science* **2013**, *342*, 341−344.

21. Shi, D.; Adinolfi, V.; Comin, R.; Yuan, M.; Alarousu, E.; Buin, A.; Chen, Y.; Hoogland, S.; Rothenberger, A.; Katsiev, K.; Losovyj, Y.; Zhang, X.; Dowben, P. A.; Mohammed, O. F.; Sargent, E. H.; Bakr, O. M. Low Trap-State Density and Long Carrier Diffusion in Organolead Trihalide Perovskite Single Crystals. *Science* **2015**, 347, 519−522.

22. Dong, Q.; Fang, Y.; Shao, Y.; Mulligan, P.; Qiu, J.; Cao, L.; Huang, J. Electron-Hole Diffusion Lengths >175 μm in Solution-Grown $CH_3NH_3PbI_3$ Single Crystals. *Science* **2015**, *347*, 967−970.

23. deQuilettes, D. W.; Koch, S.; Burke, S.; Paranji, R. K.; Shropshire, A. J.; Ziffer, M. E.; Ginger, D. S. Photoluminescence Lifetimes Exceeding 8 μs and Quantum Yields Exceeding 30% in Hybrid Perovskite Thin Films by Ligand Passivation. *ACS Energy Lett.* **2016**, *1*, 438−444.

24. Zhumekenov, A. A.; Saidaminov, M. I.; Haque, M. A.; Alarousu, E.; Sarmah, S. P.; Murali, B.; Dursun, I.; Miao, X. H.; Abdelhady, A. L.; Wu, T.; Mohammed, O. F. Formamidinium Lead Halide Perovskite Crystals with Unprecedented Long Carrier Dynamics and Diffusion Length. *ACS Energy Lett.* **2016**, *1*, 32−37.

25. Bi, Y.; Hutter, E. M.; Fang, Y.; Dong, Q.; Huang, J.; Savenije, T. J. Charge Carrier Lifetimes Exceeding 15 μs in Methylammonium Lead Iodide Single Crystals. *J. Phys. Chem. Lett.* **2016**, *7*, 923−928.

26. Ghimire, S.; Nair, V. C.; Muthu, C.; Yuyama, K.; Vacha, M.; Biju, V. Photoinduced Photoluminescence Enhancement in Self-Assembled Clusters of Formamidinium Lead Bromide Perovskite Nanocrystals. *Nanoscale* **2019**, *11*, 9335−9340.

27. Ghimire, S.; Chouhan, L.; Takano, Y.; Takahashi, K.; Nakamura, T.; Yuyama, K.; Biju, V. Amplified and Multicolor Emission from Films and Interfacial Layers of Lead Halide Perovskite Nanocrystals. *ACS Energy Lett.* **2019**, *4*, 133−141.

28. Hoffman, J. B.; Schleper, A. L.; Kamat, P. V. Transformation of Sintered $CsPbBr_3$ Nanocrystals to Cubic $CsPbI_3$ and Gradient $CsPbBr_xI_{3-x}$ through Halide Exchange. *J. Am. Chem. Soc.* **2016**, *138*, 8603−8611.

29. Nair, V. C.; Muthu, C.; Rogach, A. L.; Kohara, R.; Biju, V. Channeling Exciton Migration into Electron Transfer in Formamidinium Lead Bromide Perovskite Nanocrystal/Fullerene composites. *Angew. Chem. Int. Ed.* **2017**, *56*, 1214−1218.

30. Sánchez-Iglesias, A.; Grzelczak, M.; Altantzis, T.; Goris, B.; Perez-Juste, J.; Bals, S.; Van Tendeloo, G.; Donaldson Jr, S. H.; Chmelka, B. F.; Israelachvili, J. N.;

Liz-Marzán, L. M. Hydrophobic Interactions Modulate Self-Assembly of Nanoparticles. *ACS nano* **2012**, *6*, 11059−11065.

31. Protesescu, L.; Yakunin, S.; Bodnarchuk, M. I.; Krieg, F.; Caputo, R.; Hendon, C. H.; Yang, R. X.; Walsh, A.; Kovalenko, M. V. Nanocrystals of Cesium Lead Halide Perovskites ($CsPbX_3$, X = Cl, Br, and I): Novel Optoelectronic Materials Showing Bright Emission with Wide Color Gamut. *Nano Lett.* **2015**, *15*, 3692−3696.

32. Hanusch, F. C.; Wiesenmayer, E.; Mankel, E.; Binek, A.; Angloher, P.; Fraunhofer, C.; Giesbrecht, N.; Feckl, J. M.; Jaegermann, W.; Johrendt, D.; Bein, T.; Docampo, P. Efficient Planar Heterojunction Perovskite Solar Cells Based on Formamidinium Lead Bromide. *J. Phys. Chem. Lett.* **2014**, *5*, 2791−2795.

33. Song, J.; Li, J.; Li, X.; Xu, L.; Dong, Y.; Zeng, H. Quantum Dot Light-Emitting Diodes Based on Inorganic Perovskite Cesium Lead Halides ($CsPbX_3$). *Adv. Mater.* **2015**, *27*, 7162−7167.

34. Amat, A.; Mosconi, E.; Ronca, E.; Quarti, C.; Umari, P.; Nazeeruddin, Md. K.; Grätzel, M.; Angelis, F. D. Cation-Induced Band-gap Tuning in Organohalide Perovskites: Interplay of Spin–Orbit Coupling and Octahedra Tilting. *Nano Lett.* **2014**, *14*, 3608−3616.

35. Stoumpos, C. C.; Kanatzidis, M. G. The Renaissance of Halide Perovskites and their Evolution as Emerging Semiconductors. *Acc. Chem. Res.* **2015**, *48*, 2791−2802.

36. Manser, J. S.; Christians, J. A.; Kamat, P. V. Intriguing Optoelectronic Properties of Metal Halide Perovskites. *Chem. Rev.* **2016**, *116*, 12956−13008.

37. Yarita, N.; Tahara, H.; Ihara, T.; Kawawaki, T.; Sato, R.; Saruyama, M.; Teranishi, T.; Kanemitsu, Y. Dynamics of Charged Excitons and Biexcitons in $CsPbBr_3$ Perovskite Nanocrystals Revealed by Femtosecond Transient-Absorption and Single-Dot Luminescence Spectroscopy. *J. Phys. Chem. Lett.* **2017**, *8* 1413−1418.

38. Li, B.; Huang, H.; Zhang, G.; Yang, C.; Guo, W.; Chen, R.; Qin, C.; Gao, Y.; Biju, V. P.; Rogach, A. L; Xiao, L. Excitons and Biexciton Dynamics in Single $CsPbBr_3$ Perovskite Quantum Dots. *J. Phys. Chem. Lett.* **2018**, *9*, 6934−6940.

39. Tian, Y.; Merdasa, A.; Unger, E.; Abdellah, M.; Zheng, K.; McKibbin, S.; Mikkelsen, A.; Pullerits, T.; Yartsev, A.; Sundström, V.; Scheblykin, I. G. Enhanced Organo-Metal Halide Perovskite Photoluminescence from Nanosized Defect-Free Crystallites and Emitting Sites. *J. Phys. Chem. Lett.* **2015**, *6*, 4171−4177.

40. Tian, Y.; Peter, M.; Unger, E.; Abdellah, M.; Zheng, K.; Pullerits, T.; Yartsev, A.; Sundström, V.; Scheblykin, I. G. Mechanistic Insights into Perovskite Photoluminescence Enhancement: Light Curing with Oxygen can Boost Yield Thousandfold. *Phys. Chem. Chem. Phys.* **2015**, *17*, 24978−24987.

41. Huang, H.; Bodnarchuk, M. I.; Kershaw, S. V.; Kovalenko, M. V.; Rogach, A. L. Lead Halide Perovskite Nanocrystals in the Research Spotlight: Stability and Defect Tolerance. *ACS Energy Lett.* **2017**, *2*, 2071−2083.

42. Thomas, E. M.; Ghimire, S.; Kohara, R.; Anil, A. N.; Yuyama, K.; Takano, Y.; Thomas, K. G.; Biju, V. Blinking Suppression in Highly Excited CdSe/ZnS Quantum Dots by Electron Transfer under Large Positive Gibbs (Free) Energy Change. *ACS Nano* **2018**, *12*, 9060−9069.

43. Klimov, V. I. Multicarrier Interactions in Semiconductor Nanocrystals in Relation to the Phenomena of Auger Recombination and Carrier Multiplication. *Annu. Rev. Condens. Matter Phys.* **2014**, *5*, 285−316.

44. Park, Y.-S.; Bae, W. K.; Pietryga J. M.; Klimov, V. I. Auger Recombination of Biexcitons and Negative and Positive Trions in Individual Quantum Dots. *ACS Nano* **2014**, *8*, 7288−7296.

45. Peterson, J. J.; Nesbitt, D. J. Modified Power Law Behavior in Quantum Dot Blinking: A Novel Role for Biexcitons and Auger Ionization. *Nano Lett.* **2009**, *9*, 338−345.

46. S. Yamashita, M. Hamada, S. Nakanishi, H. Saito, Y. Nosaka, S. Wakida and V. Biju, Auger Ionization Beats Photo-Oxidation of Semiconductor Quantum Dots: Extended Stability of Single-Molecule Photoluminescence. *Angew. Chem., Int. Ed.* **2015**, *54*, 3892−3896.

47. Hamada, M.; Nakanishi, S.; Itoh, T.; Ishikawa M.; Biju, V. Blinking Suppression in CdSe/ZnS Single Quantum Dots by TiO_2 Nanoparticles. *ACS Nano* **2010**, *4*, 4445−4454.

48. Yamada, Y.; Yamada, T.; Phuong, L. Q.; Maruyama, N.; Nishimura, H.; Wakamiya, A.; Murata, Y.; Kanemitsu, Y. Dynamic Optical Properties of $CH_3NH_3PbI_3$ Single Crystals as Revealed by One- and Two-Photon Excited Photoluminescence Measurements. *J. Am. Chem. Soc.* **2015**, *137*, 10456–10459.

49. Yamada, T.; Yamada, Y.; Nishimura, H.; Nakaike, Y.; Wakamiya, A.; Murata, Y.; Kanemitsu, Y. Fast Free-Carrier Diffusion in $CH_3NH_3PbBr_3$ Single Crystals Revealed by Time-Resolved One- and Two-Photon Excitation Photoluminescence Spectroscopy. *Adv. Electron. Mater.* **2016**, *2*, 1500290.

50. Yamada, T.; Aharen, T.; Kanemitsu, Y. Near-Band-Edge Optical Responses of $CH_3NH_3PbCl_3$ Single Crystals: Photon Recycling of Excitonic Luminescence. *Phys. Rev. Lett.* **2018**, *120*, 057404.

51. Dursun, I.; Zheng, Y.; Guo, T.; De Bastiani, M.; Turedi, B.; Sinatra, L.; Haque, M. A.; Sun, B.; Zhumekenov, A. A.; Saidaminov, M. I.; de Arquer, F. P. G.; Sargent, E. H.; Wu, T.; Gartstein, Y. N.; Bakr, O. M.; Mohammed, O. F.; Malko, A. V. Efficient Photon Recycling and Radiation Trapping in Cesium Lead Halide Perovskite Waveguides. *ACS Energy Lett.* **2018**, *3*, 1492–1498.

52. Gan, Z.; Wen, X.; Chen, W.; Zhou, C.; Yang, S.; Cao, G.; Ghiggino, K. P.; Zhang, H.; Jia, B. The Dominant Energy Transport Pathway in Halide Perovskites: Photon Recycling or Carrier Diffusion? *Adv. Energy Mater.* **2019**, *9*, 1900185.

53. Ravi, V. K.; Scheidt, R. A.; Dubose, J.; Kamat, P. V. Hierarchical Array of Cesium Lead Halide Perovskite Nanocrystals through Electrophoretic Deposition. *J. Am. Chem. Soc.* **2018**, *140*, 8887−8894.

Chapter 5

Photoinduced Electron Transfer and Amplified Spontaneous Emission

Abstract

Lead halide perovskites are promising light absorbing materials for solar cells and low-threshold optical gain media for lasing. In this chapter, I discuss the consequences of photoluminescence and charge carrier dynamics in perovskite nanocrystal films and microcrystals concerning the extraction of photogenerated charge carriers and the amplified spontaneous emission. I show that the freely diffusing charge carriers generated in perovskite nanocrystal films at low-intensity photoexcitation are efficiently extracted using fullerene as electron acceptors. I study the electron transfer process from a perovskite nanocrystal film to fullerenes by using time-resolved photoluminescence and transient absorption studies. I also discuss amplified spontaneous emission in perovskite nanocrystal films and isolated microcrystals. The ensemble averaging of photoluminescence in perovskite nanocrystal films does not offer any spectral narrowing at high-intensity excitation which suggests the importance of well-defined perovskite cavity for optical gain. Thus, I prepare the microcrystals of lead halide perovskites and analyze the temporal and spectral narrowing of photoluminescence in these samples, which is by varying the incident photon flux. The potential applications of perovskite nanocrystal films and microcrystals to solar cells and lasing is demonstrated by the harvesting of photogenerated charge carriers and the observation of amplified spontaneous emission.

5.1 Introduction

Charge carrier dynamics in closely-packed lead halide perovskites concerning photon recycling, energy transfer and carrier migration, which are discussed in chapters 3 and 4,[1-3] highlight the implications of lead halide perovskites to potential applications, such as in light-harvesting and light-emitting devices. While the applications of nanocrystals, bulk crystals and films of perovskites are already demonstrated elsewhere,[4-14] the role of carrier multiplication under high-intensity excitation in nanocrystals and microcrystals on energy-harvesting and light amplification are interesting to explore. In this chapter, I discuss the extraction or harvesting of photogenerated charge carriers from PNC films and ASE from the microcrystals of lead halide perovskites.

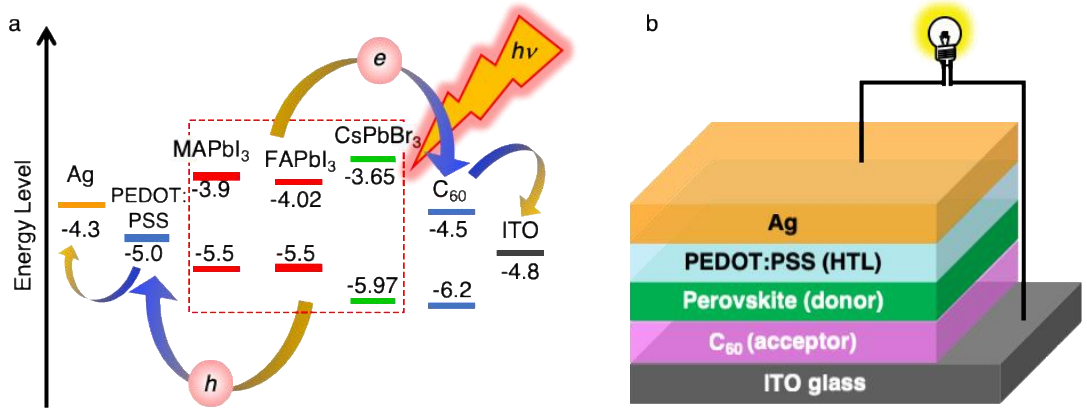

Figure 5.1 Charge carrier harvesting from perovskite layer using C_{60}.

High mobility and ambipolar and long-range diffusion of photogenerated charge carriers in a perovskite light absorbing layer is essential for the efficient collection of charges in solar cell.[11-14] The low exciton binding energy and the dominance of free charges in perovskite films and large single crystals[15-20] assist in efficient harvesting of charge carriers. Apart from the bulk films and large crystals of perovskites, PNC films are also employed for harvesting energy in solar cells.[21,22] The high PLQY and the generation of multiple charges under high-intensity excitation in PNCs are advantageous for constructing high-efficiency solar cells. Perovskites act as electron donors in solar cells. Although perovskite-based different heterojunctions are employed in solar cells, perovskite with C_{60} or its derivative is the most studied electron donor-acceptor systems for energy harvesting.[14,23-27] As shown in Figure 5.1a, C_{60} and its derivatives with their lowest unoccupied molecular orbital (LUMO) level laying lower

or comparable to those of lead halide perovskites are efficient electron acceptors in perovskite solar cells. A scheme of planar heterojunction solar cell using perovskite-C_{60} as donor-acceptor system is shown in Figure 5.1b. Importantly, the broad-band absorption of C_{60} in Vis to NIR region, photostability, and ability to accommodate multiple charges are highly desirable for efficient harvesting of electrons from perovskite layers. Under photoexcitation, the perovskite layer absorbs light to generate electron-hole pairs. The separation of charges takes place at the perovskite-C_{60} interface, which are then transported to the external circuit resulting in the photovoltaic current. Nair *et al.*[28] have discussed the efficient transfer of excitons or charge carriers from

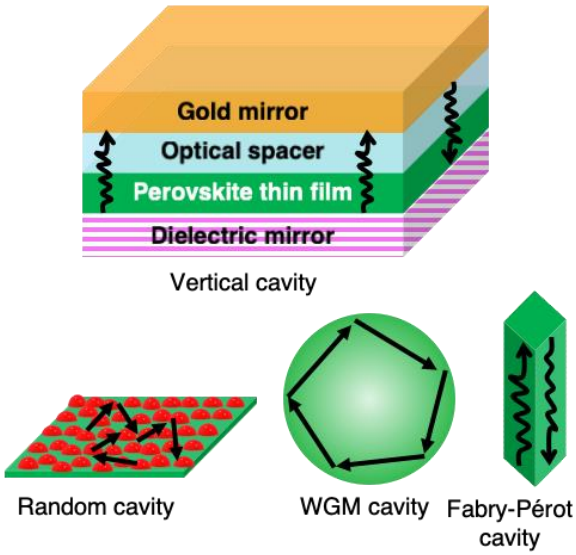

Figure 5.2 Different types of optical cavities formed by lead halide perovskites.

PNCs in a colloidal solution and films to C_{60} under photoactivation. Similarly, Privitera *et al.*[29] have reported photoinduced electron transfer from $MAPbBr_3$ PNCs to a C_{60} derivative (PCBM), resulting in efficient PL quenching in the mixed solution and the formation of PCBM anions. They demonstrated that the extent of electron transfer depends upon the length of the ligand chain, where the shorter ligands show efficient electron transfer. On the other hand, in perovskite thin films, the diffusion of charge carriers under photoexcitation is complicated by the motion of ions or vacancies which usually affects the photostability and open circuit voltage of a perovskite device.[30,31] On the other hand, C_{60}-based electron transport layers inhibit ion migration by passivating defects, binding iodide in a C_{60}-iodide complex and/or blocking grain boundaries.[23,24,26]

While the photogenerated charge carriers are efficiently collected in electron traps

such as C_{60},[14,23-29] the radiative recombination of these charges can be utilized in ASE and lasing by constructing high quality cavity resonators using lead halide perovskites. Isolated and well-assembled perovskite micro/nano plates and spheres can act as Fabry-Pérot,[8,32] WGM,[33,34] vertical,[35,36] and random cavities,[37,38] which are shown schematically in Figure 5.2. The ASE and lasing applications of lead halide perovskites are discussed briefly in Chapter 1 and are reported elsewhere.[7-9,32-38] The light is confined inside a cavity due to the difference in the refractive indices of the air and the cavity material. The minimum size of a perovskite crystal to act as a cavity for lasing or ASE is limited by $L=m\lambda/2$, where L is the length of the cavity, λ is the wavelength of light inside the perovskite crystal, and m is an integer which is equal to the number of half wavelengths inside the optical cavity.[32] λ is related to the wavelength of light in vacuum (λ_0) by $\lambda=\lambda_0/n$, where n is the refractive index of perovskite material. Therefore, for m=1, $L= \lambda/2$, which is the minimum length between the two facets of a perovskite crystal to form a Fabry-Pérot cavity for single mode lasing.

5.2 Results and Discussion

5.2.1 Extraction of Photogenerated Electrons from the Films of Perovskite Nanocrystals

The photogenerated charge carriers in perovskite films, which are diffusing over larger area, can be extracted using C_{60} and its derivatives. Here, I study the harvesting of

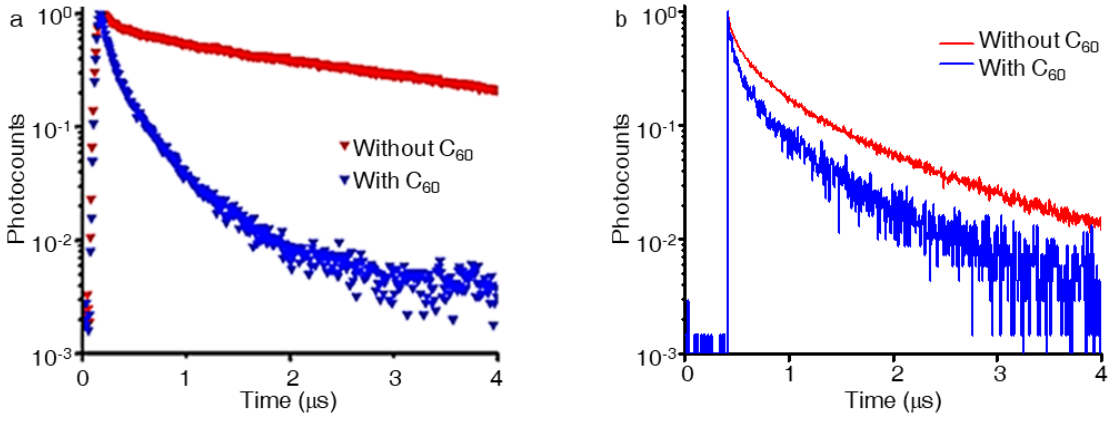

Figure 5.3 Harvesting of photogenerated charge carriers from the PNC films by C_{60}. (a,b) PL decay profiles of (a) $FAPbBr_3$ and (b) $MAPbBr_3$ PNC films with and without C_{60}. $FAPbBr_3$ PNC films were excited by using a 400 nm femtosecond laser at 0.044 mJ cm^{-2}, whereas $MAPbBr_3$ PNC films were excited by using a 365 nm pulsed LED.

photogenerated charge carriers from the PNC films by doping with C_{60}, which is by utilizing the long-range diffusion of charge carriers in such films at low-intensity excitation. PL decay profiles of $FAPbBr_3$ and $MAPbBr_3$ PNC films without and with C_{60} doping at low-intensity excitations are shown in Figure 5.3a,b, respectively. To harvest the charge carriers activated at low-intensity excitation, I doped the film samples with C_{60}. The PL lifetimes of an undoped and C_{60}-doped films are given by,

$$\tau_1=1/(k_r+k_{nr}) \quad (5.1) \text{ and}$$

$$\tau_2=1/(k_r+k_{nr}+k_{ET}) \quad (5.2),$$

respectively. Here k_r and k_{nr} are the rates of radiative and nonradiative relaxations, respectively and k_{ET} is the rate of electron transfer from PNCs to C_{60}. In the case of pristine PNC films at low-intensity excitation, I estimated the τ_1 value at 4.2 µs for $FAPbBr_3$, which was 1.06 µs for $MAPbBr_3$. These values are larger than in the samples I discussed in Chapter 4, which is attributed to the sample-to-sample variation in different preparation lots. When these PNCs were doped with C_{60}, the PL lifetime (τ_2) decreased to 0.28 µs for $FAPbBr_3$-C_{60} and 0.5 µs for $MAPbBr_3$-C_{60} films. By solving eqns. 5.1 and 5.2, I estimated the rate of electron transfer to C_{60} at 3.3×10^6 s^{-1} for a

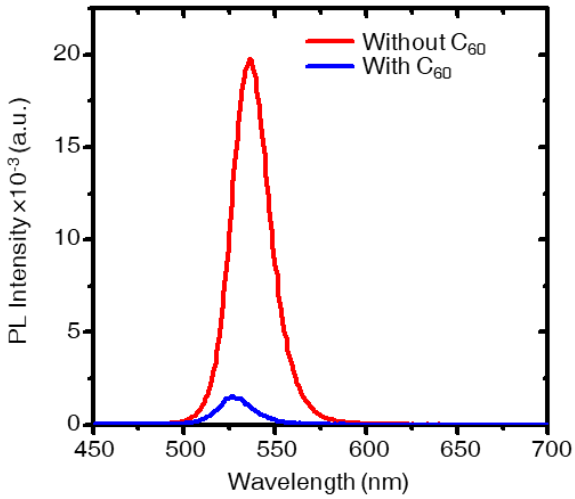

Figure 5.4 PL spectra of a pristine and C_{60}-doped $MAPbBr_3$ PNC films.

$FAPbBr_3$-C_{60} film and 1.1×10^6 s^{-1} for a $MAPbBr_3$-C_{60} film. Although the estimated rates of electron transfer from PNC films to C_{60} are not so high, an enormous quenching (>90%) of PL in a C_{60}-doped film when compared with pristine film, as shown in Figure 5.4, suggests an efficient transfer of photogenerated electron from the PNC film to C_{60}.

In other words, C_{60} acts as efficient trap for the photogenerated electrons in a PNC film under low-intensity excitation.

In order to compare the efficiency of charge carrier harvesting by C_{60} at different intensities of photoactivation, I analyzed the rate of electron transfer from a PNC film to C_{60} at high-intensity excitation. Figure 5.5 shows the PL decay profiles of pristine and C_{60}-doped $FAPbBr_3$ PNC film at high-intensity excitation. I estimated the respective τ_1 and τ_2 values of pristine $FAPbBr_3$ and $FAPbBr_3$-C_{60} films at 120 ns and 65 ns, respectively under high-intensity excitation. Again, by solving eqns. 5.1 and 5.2, I calculate the rate of electron transfer from $FAPbBr_3$ PNCs to C_{60} in the film at 7×10^6 s^{-1}. Here, the rate of electron transfer at high-intensity excitation is comparable to that at

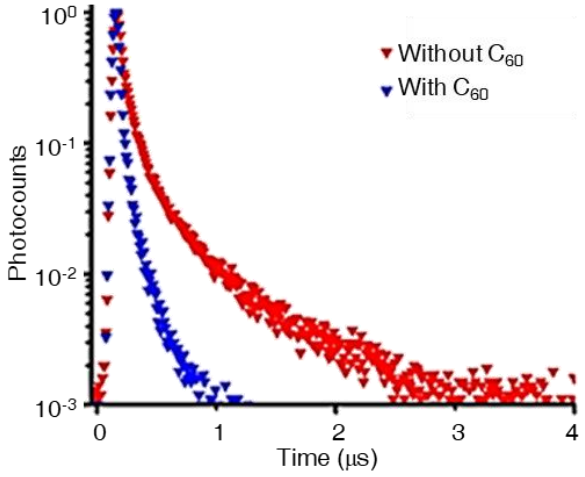

Figure 5.5 PL decay profiles of $FAPbBr_3$ PNC films with and without C_{60} at high-intensity excitation (88 mJ cm^{-2}) by using a 400 nm femtosecond laser.

low-intensity excitation despite the fact that the overall rate of relaxation under high-intensity excitation [8.3 x 10^6 s^{-1} (undoped) and 1.5 x 10^7 s^{-1} (doped)] is an order of magnitude higher than that at low-intensity [ca. 2.3 x 10^5 s^{-1} (undoped) and ca. 3.6 x 10^6 s^{-1} (doped)]. The amplification of PL under high-intensity excitations in PNC films and isolated single particles discussed in Chapter 4 suggest an increase in the rate of radiative relaxation. These results indicate that the rate of radiative relaxation, but not the rate of electron transfer, is increased at higher excitation intensities. In short, C_{60} can efficiently harvest the freely diffusing photogenerated electrons from a PNC film at low-intensity excitation.

5.2.2 Transient Absorption Studies

To obtain further insight into the electron transfer dynamics in PNCs-C_{60} film, I used the femtosecond transient absorption spectroscopy to study a $MAPbBr_3$ PNC film with and without C_{60} by exciting the samples at 400 nm. Figures 5.6a,b and c,d show the transient absorption spectra of films of pristine $MAPbBr_3$ PNCs and C_{60}-doped $MAPbBr_3$ PNCs, respectively at different pump-probe delays. The charge-separated

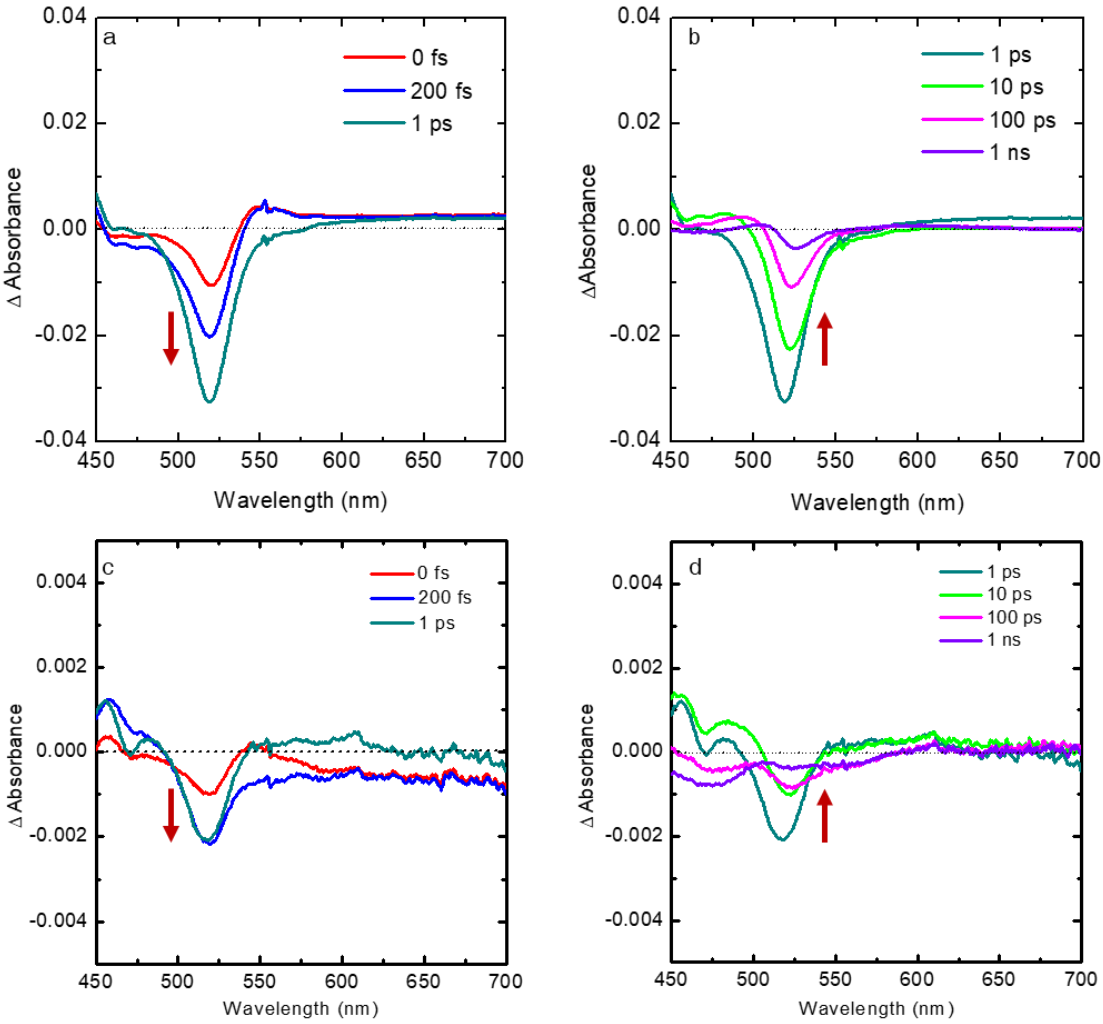

Figure 5.6 Transient absorption spectra of a $MAPbBr_3$ PNC film (a,b) without and (c,d) with C_{60}, showing (a,c) ground-state bleaching and (b,d) recovery at different pump-probe delay time. Samples are excited at 400 nm by using a femtosecond laser.

state involving C_{60} as the electron acceptor is marked with the appearance of a positive signal ca. 1070 nm, indicating the formation of a C_{60} radical anion.[39] However, I could not detect any C_{60} radical anion signal in this wavelength region of the transient absorption spectrum of C_{60} doped $MAPbBr_3$ film. I also compared the ground-state

bleaching and bleach-recovery kinetics in the transient absorption spectra of PNC film samples with and without C_{60}. A negative signal is observed at ca. 530 nm immediately after the excitation at 400 nm, indicating the ground-state bleaching. In both the cases, complete bleaching of ground state is observed within 1 ps pump-probe delay (Figure 5.6a,c). After 1 ps, ground-state bleach recovery is observed (Figure 5.6b,d), but without any significant difference between the bleach or bleach-recovery kinetics for a PNC film with and without C_{60}. However, the significant decrease in PL lifetime and the quenching of PL intensity in the case of C_{60}-doped PNC film indicates electron transfer to C_{60}. In the study, a maximum pump-probe delay of 5 ns was employed, whereas the transient absorption results indicate that the electron transfer from PNCs in the film to C_{60} is occurring outside the time window of the measurement. The efficient harvesting of photogenerated charge carriers using perovskites as the donor of electrons and C_{60} as the acceptor of electron can be promising for the development of perovskite-based high efficiency solar cells.

5.2.3 Amplified Spontaneous Emission in Perovskite Microcrystals

Beside the harvesting of freely diffusing charge carriers from the closely-packed PNC assembly at low-intensity excitation, it is interesting to utilize the carrier confinement at high-intensity excitation for the amplification of PL. As discussed in Chapter 4, with the increase in the intensity of excitation, an increase in the rate of radiative recombination was observed in the case of PNC films. However, such amplification of PL in PNC films was not accompanied by the narrowing of PL bands. In other words, I could not observe any signature of ASE or lasing in PNC films at high-intensity excitation. Although random cavity lasing is observed in the films of perovskites,[7,37,38] my results indicate that the ensemble averaging of PL from closely-packed PNCs in the film did not allow for the observation of any lasing or ASE feature. For ASE or lasing, either the PNCs must be arranged to form a well-defined cavity, such as those discussed by Yakunin *et al.*,[9] or the individual nanocrystals should act as a cavity.[8,32-34] Liu *et al.*[32] have discussed Fabry-Pérot cavity lasing in $CsPbBr_3$ nanocuboids with 400 nm edge. Similarly, Wang *et al.*[34] have demonstrated WGM lasing in $MAPbBr_3$ microplates. In my study, I observed ASE from the isolated $MAPbBr_3$ microrods of average length 15 μm and microplates with average edge-length of 10 μm, which are shown in Figure 5.7. These microcrystals show normal PL at low-intensity excitations

(Figure 5.7a,c). However, when certain threshold excitation intensity is reached or crossed, ASE occurs from the microcrystals. As observed in Figure 5.7b,d, the photoexcitation of these samples beyond the ASE threshold results in the escape of high-intensity evanescent waves from the two facets of the microrods and corners of the microplates, which is obvious from the saturation of the camera images (indicated by the dotted red circles in the figure).

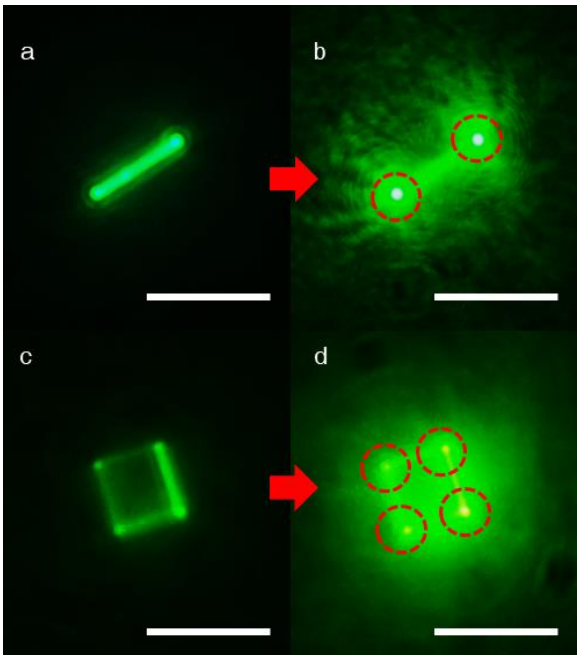

Figure 5.7 ASE from $MAPbBr_3$ perovskite microcrystals. (a,b) A $MAPbBr_3$ microrod (a) below and (b) above ASE threshold. (c,d) A $MAPbBr_3$ microplate (c) below and (d) above ASE threshold. Samples were excited at 400 nm and the scale bars correspond to 20 μm.

I analyzed ASE from the $MAPbBr_3$ perovskite microcrystals by recording the time-resolved PL from one of the microrods under increasing pump fluence. As shown in Figure 5.8a, the broad PL band (FWHM=24 nm) at low pump fluence (24 μJ cm^{-2}) gradually red-shifts and collapses into sharp PL band (FWHM = 10 nm) beyond certain excitation threshold, which is a clear signature of ASE in these microcrystals. From Figure 5.8b, I estimate the ASE threshold at 68 μJ cm^{-2}. The evolution of sharp ASE peaks in the PL spectra of an isolated $MAPbBr_3$ microcrystal is also obvious from the temporally- and spectrally-resolved photocount maps of the nanocrystal below and above the ASE threshold, as shown in Figure 5.8c. The ASE or lasing from perovskite microcrystals and nanocrystals are largely dependent upon the quality of the crystals,

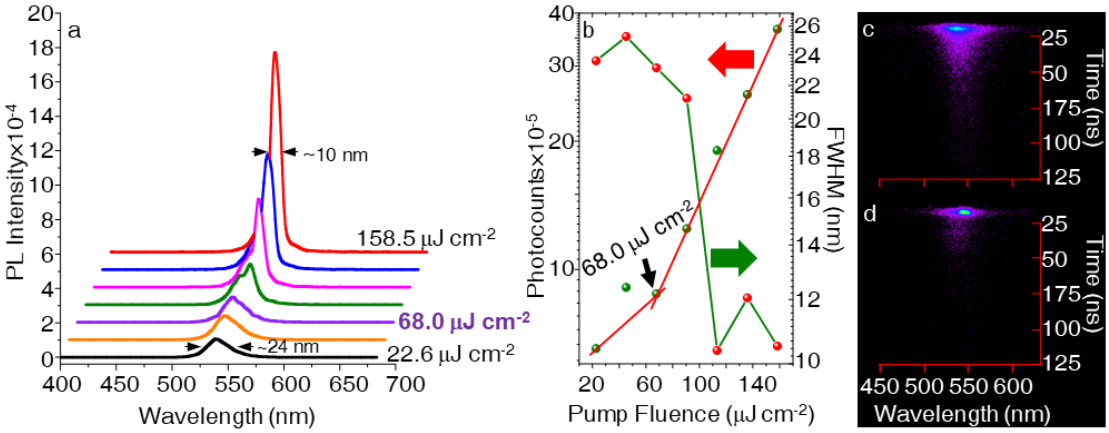

Figure 5.8 Excitation laser intensity-dependent, time-resolved PL properties of a perovskite microrod. (a) PL spectra of a $MAPbBr_3$ microrod under increasing pump fluence (22.6 to 158.5 μJ cm^{-2}), showing an increase in PL intensity along with spectral narrowing. (b) A plot of photocounts and FWHM as the function of pump fluence. ASE threshold is estimated at 68 μJ cm^{-2}. (c,d) Temporally- and spectrally-resolved photocount maps of a $MAPbBr_3$ microrod (c) below (22.6 μJ cm^{-2}) and (d) above (158.5 μJ cm^{-2}) ASE threshold (68 μJ cm^{-2}). Samples were excited with 400 nm femtosecond laser pulses.

which are often challenged by the crystallinity, phase purity, defect density, and thermal and environmental stability. In fact, such tiny crystals require higher optical gain to overcome the cavity losses. Therefore, high-quality perovskite crystals with excellent PLQY, higher optical gain and photostability are desirable for observing low-threshold ASE and lasing from them.[7-9,32-38]

5.3 Conclusions

Lead halide perovskites are emerging into a class of cutting-edge materials for high-efficiency solar cells and lighting devices. In this chapter, I studied the implications of long-range carrier diffusion in nanocrystal films and the rate of carrier recombination in the isolated microcrystals of lead halide perovskites. While the freely diffusing charge carriers generated in PNC films at low-intensity photoexcitation are efficiently harvested using C_{60} as electron acceptors, the rate of radiative recombination among these charge carriers increases under high-intensity excitation. However, the rate of electron transfer from PNCs to C_{60} remains apparently unchanged, indicating even the low-intensity photoactivation of PNCs in the film is sufficient to collect the

photogenerated charge carriers by C_{60}. Further, the increased rate of radiative recombination at high-intensity excitation in PNC films does not offer any ASE or lasing in these assemblies, suggesting the ensemble averaging of PL from random cavities of self-assembled PNCs in the film. This highlights the importance of well-defined perovskite cavity for optical gain. Such cavities are formed in high-quality perovskite microcrystals. I observe ASE from perovskite microcrystals with clear signature of temporal and spectral narrowing of PL at high-intensity excitation. The extraction of photogenerated charge carriers from PNC films using C_{60} shows, on the one hand, the confirmation of carrier migration among close-packed PNCs and, on the other hand, the potential utilization of these materials to solar energy-harvesting. ASE from perovskite microcrystals highlights their applications to lasing.

References

1. Ghimire, S.; Takahashi, K.; Takano, Y.; Nakamura, T.; Biju, V. Photon Recycling by Energy Transfer in Piezochemically Synthesized and Close-Packed Methylammonium Lead Halide Perovskites. *J. Phys. Chem. C* **2019**, *123*, 27752−27758.

2. Ghimire, S.; Nair, V. C.; Muthu, C.; Yuyama, K.; Vacha, M.; Biju, V. Photoinduced Photoluminescence Enhancement in Self-Assembled Clusters of Formamidinium Lead Bromide Perovskite Nanocrystals. *Nanoscale* **2019**, *11*, 9335−9340.

3. Ghimire, S.; Chouhan, L.; Takano, Y.; Takahashi, K.; Nakamura, T.; Yuyama, K.; Biju, V. Amplified and Multicolor Emission from Films and Interfacial Layers of Lead Halide Perovskite Nanocrystals. *ACS Energy Lett.* **2019**, *4*, 133−141.

4. Zhang, F.; Zhong, H.; Chen, C.; Wu, X.; Hu, X.; Huang, H.; Han, J.; Zou, B.; Dong, Y. Brightly Luminescent and Color-Tunable Colloidal $CH_3NH_3PbX_3$ (X=Br, I, Cl) Quantum Dots: Potential Alternatives for Display Technology. *ACS Nano* **2015**, *9*, 4533−4542.

5. Kim, Y.-H.; Cho, H.; Heo, J. H.; Kim, T.-S.; Myoung, N.; Lee, C.-L.; Im, S. H.; Lee, T.-W. Multicolored Organic/Inorganic Hybrid Perovskite Light-Emitting Diodes. *Adv. Mater.* **2015**, *27*, 1248−1254.

6. Song, J.; Li, J.; Li, X.; Xu, L.; Dong, Y.; Zeng, H. Quantum Dot Light-Emitting Diodes Based on Inorganic Perovskite Cesium Lead Halides ($CsPbX_3$). *Adv. Mater.* **2015**, *27*, 7162−7167.

7. Xing, G.; Mathews, N.; Lim, S. S.; Yantara, N.; Liu, X.; Sabba, D.; Grätzel, M.; Mhaisalkar, S.; Sum, T. C. Low-Temperature Solution-Processed Wavelength-Tunable Perovskites for Lasing. *Nat. Mater.* **2014**, *13*, 476−480.

8. Zhu, H.; Fu, Y.; Meng, F.; Wu, X.; Gong, Z.; Ding, Q.; Gustafsson, M. V.; Trinh, M. T.; Jin, S.; Zhu, X-Y. Lead Halide Perovskite Nanowire Lasers with Low Lasing Thresholds and High Quality Factors. *Nat. Mater.* **2015**, *14*, 636−643.

9. Yakunin, S.; Protesescu, L.; Krieg, F.; Bodnarchuk, M. I.; Nedelcu, G.; Humer, M.; De Luca, G.; Fiebig, M.; Heiss, W.; Kovalenko, M. V. Low-Threshold Amplified Spontaneous Emission and Lasing from Colloidal Nanocrystals of Caesium Lead Halide Perovskites. *Nat. Commun.* **2015**, *6*, 8056.

10. Ramasamy, P.; Lim, D.-H.; Kim, B.; Lee, S.-H.; Lee, M.-S.; Lee, J.-S. All-Inorganic Cesium Lead Halide Perovskite Nanocrystals for Photodetector Applications. *Chem. Commun.* **2016**, *52*, 2067−2070.

11. Stranks, S. D.; Eperon, G. E.; Grancini, G.; Menelaou, C.; Alcocer, M. J. P.; Leijtens, T.; Herz, L. M.; Petrozza, A.; Snaith, H. J. Electron-Hole Diffusion Lengths Exceeding 1 Micrometer in an Organometal Trihalide Perovskite Absorber. *Science* **2013**, *342*, 341−344.

12. Dong, Q.; Fang, Y.; Shao, Y.; Mulligan, P.; Qiu, J.; Cao, L.; Huang, J. Electron-Hole Diffusion Lengths >175 μm in Solution-Grown $CH_3NH_3PbI_3$ Single Crystals. *Science* **2015**, *347*, 967−970.

13. Kojima, A.; Teshima, K.; Shirai, Y.; Miyasaka, T. Organometal Halide Perovskites as Visible-Light Sensitizers for Photovoltaic Cells. *J. Am. Chem. Soc.* **2009**, *131*, 6050−6051.

14. deQuilettes, D. W.; Vorpahl, S. M.; Stranks, S. D.; Nagaoka, H.; Eperon, G. E.; Ziffer, M. E.; Snaith, H. J.; Ginger, D. S. Impact of Microstructure on Local Carrier Lifetime in Perovskite Solar Cells. *Science* **2015**, *348*, 683−686.

15. Herz, L. M. Charge carrier Mobilities in Metal Halide Perovskites: Fundamental Mechanisms and Limits. *ACS Energy Lett.* **2017**, *2*, 1539−1548.

16. Stranks, S. D.; Burlakov, V. M.; Leijtens, T.; Ball, J. M.; Goriely, A.; Snaith, H. J. Recombination Kinetics in Organic-Inorganic Perovskites: Excitons, Free Charge, and Subgap States. *Phys. Rev. Appl.* **2014**, *2*, 034007.

17. Saba, M.; Cadelano, M.; Marongiu, D.; Chen, F.; Sarritzu, V.; Sestu, N.; Figus, C.; Aresti, M.; Piras, R.; Lehmann, A. G.; Cannas, C.; Musinu, A.; Quochi, F.; Mura, A.; Bongiovanni, G. Correlated Electron–Hole Plasma in Organometal Perovskites. *Nat. Commun.* **2014**, *5*, 5049.

18. Yang, Y.; Yang, M.; Li, Z.; Crisp, R.; Zhu, K.; Beard, M. C. Comparison of Recombination Dynamics in $CH_3NH_3PbBr_3$ and $CH_3NH_3PbI_3$ Perovskite Films: Influence of Exciton Binding Energy. *J. Phys. Chem. Lett.* **2015**, *6*, 4688−4692.

19. Liu, Q.; Wang, Y.; Sui, N.; Wang, Y.; Wang, X.; Chi, X.; Wang, Q.; Chen, Y.; Ji, W.; Zou, L.; Zhang, H. Exciton Relaxation Dynamics in Photo-Excited $CsPbI_3$ Perovskite Nanocrystals. *Sci. Rep.* **2016**, *6*, 29442.

20. Jha, A.; Duan, H.-G.; Tiwari, T.; Nayak, P. K.; Snaith, H. J.; Thorwart, M.; Miller, R. J. D. Direct Observation of Ultrafast Exciton Dissociation in Lead Iodide Perovskite by 2D Electronic Spectroscopy. *ACS Photonics* **2018**, *5*, 852−860.

21. Akkerman, Q. A.; Gandini, M.; Di Stasio, F.; Rastogi, P.; Palazon, F.; Bertoni, G.; Ball, J. M.; Prato, M.; Petrozza, A.; Manna, L. Strongly Emissive Perovskite Nanocrystal Inks for High-Voltage Solar Cells. *Nat. Energy* **2017,** *2*, 16194.

22. Yuan, J.; Ling, X.; Yang, D.; Li, F.; Zhou, S.; *et al.* Band-Aligned Polymeric Hole Transport Materials for Extremely Low Energy Loss α-$CsPbI_3$ Perovskite Nanocrystal Solar Cells. *Joule* **2018**, *2*, 2450−2463.

23. Bai, Y.; Dong, Q.; Shao, Y.; Deng, Y.; Wang, Q.; Shen, L.; Wang, D.; Wei, W.; Huang, J. Enhancing Stability and Efficiency of Perovskite Solar Cells with Crosslinkable Silane-Functionalized and Doped Fullerene. *Nat. Commun.* **2016**, *7*, 12806.

24. Hermes, I. M.; Hou, Y.; Bergmann, V. W.; Brabec, C. J.; Weber, S. A. L. The Interplay of Contact Layers: How the Electron Transport Layer Influences Interfacial Recombination and Hole Extraction in Perovskite Solar Cells. *J. Phys. Chem. Lett.* **2018**, *9*, 6249−6256.

25. Ye, Q.-Q.; Wang, Z.-K.; Li, M.; Zhang, C.-C.; Hu, K.-H.; Liao, L.-S. N-Type Doping of Fullerenes for Planar Perovskite Solar Cells. *ACS Energy Lett.* **2018**, *3*, 875−882.

26. Li, M.; Yang, Y.-G. Wang, Z.-K.; Kang, T.; Wang, Q.; Turren-Cruz, S.-H.; Gao, X.-Y.; Hsu, C.-S.; Liao, L.-S.; Abate, A. Perovskite Grains Embraced in a Soft Fullerene Network Make Highly Efficient Flexible Solar Cells with Superior Mechanical Stability. *Adv. Mater.* **2019**, *31*, 1901519.

27. Jeng, J. Y.; Chiang, Y. F.; Lee, M. H.; Peng, S. R.; Guo, T. F.; Chen, P.; Wen, T. C. $CH_3NH_3PbI_3$ Perovskite/Fullerene Planar-Heterojunction Hybrid Solar Cells. *Adv. Mater.* **2013**, *25*, 3727−3732.

28. Nair, V. C.; Muthu, C.; Rogach, A. L.; Kohara, R.; Biju, V. Channeling Exciton Migration into Electron Transfer in Formamidinium Lead Bromide Perovskite Nanocrystal/Fullerene composites. *Angew. Chem. Int. Ed.* **2017**, *56*, 1214−1218.

29. Privitera, A.; Righetto, M.; Bozio, R.; Franco, L. The Central Role of Ligands in Electron Transfer from Perovskite Nanocrystals. *MRS Adv.* **2017**, *2*, 2327−2335.

30. Yuan, Y.; Huang, J.; Ion Migration in Organometal Trihalide Perovskite and Its Impact on Photovoltaic Efficiency and Stability. *Acc. Chem. Res.* **2016**, *49*, 286−293.

31. Zhang, H.; Fu, X.; Tang, Y.; Wang, H.; Zhang, C.; Yu, W. W.; Wang, X.; Zhang, Y.; Xiao, M. Phase Segregation due to Ion Migration in All-Inorganic Mixed-Halide Perovskite Nanocrystals. *Nat. Commun.* **2019**, *10*, 1088.

32. Liu, Z.; Yang, J.; Du, J.; Hu, Z.; Shi, T.; Zhang, Z.; Liu, Y.; Tang, X.; Leng, Y.; Li, R. Robust Subwavelength Single-Mode Perovskite Nanocuboid Laser. *ACS Nano* **2018**, *12*, 5923−5931.

33. Zhang, Q.; Su, R.; Liu, X.; Xing, J.; Sum, T. C.; Xiong, Q. High-Quality Whispering-Gallery-Mode Lasing from Cesium Lead Halide Perovskite Nanoplatelets. *Adv. Funct. Mater.* **2016**, *26*, 6238–6245

34. Wang, K.; Sun, W.; Li, J.; Gu, Z.; Xiao, S.; Song, Q. Unidirectional Lasing Emissions from $CH_3NH_3PbBr_3$ Perovskite Microdisks. *ACS Photonics* **2016**, *3*, 1125−1130.

35. Wang, Y.; Li, X.; Nalla, V.; Zeng, H.; Sun, H. Solution-Processed Low Threshold Vertical Cavity Surface Emitting Lasers from All-Inorganic Perovskite Nanocrystals. *Adv. Funct. Mater.* **2017**, *27*, 1605088.

36. Huang, C.-Y.; Zou, C.; Mao, C.; Corp, K. L.; Yao, Y.-C.; Lee, Y.-J.; Schlenker, C. W.; Jen, A. K. Y.; Lin, L. Y. $CsPbBr_3$ Perovskite Quantum Dot Vertical Cavity Lasers with Low Threshold and High Stability. *ACS Photonics* **2017**, *4*, 2281−2289.

37. Shi, Z.-F.; Sun, X.-G.; Wu, D.; Xu, T.-T.; Tian, Y.-T.; Zhang, Y.-T.; Li, X.-J.; Du, G.-T. Near-Infrared Random Lasing Realized in a Perovskite $CH_3NH_3PbI_3$ Thin Film. *J. Mater. Chem. C* **2016**, *4*, 8373−8379.

38. Yuan, F.; Wu, Z.; Dong, H.; Xi, J.; Xi, K.; Divitini, G.; Jiao, B.; Hou, X.; Wang, S.; Gong, Q. High Stability and Ultralow Threshold Amplified Spontaneous Emission from Formamidinium Lead Halide Perovskite Films. *J. Phys. Chem. C* **2017**, *121*, 15318−15325.

39. Shibu, E.S.; Sonoda, A.; Tao, Z.; Feng, Q.; Furube, A.; Masuo, S.; Wang, L.; Tamai, N.; Ishikawa, M.; Biju, V. Photofabrication of Fullerene-Shelled Quantum Dots Supramolecular Nanoparticles for Solar Energy Harvesting. *ACS Nano* **2012**, *6*, 1601−1608.

Summary and Perspectives

In this work, I studied the PL and charge carrier dynamics in closely-packed perovskite (nano or micro) crystallites. The study highlights the charge carrier properties in closely-packed assemblies of lead halide perovskites as the function of band-gap distribution and excitation laser intensity modulation. The study also investigates the extraction of photogenerated electrons from the closely-packed assemblies and the ASE in the isolated microcrystals of lead halide perovskites.

For studying the PL and charge carrier dynamics of lead halide perovskites, I synthesized pellets, nanocrystals, microcrystals and films of different types of organic-inorganic and all-inorganic perovskites employing various methods. I introduced piezochemical synthesis for the preparation of $MAPbX_3$ (X=Cl, Br, I) and mixed halide $MAPbBr_{3-x}I_x$ perovskite pellets, which is by applying a hydraulic pressure to the mixture of precursor salts. In such perovskite pellets with closely-packed crystallites, nonradiative energy transfer through the distributed band-gap was detected. Further, the role of nonradiative energy transfer on photon recycling was analyzed.

To study the charge carrier migration in closely-packed PNC assemblies, I synthesized $MAPbBr_3$, $FAPbBr_3$ and $CsPbBr_3$ PNCs and prepared their films and clusters. These nanocrystals formed closely-packed self-assembly in the film and cluster which is facilitated by the interaction among hydrophobic ligands. The films and clusters of $MAPbBr_3$ and $FAPbBr_3$ showed unusually long τ_{av} values (>1 μs) at low-intensity excitation which was attributed to the long-range diffusion of low-density charge carriers. However, at higher intensity excitations, the τ_{av} was decreased, and the rate of radiative recombination was increased in the films and clusters of PNCs. This was attributed to the spatial confinement of high-density charges which were generated at higher excitations.

To confirm long-range carrier migration in PNC films and clusters at low-intensity excitation, I extracted the photogenerated electrons from the films of $FAPbBr_3$ and $MAPbBr_3$ PNCs by using C_{60} as electron acceptors or traps. Although the PNC clusters and films showed amplified PL under higher intensity excitations, I could not detect any spectral narrowing, which is attributed to the ensemble averaging of PL among large number of random cavities formed by self-assembled PNCs in the film.

Nevertheless, spectral narrowing with ASE is observed when such perovskites form well-defined cavities under high-intensity excitation. Here, I detected ASE in isolated microrods and plates of lead halide perovskites. The ASE and extraction of charge carriers from the perovskite microcrystals and nanocrystal film, respectively indicate their potential applications in high-efficiency solar cells and low-threshold lasers.

List of Papers Presented in Conferences

1 Photon-recycling by Nonradiative Energy Transfer in Piezochemically Synthesized Organic-Inorganic Hybrid Lead Halide Perovskites

Sushant Ghimire, Yuta Takano, Vasudevanpillai Biju

2019 International Symposium of Research Institute for Electronic Science (RIES) Hokkaido University & Center for Emergent Functional Matter Science (CEFMS) National Chiao Tung University, Sapporo, Japan, December 3-4, 2019

2 Piezochemical Synthesis and Close-packing of Lead Halide Perovskites for Photon-recycling by Energy Transfer

Sushant Ghimire, Vasudevanpillai Biju

The 20th RIES-Hokudai International Symposium, Sapporo, Japan, December 2-3, 2019

3 Efficient Non-radiative Energy Transfer in Close-packed Lead Halide Perovskites Synthesized by a Pressure-induced Solid-state Method

Sushant Ghimire, Vasudevanpillai Biju

Final International Symposium on Photosynergetics, Osaka, Japan, October 23-26, 2019

4 Photon Recycling via Efficient Non-Radiative Energy Transfer in Close-packed Lead Halide Perovskites Synthesized by a Pressure-induced Solid-state Method

Sushant Ghimire, Yuta Takano, Vasudevanpillai Biju

Annual Meeting on Photochemistry 2019, Nagoya, Japan, September 10-12, 2019

5 The Dynamics of Photogenerated Charge Carriers in Perovskite Nanocrystal Films

Sushant Ghimire, Lata Chouhan, Vasudevanpillai Biju

10th Asian Photochemistry Conference, Taipei, Taiwan, December 16-20, 2018

6 Extended Diffusion of Charge Carriers in Perovskite Nanocrystal Assembly

Sushant Ghimire, Lata Chouhan, Ken-ichi Yuyama, Yuta Takano, Vasudevanpillai Biju

The 98th Annual Meeting of the Chemical Society of Japan, Funabashi, Japan, March 20-23, 2018

7 Fate of Charge Carrier Dynamics in Perovskite Nanocrystal Thin Films

Sushant Ghimire, Lata Chouhan, Ken-ichi Yuyama, Yuta Takano, Vasudevanpillai Biju:

Symposium on Nanomaterials for Environmental Purification and Energy Conversion, Sapporo, Japan, February 20-21, 2018

8 The Dynamics of Photogenerated Charge Carriers in Self-Assembled Semiconductor Nanocrystal Structures

Sushant Ghimire, Vijaykumar C Nair, Ken-ichi Yuyama, Vasudevanpillai Biju

The 18th RIES-Hokudai International Symposium, Sapporo, Japan, November 30-December 1, 2017

List of Papers Published in Peer-reviewed Journals and Patents

Dissertation Related Papers

I **Photon Recycling by Energy Transfer in Piezochemically Synthesized and Close-packed Methylammonium Lead Halide Perovskites**

Sushant Ghimire, Kiyonori Takahashi, Takayoshi Nakamura, Yuta Takano, and Vasudevanpillai Biju

Journal of Physical Chemistry C **2019**, *123*, 27752–27758

II **Photoinduced Photoluminescence Enhancement in Self-assembled Clusters of Formamidinium Lead Bromide Perovskite Nanocrystals**

Sushant Ghimire, Vijayakumar C. Nair, Chinnadurai Muthu, Ken-ichi Yuyama, Martin Vacha, and Vasudevanpillai Biju

Nanoscale **2019**, *11*, 9335–9340

III **Amplified and Multicolor Emission from Films and Interfacial Layers of Lead Halide Perovskite Nanocrystals**

Sushant Ghimire, Lata Chouhan, Yuta Takano, Kiyonori Takahashi, Takayoshi Nakamura, Ken-ichi Yuyama, and Vasudevanpillai Biju

ACS Energy Letters **2019**, *4*, 133−141

Other Papers

1 **Nonradiative Energy Transfer through Distributed Bands in Piezochemically-synthesized Cesium and Formamidinium Lead Halide Perovskites**

Sankaramangalam Balachandran Bhagyalakshmi, Sushant Ghimire, Kiyonari Takahashi, Ken-ichi Yuyama, Yuta Takano, Takayoshi Nakamura, and Vasudevan Biju

Chemistry A European Journal **2019**, DOI 10.1002/chem.201904300

2 **Blinking Beats Bleaching: The Control of Superoxide Generation by Photo-Ionized Perovskite Nanocrystals** Lata Chouhan, Sushant Ghimire, and Vasudevanpillai Biju
Angewandte Chemie International Edition **2019**, *58*, 4875−4879

3 **Phase Transfer Reaction for the Preparation of Stable Polymer-Quantum Dot Conjugates**
Geethy P Gopalan, Ajith Nair Anil, Sushant Ghimire, Nidhin Joy, Ken-ichi Yuyama, Vasudevanpillai Biju, Raju Francis
Journal of Photochemistry and Photobiology A **2019**, *371*, 91−97

4 **Blinking Suppression in Highly Excited CdSe/ZnS Quantum Dots by Electron Transfer under Large Positive Gibbs (Free) Energy Change**
Elizabeth Mariam Thomas*, Sushant Ghimire*, Reiko Kohara, Ajith Nair Anil, Ken-ichi Yuyama, Yuta Takano, K George Thomas, Vasudevanpillai Biju
ACS Nano **2018**, *12*, 9060–9069

5 **Quantum Dot–Polymer Conjugates for Stable Luminescent Displays**
Sushant Ghimire, Anjaly Sivadas, Ken-ichi Yuyama, Yuta Takano, Raju Francis, Vasudevanpillai Biju
Nanoscale **2018**, *10*, 13368−13374

6 **Relations of Exciton Dynamics in Quantum Dots to Photoluminescence, Lasing, and Energy Harvesting**
Sushant Ghimire, Vasudevanpillai Biju
Journal of Photochemistry and Photobiology C: Photochemistry Reviews **2018**, *34*, 137−151

Patent

ペロブスカイトナノ結晶薄膜、ペロブスカイトナノ結晶薄膜の製造方法、発光素 子、光電変換素子、表示装置および電子機器
Vasudevanpillai Biju, Sushant Ghimire, Lata Chouhan
Application No. PCT/JP2019/040788, Japanese Patent No. 629742

*Shared first authorship